ENGINEERING AND APPLIED SCIENCE DIVISION
CALIFORNIA INSTITUTE OF TECHNOLOGY
PASADENA, CALIFORNIA 91109

VISCOUS EFFECTS IN INCEPTION AND DEVELOPMENT OF CAVITATION ON AXI-SYMMETRIC BODIES

PART I - CAVITATION INCEPTION

PART II - A SEMI-EMPIRICAL METHOD TO PREDICT CAVITATION SEPARATION ON SMOOTH BODIES

BY

VIJAY H. ARAKERI

THIS RESEARCH WAS SPONSORED BY THE NAVAL SHIP SYSTEMS COMMAND GENERAL HYDROMECHANICS RESEARCH PROGRAM, SR0230101, ADMINISTERED BY THE NAVAL SHIP RESEARCH AND DEVELOPMENT CENTER. PREPARED UNDER OFFICE OF NAVAL RESEARCH CONTRACT N00014-67-A-0094-0023.

REPORT NO. ENG. 183-1 JANUARY 1973

Engineering and Applied Science Division
California Institute of Technology
Pasadena, California 91109

VISCOUS EFFECTS IN INCEPTION AND DEVELOPMENT OF CAVITATION ON AXI-SYMMETRIC BODIES

PART I - CAVITATION INCEPTION

PART II - A SEMI-EMPIRICAL METHOD TO PREDICT CAVITATION SEPARATION ON SMOOTH BODIES

by

Vijay H. Arakeri

This research was sponsored by the Naval Ship Systems Command General Hydromechanics Research Program, SR0230101, administered by the Naval Ship Research and Development Center. Prepared under Office of Naval Research Contract N00014-67-A-0094-0023.

Report No. Eng. 183-1
January 1973

Approved by:
A. J. Acosta

ACKNOWLEDGMENTS

The author would like to thank Professor Allan J. Acosta for his valuable guidance and encouragement at all times. Helpful suggestions by Dr. C. Brennen are appreciated.

The author would like to acknowledge the assistance of Messrs. H. Hamaguchi, J. Kingan, C. Eastvedt, G. Lundgren and M. Jessey of the Hydrodynamics and Aeronautics Laboratories.

Special thanks are due to Thomas Ward for his assistance in the experimental work.

The author would like to thank Mrs. Lynne Lacy for the excellent typing and careful preparation of the manuscript.

The author would like to gratefully acknowledge the financial support provided by the Office of Naval Research and the Naval Ship Research and Development Center through Contract No. N00014-67-A-0094-0023 which has made this experimental study possible. Major portions of the tunnel operational costs were financed by a grant from the Sloan Foundation. This support is greatfully acknowledged.

This work was done as partial fulfillment of the requirements for the degree of Doctor of Philosophy at the California Institute of Technology.

ABSTRACT

The schlieren method was developed as a flow visualization technique for use in water tunnels. The process of cavitation development on two axi-symmetric bodies was studied using this approach and found to be greatly influenced by the presence of a previously unreported viscous laminar separation. On these bodies, cavitation inception was observed to take place within this separated region which occurs far downstream of the minimum pressure point. On one of these bodies, the incipient cavitation index was found to be closely correlated with the negative value of the pressure coefficient at the point of laminar separation. Approximate computations of the position of transition on a body without laminar separation indicate that the incipient cavitation index is closely correlated with the negative value of the pressure coefficient at the predicted point of transition.

Cavitation separation under fully developed conditions is found to be preceded by a viscous laminar boundary layer separation on bodies which possess the latter separation under fully wetted conditions. An empirical method is proposed to compute the position of cavitation separation on such bodies and the method applied to a sphere and a cylinder showed good agreement with experiments.

LIST OF SYMBOLS

D	-	Diameter of the model
P_t	-	Free stream tunnel static pressure
P_v	-	Vapor pressure of water at its bulk temperature
s	-	Streamwise position along the model surface from the stagnation point
T	-	Coefficient of surface tension
U	-	Free stream tunnel velocity
U_s	-	Velocity at the position of laminar boundary layer separation
γ	-	Angular position measured from the stagnation point in degrees
μ	-	Coefficient of dynamic viscosity
ν	-	Coefficient of kinematic viscosity
ρ_L	-	Density of water
θ	-	Boundary layer momentum thickness
θ_s	-	Boundary layer momentum thickness at the position of laminar separation
$(\theta_s)_{N.C.}$	-	Boundary layer momentum thickness at the position of laminar separation under non-cavitating conditions
δ^*	-	Boundary layer displacement thickness
H	-	Boundary layer shape parameter given by, δ^*/θ
c_p	-	Pressure coefficient given by, $\frac{P - P_t}{1/2\,\rho_L U^2}$

$c_{p\,min}$ - Minimum pressure coefficient

c_{p_s} - Pressure coefficient at the position of laminar boundary layer separation

$(c_{p_s})_{N.C.}$ - Pressure coefficient at the position of laminar boundary layer separation under non-cavitating conditions

$c_{p_{tr}}$ - Pressure coefficient at the position of transition in the laminar boundary layer

H_m - Maximum height of the laminar separated layer indicated by schlieren photographs

L_r - Length of the laminar separated layer indicated by schlieren photographs

Re_D - Reynolds number given by, UD/ν

Re_{θ_s} - Reynolds number given by, $U\theta_s/\nu$

$Re^*_{\theta_s}$ - Reynolds number given by, $U_s\theta_s/\nu$

$Re_{\delta^*}, R_{\delta^*}$ - Reynolds number given by, $U_s\delta^*/\nu$

$Re_{D\,crit}$ - Critical Reynolds number at which transition takes place at the position of laminar boundary layer separation

We - Weber number given by $\rho_L U_s^2 D/T$

σ - Cavitation number based on vapor pressure given by, $P_t - P_v / 1/2\ \rho_L U^2$

σ_i - Incipient cavitation index

σ_d - Desinent cavitation index

$\overline{\sigma_i}$ - Average incipient cavitation index

σ_i^* - Cavitation inception coefficient given by, $-\dfrac{(c_{p_s}) + \overline{\sigma}_i}{(1 - c_{p_s})}$

$s_{B.L.S.}$ - Streamwise position of laminar boundary layer separation

$s_{C.S.}$ - Streamwise position of cavitation separation

$(s_{B.L.S.})_{N.C.}$ Streamwise position of laminar boundary layer separation under non-cavitating conditions

$(s_{B.L.S.})_{\sigma}$ Streamwise position of laminar boundary layer separation with cavitation at the value of σ

$(s\, c_{p\,min})_{N.C.}$ Streamwise position of the minimum pressure coefficient under non-cavitating conditions

$\gamma_{B.L.S.}$ - Angular position of laminar boundary layer separation

$\gamma_{C.S.}$ - Angular position of cavitation separation

$(\gamma_{B.L.S.})_{N.C.}$ Angular position of laminar boundary layer separation under non-cavitating conditions

$(\gamma_{B.L.S.})_{\sigma}$ Angular position of laminar boundary layer separation with cavitation at the value of σ

$(\gamma\, c_{p\,min})_{N.C.}$ Angular position of the minimum pressure coefficient under non-cavitating conditions

λ - Streamwise distance between the position of boundary layer separation and cavitation separation

λ^* - Average of λ over all the meaningful cavitation numbers

σ' - Cavitation parameter representing extent of cavitation given by, $1+[\sigma/(c_{p_s})_{N.C.}]$

Φ - Correlation parameter given by,

$$\left[\frac{(s_{B.L.S.}/D)_{N.C.} - (s_{B.L.S.}/D)_{\sigma}}{(s_{B.L.S.}/D)_{N.C.} - (s\, c_{p\,min}/D)_{N.C.}}\right]$$

Ψ - Correlation parameter given by, $\lambda^{*}/(\theta_s)_{N.C.}$

TABLE OF CONTENTS

PART I - CAVITATION INCEPTION

I. INTRODUCTION

Background

As a consequence of the equation of state one of the important differences between dynamics of liquids and gases is that, liquids can withstand tensile stresses whereas gases cannot. If sufficient tensile stresses are applied, the liquid ruptures to form cavities. Theoretical predictions indicate that pure homogeneous liquids can withstand considerable amount of tensile stresses of the order of thousands of atmospheres[1]. So far carefully treated liquid samples are known to withstand only moderate tensile stresses of the order of hundreds of atmospheres[1]. The reason for this discrepancy has led to the postulation of presence of impurities in the liquid samples commonly known as "nuclei". The initiation of vapor growth on these nuclei under the action of the tensile stress to result in visible cavity is known as the inception of cavitation. It is clear that if these cavities once formed are subjected to compressive stress, they would tend to disappear. In general, cavitation is the study of appearance, development and disappearance of cavities in a body of liquid.

If the cavities contain mainly the vapor form of the cavitating liquid, the process is known as "vaporous" cavitation; on the other hand if they mainly contain dissolved gas which is one of the most common forms of impurity in a liquid, it is termed as "gaseous" cavitation. Cavitation is of common occurrence on ship propellers, hydraulic machinery such as liquid pumping devices and on hydrofoils

used as lifting devices for hydrofoil craft. In almost all cases occurrence of cavitation is an undesirable phenomenon due to limitations on the design of liquid flow devices, the potential of damage to the solid surfaces of the body, unsteady forces and noise.

Since the onset of cavitation distinguishes the limit for cavitation-free operation, it has been the subject of considerable experimental research. In this type of work it is of great importance to predict the onset or inception of cavitation on prototypes from model studies. With regards to this prediction, scaling laws which control the behavior of flows under cavitating conditions have to be found. Therefore by "scaling" it is meant to extrapolate the cavitation behavior from one set of conditions to another. To achieve the goal of finding appropriate scaling laws, considerable experimental research has been conducted on certain simple bodies. With these studies it is hoped that a clear understanding of the basic mechanism of cavitation is obtained in order to predict the behavior of flows under cavitating conditions in complex situations.

One of the important parameters in describing cavitating flow is the cavitation number σ defined as

$$\sigma = (P_0 - P_v) / \frac{1}{2} \rho U_0^2 \quad \text{where,}$$

P_0 is the reference pressure, U_0 is the reference velocity, ρ is the liquid density and P_v is the vapor pressure of the liquid at its bulk temperature. The value of σ at which inception of cavitation occurs is designated as σ_i. In water tunnel experiments P_0 and U_0 refer to the

tunnel static pressure and velocity respectively, measured some distance away from the model. In most water tunnels, experimental conditions of cavitation inception are achieved by lowering P_0 until signs of cavitation are visible in the neighborhood of the test model while the tunnel velocity is held fixed. If σ is lowered sufficiently below that of σ_i a developed cavity is formed on the model surface and if the tunnel static pressure is increased slowly, cavitation disappears and condition of existence of last traces of cavitation on the model is known as "desinent" cavitation. The corresponding σ is designated by σ_d and has been used to describe the limit of the noncavitating flow regime notably by Holl[2]. In general it has been found that $\sigma_d > \sigma_i$ and this can be viewed as a hysteresis phenomenon. But σ is not the only pertinent physical parameter in determining cavitation inception, and a complete set of parameters determining σ_i in general is yet to be found[2, 3]. An example of this is illustrated in measurements[4] of cavitation inception index on different sized cylindrical bodies with hemispherical noses. Some of the results from Ref. (4) are shown in Fig. 1. σ_i is seen to vary with both size of the body and tunnel velocity. This dependence of σ_i on the size of the body, velocity and other variables in determining inception of cavitation is commonly termed the "scale effect". Additional inception tests conducted on different types of streamlined bodies such as a 1.5 calibre ogive[5] and various hydrofoil sections[2, 6] have exhibited different effects with change of scale.

Cavitation inception studies are normally carried out in the

many different tunnels throughout the world. Each of these possesses different hydrodynamic and physical characteristics. A program to carry out a comparison of cavitation inception measurements in many of these tunnels was recently organized by the Cavitation Committee of the International Towing Tank Conference (I. T. T. C.). The purpose of the investigation was to determine the incipient cavitation index σ_i on a particular axi-symmetric half body (see Fig. 9). In this program each laboratory was advised to use its own normal routine of performing inception measurements; no suggestions were given regarding the diameters of the model, the way of measuring tunnel static pressure, water speed and so on. Other experimental details may be found in Ref. (7). Some of the results from this study are shown in Fig. 2 from which it is evident that considerable differences in the values of observed σ_i were found in different tunnels. It is also discussed in Ref. (7) that the appearance or form of the cavitation could be different in the various facilities. One of the principle design differences between various tunnel facilities is the presence or absence of a "resorber" in the tunnel circuit. The purpose of a resorber is to put into solution the free air bubbles created during the process of tunnel operation. This is achieved by subjecting the flow to high pressures before re-entering the test section. Tunnel facilities which do not contain a resorber tend to have an abundance of macroscopic air bubbles in the water approaching the test body (readily visible under stroboscopic illumination). These macroscopic bubbles when passing through the low pressure region in the neighborhood of the model explode to

vaporous cavities and subsequently collapse. Photographs of this type of cavitation have been obtained by Knapp[8]. A different type of inception is observed in tunnel facilities which do have a resorber. This type has been described by Acosta[9]. "At this stage we would like to describe the cavitation that appears on the I. T. T. C. test body in the high speed water tunnel. In practically all of the present tests no free bubbles, or very few, in the working section upstream of the test body were observed even up to speeds of 20.0 meters per second. This is in contrast to many other water tunnels in which a copious number of free air bubbles are plainly evident – for example, the Naval Ordnance Test Station* Vertical Water Tunnel. Furthermore, as the point of cavitation inception on the body is reached, no minute traces of cavitation bubbles were seen on the I. T. T. C. test body. In practically every case when cavitation inception occurred, it took place suddenly and abruptly in the form of a small band all around the nose of the body. This appearance was characteristically abrupt rather than gradual and there were no "precursors" suggesting that cavitation inception was imminent". As further discussed in Ref. (9) this form of cavitation is termed "band" inception. But, on the same I. T. T. C. test body at higher speeds another type of cavitation inception was also observed and is termed as "spot cavitation", which commenced at a pinpoint or spot and subsequently spread out in the form of a "V" rather like a wake. A photograph of "band" type inception as observed in Ref. (9) is shown in the bottom photograph of Fig. 1 of Part II.

*Now called the Naval Undersea Research and Development Center.

Some of the differences observed in the values of σ_i in the different facilities shown in Fig. 2 may be attributed to the different types of cavitation inception just discussed. Indeed, the work done at D. T. M. B.* shows that values of σ_i measured in a 36 inch tunnel with a resorber were systematically lower by about 15-20 percent than the values of σ_i measured in the same tunnel without the resorber feature. The I. T. T. C. report [7] was not able to resolve these differences as well as others on geometrically similar bodies tested in different laboratories. One may conclude from this work that the test body used or procedures adopted did not lead to a useful means of predicting cavitation inception, or to the ability of translating the results of one experimental facility to another.

Some Physical Features of Cavitation Inception: It has been mentioned before that "nuclei" or weak spots are necessary to initiate the phase change that results in the cavitation that is observed at inception. It is apparent that in considering flows about a submerged body as in the experiments mentioned before, the nuclei can come from two sources; namely, from within the free stream, and the surface of the test body itself. Nuclei of the first type are termed as "stream nuclei" and the latter as "surface nuclei". The physical nature of the free stream nuclei have been hypothesized to be of the form of free gas bubbles[10,11], gas trapped in the crevices of solid particles in the free stream[12], or solid particles themselves[13] which are present in the fluid. It has

*Now the Naval Ship Research and Development Center.

been suggested[12] that surface nuclei consist of gas trapped in microscopic crevices of the body surface. To understand the role of nuclei in cavitation inception it is helpful to consider the static stability of a stationary spherical gas bubble containing the vapor of the fluid and a small amount of permanent gas. It is found from the results of such an analysis (see for example, Strasberg[14]) that for a given radius R_0 there is an ambient pressure below which the bubble becomes unstable. This pressure is designated as the "critical" pressure P_c which depends on the initial radius R_0. When the ambient pressure is less than P_c, the bubble may grow under the condition of constant vapor pressure and gas content. In this event the bubble may be said to grow by vaporous cavitation (i.e., gaseous diffusion does not occur). It can be shown that as R_0 becomes larger than about 10^{-2} inches, the critical pressure for the bubble growth (or vaporous cavitation) approaches, but never exceeds, the vapor pressure i.e., the critical pressure is always less than the vapor pressure. Smaller bubbles with radii of the order of 2×10^{-5} inches for example, would have a critical pressure approximately one atmosphere less than the vapor pressure. A bubble of this size in water at room temperature would therefore require a tension of this magnitude for instability to occur. Thus we can see that for any given liquid pressure lower than the vapor pressure, a bubble of radius less than a certain minimum radius will not grow or cavitate vaporously. This minimum radius may be designated as the "critical radius" R_c. We would therefore expect from these examples that if a sufficient number of nuclei are present in a flowing stream with radii larger than

about 10^{-2} inches, vaporous cavitation would begin as soon as the pressure in the neighborhood of a submerged body falls to the vapor pressure. In any case, since the minimum pressure on the body is the lowest pressure available in the flow it has been customary to predict σ_i by equating it with the minimum pressure coefficient of the body, $-c_{p\,min}$. But from comparative studies on the I. T. T. C. test body it may be observed that σ_i can be considerably different from $-c_{p\,min}$ as can be seen in Fig. 2. For the cases $\sigma_i < -c_{p\,min}$ it may be concluded either that the value of $-c_{p\,min}$ was not known correctly or that the critical pressure of liquid was not vapor pressure. It can also be seen from Fig. 2 that some of the values of σ_i are, in fact, greater than $-c_{p\,min}$, indicating occurrence of cavitation at pressures higher than vapor pressure. This observation suggests that a process other than vaporous cavitation is responsible and indeed this is attributed to gaseous diffusion and is discussed by Holl[2] in his review article. This process is termed "gaseous cavitation" in contrast to vaporous cavitation. Gaseous cavitation can occur at any ambient pressure (unlike vaporous cavitation) provided that the liquid is supersaturated in respect to the partial pressure of the gas within the bubble. The dynamics of the vaporous and gaseous growth of a nucleus is of different time scales. Typical times for vaporous growth are of the order of milliseconds[8], whereas for gaseous growth they may be of the order of few seconds[15]. This would seem to preclude gaseous cavitation as being technically important because, if bubbles move with the free stream they do not remain in low-pressure regions long enough for

appreciable growth. However, if the bubbles are trapped on a fixed boundary, sufficient time may be available for diffusion. It may be imagined that both processes occur in cavitation on real bodies, as will, in fact, be seen in the experiments to be discussed subsequently.

Thus cavitation inception process can be assumed to be dependent on two main factors, namely, (a) sources of cavitation nuclei, and (b) the growth potential of the nucleus. Following are some detailed considerations of the above mentioned two factors.

Sources of Cavitation Nuclei: As mentioned earlier depending on their origin; nuclei can be classified into either surface nuclei or stream nuclei. In recent years, there have been several investigations which have shown that inception of cavitation is influenced by surface characteristics, which presumably control the characteristics of surface nuclei. Holl and his co-workers[16, 17, 18] have carried out cavitation inception studies on hemispherical nosed bodies having surfaces of smooth stainless steel, sandblasted steel, waxed stainless steel, teflon, nylon and glass. It was observed that teflon was easy to cavitate whereas, glass was hard to cavitate. Such observations prompted Holl[2] to suggest that porosity might be an important factor influencing the characteristics of surface nuclei. It is not clear from their findings whether the change in inception characteristics was due to the above mentioned reason or due to the change in the nature of the boundary layer growth on bodies having different surface characteristics. Peterson[19] recently has found that if the test body is cleaned with acetone, then

subjected to a pressure of 19,000 psi (presumably effect of this is to drive some of the air trapped in the model crevices into solution, thus changing effective size of the surface nuclei) this produced sixteen percent reduction in the observed value of σ_i compared with the values obtained without any surface treatment. Another interesting experiment concerning surface nuclei was carried out by Acosta and Hamaguchi[9]. In their experiments the nose of the test body (the same test body used in the I. T. T. C. comparative study) was dipped into a mixture of a silicon fluid and solvent. The object of this procedure was to coat the surface of the body with a fluid which had the ability to dissolve a large amount of air as silicone fluids are known to do. The inception studies showed that when the silicone coating was fresh and presumably saturated with air incipient cavitation numbers to be systematically higher than that obtained for the case of pure water. But as the coating got old and deaerated due to evolution of cavitation bubbles the values of σ_i were found to be lower than that observed for the case of pure water. It should be mentioned that the tests were preliminary in nature, but they do indicate the possibility of existence of surface nuclei in the form of air trapped in the model crevices. Still, the knowledge regarding the role of surface nuclei in the mechanism of cavitation inception is obscure.

The role of free stream nuclei in the form of free air bubbles in the process of cavitation inception has been studied by Ripken, Killen and Schiebe[20, 21]. It is expected from the stability analysis of gas bubbles considered earlier, that the size spectrum of gas bubbles

present in the stream would be of importance in determining the value of σ_i. An acoustic method of obtaining such a spectrum for recirculating facilities has been successfully used by Schiebe[21]. Major findings of Ripken and Killen summarized in Ref. (20) are that the free gas content (in the form of gas bubbles) is at least a function of: a) total gas content, which is the sum of the free gas content and the dissolved gas content, b) tunnel pressure, and c) tunnel velocity. They also mention that the water tunnel pump is probably the main source of gas bubbles and that the free gas spectrum would be a unique property of individual tunnel facilities. It is clear from earlier considerations that measurement of free gas spectrum would be of greater importance for tunnel facilities without the presence of a resorber than for facilities with the presence of a resorber.

Growth Potential of the Nucleus: The ability of the available nucleus to grow to visible size would definitely be influenced by the magnitude and duration of the low pressure experienced by the nucleus. Photographic investigations conducted by Knapp and Hollander[8] years ago have indicated that the growth history of cavitation bubbles orginating from free stream nuclei is only slightly influenced by the presence of the boundary layer on the model surface. The development of surface nuclei into visible cavitation would be expected to be greatly influenced by the presence of the boundary layer on the model surface contrary to the behavior of free stream bubble cavitation. It is this point which has received very little attention in the understanding of cavitation inception

mechanism. During Kermeen's[4] experiments on hemispherical nosed bodies, it was observed that cavitation inception took place in the form of a ring of macroscopic bubbles around the nose of the headform and photographs indicated the presence of microscopic bubbles with diameters smaller than typical boundary layer thicknesses ahead of the macroscopic ones. These observations prompted Parkin and Kermeen[22] to study the influence of the presence of the boundary layer on the mechanism of cavitation inception. Thus from their now classic experiments[22] of 1953 they concluded that the presence of a boundary layer plays a significant role in the process of cavitation inception on streamlined bodies. Their results can be summarized as follows. The macroscopic cavitation visible to the unaided eye was sustained by very small "microscopic" bubbles which grew in the boundary layer. The microscopic bubbles grew for a time at a fixed position on the body upstream from the macroscopic cavitation. These bubbles after attaining a radius of approximately one half the displacement thickness of the boundary layer were then entrained into the flow and travelled downstream to be distorted into irregular patches which sustained the macroscopic cavitation. After further reduction of tunnel static pressure the evolution of microscopic cavitation bubbles increased until a clear attached glassy cavity was formed on the model surface. When this occurred the microscopic cavitation just described was completely suppressed. It was also concluded that latter stages of the growth of microscopic bubbles was significantly influenced by gaseous diffusion. It should be mentioned that flow visualization of the boundary

layer was done by introducing a dye streak. In their final conclusions Parkin and Kermeen mentioned the definite need for further work along their lines in order to explain theoretically the experimentally observed scale effects. Almost no experimental work along the lines of Parkin and Kermeen has been carried out since, but many theoretical models have been proposed utilizing the interpretations of Parkin and Kermeen's experimental observations.

Review of Existing Theoretical Models: In general theoretical predictions of cavitation inception are based on calculations of the growth of a spherical bubble from an initial radius R_0 to a prescribed final radius. The growth of the bubble is assumed to be determined by the solution of the Rayleigh-Plesset equation[23] to be considered later. The pressure distribution around the headform is assumed to be that existing under non-cavitating conditions. The behavior of a single spherical bubble is assumed to characterize the problem.

Parkin's Theory: One of the first attempts to model the process of cavitation inception theoretically was made by Parkin[24] in 1952. In his formulation Parkin did not consider the effects of boundary layer presence on the model surface. It was supposed that cavitation is initiated from small nuclei which contain air or water vapor, or both, stabilized on small solid particles in the liquid. Based on stability arguments and experimental observations these nuclei are taken to be equivalent to a spherical bubble of radius $R_0 = 2 \times 10^{-4}$ millimeters. This bubble is assumed to travel along the model surface

at the local liquid velocity; during this travel the growth of the bubble was estimated from the Rayleigh-Plesset equation. This equation ignoring the viscous and temperature effects in the bubble growth is[25]

$$R\ddot{R} + \frac{3}{2}\dot{R}^2 = \frac{1}{\rho_L}\left\{P_G - \frac{2T}{R} + \left[C_p(t) - \sigma_L\right]\frac{1}{2}\rho_L U_\infty^2\right\}$$

where R is the instantaneous bubble radius and a dot represents the time derivitive. σ_L is the cavitation number based on vapor pressure and the pressure coefficient $C_p(t)$ describes the time varying liquid pressure P_L seen by the bubble as it travels along the model surface. Thus, the pressure distribution on the model under non-cavitating conditions is considered to be known. The value of P_G is the gas pressure inside the bubble which is assumed to follow ideal gas law giving $P_G = P_0 \ (R_0/R)^3$ where, P_0 and R_0 are initial conditions to be prescribed.

Parkin assumed the surface tension term to be equal to zero initially and to reach its full value of $2T/R$ when $R = 5R_0$. Thus, his assumption is not quite equivalent to a free stream nuclei in the form of a gas bubble of radius R_0. Inception of cavitation was assumed to take place when the bubble radius reaches a value of 1 millimeter or when the final radius reaches 500 times the initial radius. Calculations carried out by this method for the incipient cavitation number σ_i on hemispherical nosed models showed poor agreement with the observed values. Parkin attributed the lack of agreement between theory and experiment to the neglect of the effect of the boundary layer. It should be mentioned that experiments of Parkin and Kermeen[22] showing the

importance of boundary layer in the process of cavitation inception were done after Parkin formulated his theory.

Holl and Kornhauser's Theory: Holl and Kornhauser[25] employed similar ideas as Parkin's, but they did extensive studies regarding the effect of initial conditions, stream versus surface nuclei, and thermodynamic effects. Thermodynamic effects were considered in determining the cavitation inception number for a large range bulk fluid temperatures. This required the simultaneous solution of the Rayleigh-Plesset equation for the bubble growth and the energy equation for the bubble wall temperature. These computations were made as follows: for a prescribed R_0, from static stability analysis there exists a liquid pressure, P_L, for static equilibrium. The corresponding position on the model surface at which the local pressure is equal to P_L is taken to be the starting point of bubble history. If the nucleus was a free stream nucleus, it was assumed to travel at the local velocity of the liquid, V_L; in particular, if boundary layer effects are included the velocity of the bubble, V_B, was taken to be equal to V_L within the boundary layer at a distance of one bubble radius from the model surface. If the nucleus was of the surface type, V_B initially was taken to be zero. Subsequent values of V_B were determined by carrying out a trajectory analysis of the bubble within the boundary layer accounting for inertial effects, viscous drag, and buoyancy forces arising from the pressure distribution on the body. The velocity of the liquid, V_L, was again taken at a distance of one bubble radius from one model surface.

Cavitation inception was said to occur when the bubble reaches a maximum diameter of 0.01 in. These calculations carried out for a hemispherical body showed that, if one includes thermodynamic effects in the process of cavitation inception, the value of σ_i should decrease considerably with increase in fluid temperature. Experiments, on the contrary, showed an increase in σ_i with increase in fluid temperature. This lack of agreement was attributed to possible effects of convective heat transfer in the solution of energy equation neglected in their theoretical formulation. It should be mentioned that without any physical basis whatsoever they assumed turbulent transition of the boundary layer to take place at the minimum pressure point.

The Van der Walle Theory: The Van der Walle[26] theory is again basically the same as that of Parkin's except that he considers in addition the possibility of gaseous growth, vaporous growth of both free stream and surface nuclei, and a hypothesized process of a surface nuclei being generated from a crevice. He concluded that the surface nuclei generation, their detachment and subsequent behavior will be influenced by a balance of local pressure gradient forces, inertial drag forces and surface adhesion forces. In the calculation of the drag force on the attached nucleus, the local flow was considered to be laminar or turbulent and the local velocity within the boundary layer was used in a similar manner to that of Holl's theory explained earlier but, in fact, his work was first. Thus for different bodies with different pressure gradients, Van der Walle obtained various inception relations and, accordingly, scaling factors. Finally, comparison of his theoretical

calculations of σ_i on a hemispherically nosed body showed only a qualitative agreement with the experimental results. Boundary layer calculations on this body were estimated with elementary flat plate boundary layer growth relationships.

The Oshima Theory: Oshima's theory[27] is somewhat different in the sense that he attempts to formulate strict scaling relationships based on similarity ideas and for this reason the value of σ_i must be known at a reference condition from experiments. Oshima assumed that cavitation occurs at geometrical similar positions on geometrical similar bodies. Dynamically similar growth of vapor bubbles as specified by the Rayleigh-Plesset equation is assumed to occur between two geometrically similar points. Vapor bubbles are assumed to travel at a distance from the body surface which is a constant fraction of the local boundary layer height. Finally, cavitation is assumed to occur when the bubble diameter is equal to that of the local boundary layer displacement thickness, an assumption based on Parkin and Kermeen's[22] observations. This last assumption introduces a Reynold number effect. Boundary layer transition was assumed to occur at the point of instability of the laminar boundary layer. From this, the flow at the position of inception could either be laminar or turbulent. Oshima's results compared well with the experiments even though as we will see from the present work that his last assumption is based on wrong interpretations of Parkin's experiments.

Johnson and Hsieh's Theory: The previously considered theoretical models place main importance on the bubble growth which

takes place inside the boundary layer. But considerations of the growth of free stream gas bubbles into macroscopic cavitation as observed by Knapp[8] can, in fact, disregard the presence of the boundary layer unless these bubbles somehow get entrained into it. It was mentioned earlier that if there is a sufficient number of free stream nuclei in the form of gas bubbles with radii larger than say 10^{-2} in. present in the stream, the value of σ_i would be expected to be equal to $-c_{p\,min}$ from bubble stability considerations. Johnson and Hsieh[28] consider the trajectories of these free stream bubbles with the flow past a body. They find that under the effects of the pressure gradient there is a certain "screening" process of the various sized bubbles which tends to deflect the larger bubbles away from the minimum pressure area near the body. This screening process is speed and size dependent and leads to scaling relations again based on the idea of a "critical" radius, but with certain assumed free stream nuclei distributions. The consistent trend of these relations is for an increase of σ_i with increase in speed and body size. Scheibe[21] has used these above mentioned ideas to compute σ_i with more realistic free stream nuclei distribution and his computations agreed only qualitatively with experimentally measured values.

Scope of Present Work: From previous comments it is clear that, both experimental and theoretical investigations have neglected any detailed consideration of possible real fluid effects on cavitation inception. Especially noteworthy oversights are the possibility of separation and

of any consideration for the unsteady effects of transition itself. Transient pressures are known to influence the value of σ_i in separated flows behind disks[29], rearward facing steps[30], fully developed turbulent channel flow[31] and in the mixing layer of a submerged jet[32] as discussed by Arndt and Ippen in their review[33].

Through private communication J. W. Holl of the Pennsylvania State University has brought to our attention some recent work by A. B. Bailey[34] and M. V. Casey. In their work they have shown a good correlation of measured σ_i with negative value of the pressure coefficient at the predicted position of laminar separation on hydrofoils at moderate angles of attack. The position of separation was estimated by Thwaites approximate method. But, the agreement mentioned above does get worse with increase in Reynolds number and increase in angle of attack. As will be discussed later similar calculations during early portion of present investigation prompted us to take up the subsequent experimental study.

It may be mentioned here that there are several possible viscous flow regimes on a streamlined body; these include, (a) laminar boundary layer flow without separation or transition, (b) laminar boundary layer flow with transition but without any separation, (c) same as (b) but with possible turbulent separation after transition, and (d) flow with laminar boundary layer separation with the possible subsequent transition in the separated free shear layer. It is expected that inception would be dependent on the flow regime. Further, it might be misleading to draw comparisons of values of σ_i obtained in different flow regimes without

this knowledge. The present work is concerned with identifying the type of viscous flow regime on some of the bodies used in cavitation research by a new technique and further to determine how cavitation inception may be influenced by these real fluid flows.

Our interest in this approach was prompted by some preliminary boundary layer growth calculations made for the I. T. T. C. test body. It was found that the position of inception roughly coincided with the predicted position of the laminar separation. It was also found that the value of the inception cavitation number was very close to the pressure coefficient at this point. These findings stimulated us to take a new look at the interaction of viscous effects with mechanism of cavitation inception on streamlined bodies along the same lines as Parkin's[22] original work. It was believed that earlier methods of flow visualization used in water tunnel research would be inadequate and that a different method of flow visualization would be needed. The schlieren technique widely used in the field of compressible aerodynamics was subsequently (and successfully) developed for this purpose[35].

Electrolysis bubbles as a means of flow visualization is of common use in slow liquid flows. For the present studies it was thought that this principle could be utilized as a source of artificial surface nuclei. A modest investigation of the use of this technique for research in cavitation inception seems to be in order.

2. EXPERIMENTAL METHODS

2.1 Flow Visualization

Need for New Method: Normally conventional methods of flow visualization such as dye injection and oil film techniques are difficult to use in water, especially at high velocities. The author had come to realize these difficulties in his earlier work with flow visualization on hydrofoils[6] by oil film technique. During some preliminary work of the present studies, the method of dye injection was used to show the existence of a laminar separated flow on a two inch hemispherical nose at a tunnel velocity of about 5 feet per second, but at a velocity of about 15 feet per second the observations were difficult to interpret and were confusing. Due to these difficulties a better method of flow visualization had to be developed. Many methods were considered including interferometry, schlieren technique and skin friction gages. The latter were thought to be feasible but expensive to obtain spatial resolution. Interferometry and the schlieren technique both require a density gradient in the vicinity of the viscous boundary layer. It was thought the necessary gradients could be created by heating or cooling of the model and that the resulting thermal boundary layer could then be visualized by interferometry or the schlieren technique. Of the two, the latter is far simpler and has a long history of use in compressible aerodynamics. The gross properties of thermal and hydrodynamic boundary layers especially when visualizing such details as separation and transition are very similar. Finer details such as relationship between the growth

of the two boundary layers are dependent on the Prandtl number and the starting position of heating or cooling.

Preliminary Work: The feasibility of the schlieren method was determined by carrying out preliminary experiments in the Free Surface Water Tunnel (FSWT). The working section of this tunnel is 20 in. wide and 8 ft. long with a water depth of 21 in. ; the side walls of the tunnel are made of transparent plexiglass. Further details of the tunnel may be found in Ref. (36). The physical principles in the schlieren method of flow visualization are well known and may be found in Ref. (37). A schematic drawing of the optical set-up used for schlieren purposes in the FSWT is shown in Fig. 3. The light source used was an air cooled steady mercury vapor lamp which in conjunction with a gathering lens and slit arrangement as shown in Fig. 3 formed a point source. The position of the focusing lens and the film plate was such that a 5:1 magnification could be obtained with adequate illumination.

The first experiments were on a two inch hemispherical nose model and the density gradient required for the schlieren effect was accomplished by internal circulation of hot water with an inlet temperature of 130°F. The general arrangement and the position of the measurement of various temperatures to obtain heat transfer data are shown in Fig. 4.

Observations made with the continuous light source showed the existence of a laminar boundary layer separation on the hemispherical nose even at the highest tunnel velocity attainable in the FSWT (25 feet

per second). Photographs obtained with the help of a mechanical shutter which provided exposure time of 1/100 sec. did not show any of the details of the separated free shear layer or its subsequent reattachment process, if the latter did exist. To obtain such details the mercury vapor lamp was replaced by a spark gap source which had an exposure time of about 5 microseconds. The spark gap was made up of two brass disks each of 0.5 in. in diameter and 0.14 in. in thickness having a minimum clearance of about 0.2 in. A potential of 10-15 kilovolts applied to the disks provided a bright spark of the time duration noted. The spark so created was masked to provide a diffuse source light of about 0.2 in. × 0.14 in.. As shown in Fig. 3 this extended source was placed at the focus of the columnating lens. It may be mentioned that a cut-off plate is used in the schlieren apparatus as shown in Fig. 3. This plate had to be adjusted to obtain maximum contrast and sensitivity to provide photographs with small temperature differences needed in the present experiment. Shadowgraph pictures with little detail could be obtained at very low tunnel speeds by removing the cut-off plate but, they were not satisfactory at the speeds and temperature differences required of the contemplated experiment.

The photographs obtained with this schlieren system revealed clearly the laminar boundary layer separation; the short exposure time resolved some of the features of the subsequent turbulent reattachment process at these tunnel velocities and an early example is provided in Fig. 11.

With this initial success, further tests were carried out to estimate heat transfer requirements at higher tunnel velocities than used in the FSWT. With the help of an iron-constantan thermocouple imbedded at 60 degrees from the stagnation point on the model surface as shown in Fig. 4, it was concluded that a temperature difference of about 5°F is needed to produce visible schlieren effects. Heat transfer requirements to produce such a difference were estimated by measuring the temperature drop of the circulating hot water as a function of tunnel velocity. From these measurements it was predicted that for a two in. hemispherical nose with an afterbody similar to that shown in Fig. 4 a heat input of about 3000 BTU per hour would be required at a tunnel velocity of 60 feet per second. This in fact limited the velocity to be used for the subsequent experiments in the High Speed Water Tunnel (HSWT) to this value. This heat transfer requirement could just be met without great difficulty by electrical heating.

To test qualitatively the effect of temperature on the position of boundary layer separation, additional schlieren photographs were made with circulation of cold water with an inlet temperature of 50°F. As will be discussed in a later section there are no significant differences observed for the conditions of the subsequent tests.

It should be mentioned that the schlieren technique has been previously shown to work in water by Bland and Pelick[38] but they did not subsequently pursue the method.

Final Schlieren Set-Up: Success of the preliminary work prompted us to try the method in the HSWT. To provide a vibration free optical

system, the schlieren set-up was mounted on a platform suspended from the ceiling wall. Optical components used for the final set-up were the same as that used for the preliminary work, but with some modifications which will be considered next. Basically, the schlieren apparatus consisted of two light sources, one a short duration spark gap and the other, a steady mercury vapor lamp. The steady source was utilized for visual flow observations and also for focusing the optical system. A schematic diagram of the apparatus is shown in Fig. 5. The removable mirror shown in this diagram was used to align the spark gap system with the aid of the steady light source.

It may be noted from Fig. 5 that the windows of HSWT are cylindrical and not flat as in the FSWT. This introduces severe astigmatism which must be corrected to obtain acceptable schlieren photographs. This is accomplished by placing a plano convex lens on each of the tunnel side windows to remove first order astigmatism. In addition the plexiglass outer surface of the windows was not optically finished and had a pronounced "orange peel" surface which overwhelmed the sought for schlieren effect. This problem was overcome to a large extent by introducing a thin film of glycerine between the correction lenses and the window. For these reasons the quality of the photographs obtained in the HSWT were not as good as that obtained in the FSWT, but they were of sufficient quality to visualize the flow at all velocities.

A photograph of the apparatus on the light sources side is given in Fig. 6 and Fig. 7 shows the camera side.

The required heating of the models was accomplished by installation of a Thunderbolt kilowatt electric cartridge heater TB703 (supplied by the Vulcan Electric of ITT) within the model. Details are provided in Fig. 8.

2.2 Test Models

Two axisymmetric models widely utilized in cavitation inception studies and commonly known as Hemispherical nose and Swedish headform (or I. T. T. C. standard headform) were used in the present investigations. Details of the test bodies are shown in Figs. 9 and 10. The Swedish headform presently used is the same one used by Acosta and Hamaguchi in their inception studies detailed in Ref.(9). The test bodies were mounted in the axisymmetric test section of the HSWT[9, 36] by a three bladed sting support, which was about seven diameters downstream of the model nose. This mounting provided a rigid support for the model and during all tests no vibration or movement of the model could be discerned. The circular cross section of the tunnel was 14 inches in diameter, thus the models occupied less than two percent of the through flow area. The approximate angular misalignment between the model axis and tunnel axis was measured to be about 0.2° for both the test bodies. The models were cleaned with taluene before and after each test run.

2.3 General Experimental Procedures

Photographic Methods: Most of the photographs were taken under silhouette conditions, and the lens and film plate positions were such

that a magnification of 5:1 was obtained. Single exposure photographs were taken with the spark gap which had an exposure time of about 5 microseconds. This short time provided freezing action of the physical processes such as movement of cavitation bubbles and growth of instability waves on the separated free shear layer at all velocities, thus producing photographs with great clarity. Some photographs were taken with usual arc discharge lamps placed on the camera side of the tunnel as done in Ref. (9). High speed kodak 5 inches × 7 inches and 4 inches × 5 inches Royal x-pan sheet films with an ASA rating of 1250 were used for single exposure photographs.

Data from developed negatives concerning positions of boundary layer separation, cavitation separation and so on were obtained with the help of a negative containing nose of the model as a reference point and calibration factor obtained by photographing a scaled negative in the place of the model.

Some motion pictures of the cavitation bubble movements were taken with a Fastax camera at 4000 frames per second and few at 5000 frames per second. Framing rate was limited by the available intensity of the light at the recording film position to produce sufficient contrast on the developed negative. The light source used was a steady high pressure Peck 110 mercury vapor lamp. Motion picture studies were recorded with 16 mm kodak 2475 Recording Film and were developed in Accufine solution to obtain better contrast. Data from developed film concerning bubble sizes were obtained in a similar manner as in the case of single exposure negatives mentioned earlier.

Electrolysis Bubble Production: Use of electrolysis bubbles for flow visualization has been widely used but, in present studies it was decided to use these bubbles as source of artificial surface nuclei. For this purpose the whole model and the supporting sting were used as two terminals. A non-conducting adapter was utilized to electrically isolate the model from the sting assembly. A voltage pulse of 75 volts in magnitude and approximately 1 second in duration was applied between the terminals to produce the electrolysis bubbles. This produced a total current of 15 amperes in the circuit and a current density of about .2 amperes per square inch of the model surface.

Tunnel Operation: Pressure measurements for the computation of the free stream velocity and cavitation number were made with mercury manometers. As there is a boundary layer growth along the walls of the working section of the tunnel, it is necessary to calibrate the tunnel both bare and with a model installed in order to determine the static pressure and the velocity head at the location of the model. Such calibrations have been done by Acosta and Hamaguchi and their results are detailed in Appendix A of the Ref. (9). Working formulae for the computation of tunnel speed and cavitation number are given in the same Ref. (9), and these were utilized for present purposes for both the models. These corrections do not include blockage effects and may be justified from the computations of Hoyt[39], who has shown that for the Swedish headform when the model occupies about two percent of the through flow area (as is the case for present experimental conditions) the blockage effects are negligible.

Air content value of the tunnel water was held fixed at a value of about 10 PPM during all test runs. At the end of each day of testing, the air content value was measured with a Van Slyke blood gas analyzer. At this particular value of air content none or very few visible macroscopic air bubbles were seen in the water approaching the test model under all conditions. This being the consequence of the presence of a resorber in the present tunnel facility. Lower air content would have been preferable but could not be achieved due to a leak in the main seal of the pump.

All the tests were conducted at room temperature and the cavitation number was based on the vapor pressure at room temperature.

Method of Inception Observations: The incipient cavitation conditions were obtained by holding the tunnel velocity fixed and gradually reducing the tunnel static pressure until the presence of steady cavitation near or on the body was visually observed under the illumination of stroboscopic light. At this point all the manometer readings were recorded and single silhouette photographs were taken with the schlieren apparatus. By lowering the tunnel static pressure further, process of development of cavitation was photographed in a similar manner.

As mentioned earlier none or very few macroscopic bubbles were observed in the free stream approaching the test model; occasionally these cavitated near the model, but this type of cavitation was avoided and not recorded during present studies. In the terminology of Parkin and Kermeen on Page 29 of Ref. (22), present *incipient* conditions

may be termed "boundary layer incipient cavitation". No attempts were made to record desinent conditions.

3. EXPERIMENTAL RESULTS

Flow Visualization Under Fully Wetted Conditions: Figure 11 shows a schlieren photograph of laminar boundary layer separation bubble at a Reynolds number of 10^5 on a two inch hemispherical nose mounted in the FSWT. The top photograph in Fig. 12 shows the boundary layer separation when the surface temperature of the model is about 10°F below the free stream water temperature, whereas the bottom photograph illustrates the same phenomenon when the surface temperature is about 10°F above. Both photographs are at a Reynolds number of 2.5×10^5 and were taken in the same facility. As mentioned earlier the difference in temperature under heated conditions was measured directly, but under cooled conditions it is estimated from heat transfer measurements. Schlieren photographs in Fig. 13 were taken in the HSWT and are meant to show the behavior of laminar separation bubble with changes in Reynolds number and body shape. Also shown in Fig. 13 are two photographs taken without heating the test models at a tunnel velocity of 40 feet per second. Variation of measured laminar boundary layer separation position on the hemispherical nose with tunnel velocity is shown in Fig. 14. Similar results for the Swedish headform are shown in the next Fig. 15. These measurements were obtained from schlieren photographs and an example of the position of separation used is marked on the photograph (c) of Fig. 13 by an arrow and "S". Also included in Fig. 14 are results obtained from tests conducted in the FSWT on a different hemispherical nose than used in the HSWT. A plot of non-

dimensional axial distance from the point of separation to the disappearance of separated white line in the photographs of Fig. 13 as function of tunnel velocity is shown in Fig. 16. An example of point of disappearance used is marked on the photograph (i) of Fig. 13 by an arrow and "T". A measure of vertical extent of the laminar separation bubble was obtained from the measured value of the maximum height from the body surface to the separated white line in the photographs of Fig. 13. An example of this is provided in the photograph (ℓ) of Fig. 13 and is marked by "H_m". Variation of non-dimensional H_m with tunnel velocity is shown in Fig. 17 for the hemispherical nose and also for the Swedish headform.

Cavitation Inception Studies: Figure 18 provides a sequence of photographs illustrating the development of cavitation in the separated layer of the hemispherical nose at a velocity of 40 feet per second. Partial development at 60 feet per second is shown in the next Fig. 19. The dark patches above the model surface in the photographs of Figs. 18 and 19 represent the cavitating areas. Figure 20 shows two different kinds of incipient cavitation data for the hemispherical nose. The unfilled circles in Fig. 20 correspond to the incipient conditions as shown by the two top photographs of Figs. 18 and 19. The filled triangles correspond to the incipient conditions as shown by the third photograph of Fig. 18. Comparison of present data with that obtained by Kermeen[4] is shown in Fig. 20. Variation of incipient cavitation number for the Swedish headform with tunnel velocity is shown in Fig. 21. Comparison

of average data of Fig. 21 with that obtained in Ref. (9) is shown in the next Fig. 22.

Electrolysis Studies: Figure 23 shows a series of photographs illustrating the effect of producing artificial nuclei by electrolysis on the hemispherical nose at the same velocity of 28 feet per second, but at various cavitation numbers. The photograph marked "natural cavitation" is taken without the production of electrolysis bubbles. A similar set of photographs for the Swedish headform is shown in Fig. 24 These photographs were taken with the help of two arc dishcarge lamps located on the same side of the tunnel as camera and a silhouette photograph was superimposed on the same negative. The latter was done with the spark gap under fully wetted flow conditions. Next series of photographs in Fig. 25 were taken at about the same cavitation number, but, at different velocities.

Motion Picture Studies: Some interesting cavitation bubble motions in the separated layer of the hemispherical nose are shown in Figs. 26(a) and 26(b). Both series of photographs were taken at a velocity of 40 feet per second and cavitation number of 0.74. At the top of the sequence is a schlieren photograph showing the boundary layer separation at 40 feet per second. These photographs were obtained with the spark source and by turning the film manually frame by frame. Sequence of disappearance of cavitation on the Swedish headform at 40 feet per second and approximate cavitation number of 0.46 is shown in Fig. 27. The schlieren photograph at the top of the sequence is at 30 feet per second.

4. DISCUSSION OF FULLY WETTED FLOW OBSERVATIONS

Position of Boundary Layer Separation: Effectiveness of the schlieren method as flow visualization technique is clearly illustrated in the photograph of Fig. 11. It shows the position of boundary layer separation, and also the process of reattachment of the separated free shear layer to form a laminar separated bubble.

Measurements shown in Fig. 14 illustrate that the position of boundary layer separation did not alter with change in surface temperature of the model for all test velocities in the FSWT. Similar results were observed concerning the extent of separated bubble as may be seen from the photographs of Fig. 12. The observed difference in the break up mechanism of the free shear layer is not due to the temperature difference, but is an inherently unsteady property of the separated layer. Thus within the range of temperatures used to create the schlieren effects, the position or the extent of laminar separated bubble was not influenced by heating or cooling of the model.

As may be seen from the set of photographs in Fig. 13, both hemispherical nose and Swedish headform possessed laminar separation bubble at all the test velocities in the HSWT. The highest test velocity corresponds to a Re_D of 9.06×10^5 for the hemispherical nose and Re_D of 8.78×10^5 for the Swedish headform. To help distinguish the separated white line in the photographs of Fig. 13, two photographs taken without heating of the model are included at the top of the sequences.

From Fig. 14, it may be seen that the position of laminar boundary layer separation on the hemispherical nose mounted in both the

HSWT and FSWT is about 87° from the stagnation point. To avoid free surface effects in the FSWT, the model was submerged about 6 diameters below the surface. It should be noted that two different models were utilized in the two different tunnels whose characteristics (such as free stream turbulence levels) are not completely known and may be different. In both tunnel facilities the position of separation on the hemispherical nose did not change appreciably with increase in velocity, the change being within the error of experimental measurements. As seen from Fig. 15, for Swedish headform s/D at separation is equal to 0.82 at a velocity of 20 feet per second and increases to 0.84 at a velocity of 60 feet per second.

Length of Separated Bubble: In almost all the photographs of Fig. 13, the separated white line begins to form into a wavy line and subsequently either disappears or becomes very faint. Since the schlieren effects are a measure of the density gradients (in this case induced by temperature gradients) disappearance of the separated white line may be interpreted as vanishing of these gradients due to turbulent mixing. The distance from the position of separation to the point of disappearance of the separated white line may be used as a convenient measure of the length of the separated bubble. Variation of such distance with velocity for both the test models is shown in Fig. 16. As expected the bubble length decreases with increase in velocity for both the models. Physically for both the models these bubble lengths were quite small, being only 12 percent of the diameter at 20 feet per second ($Re_D \doteq 3.02 \times 10^5$)

and about 4 percent at 60 feet per second ($Re_D \doteq 9 \times 10^5$).

Some Comparisons With Wind Tunnel Data: Length of separated bubble- L_r for both the models in terms of appropriate non-dimensional variables- $Re^*_{\theta_s}$, L_r / θ_s is shown in Fig. 28. The value of the momentum thickness at separation-θ_s was estimated by Thwaite's method as outlined in Appendix A. Also shown in Fig. 28 is data obtained by Gaster[40] in his wind tunnel studies concerning laminar separation bubbles which were created on a flat plate with the help of an auxilary airfoil. Distance from the position of separation to a downstream point where velocities close to the wall become significantly larger (say a tenth of the free stream velocity) was used as a measure of length of the separated bubble. Gaster refers to this distance as "dead air region" and measurements of L_r were obtained with the help of detailed velocity and pressure measurements. Favorable comparison with Gaster's data indicates that present basis and method of obtaining the length of separated bubble is quite adequate. It can also be inferred from Fig. 28 that L_r / θ_s is slowly varying, but primarily a function of $Re^*_{\theta_s}$.

Height of the Separated Bubble: As seen from Fig. 13, on present bodies the height of the separated bubble from the model surface essentially starts with a value of zero and gradually increases to a maximum value - H_m at the end of the separated region. From Fig. 17, it is seen that H_m decreases with increase in velocity for both the models. The largest physical value of H_m indicated by the schlieren photographs is only about one hundredth of the body diameter.

Measurements shown in Fig. 17 are within 25 percent accuracy. A replot of Fig. 17 in terms of appropriate non-dimensional variables - $Re^{*}_{\theta_s}$, H_m/θ_s is shown in Fig. 29. At a large Reynolds number of about 8.8×10^5, on the Swedish headform the maximum separated height is only twice the value of estimated momentum thickness at separation. The pertinent point to note here is that at the same Reynolds number the observed maximum separated height on the hemispherical nose is two to three times larger than on the Swedish headform; this being the case for all the test Reynolds numbers.

A Remark on Measurement of Data From Schlieren Photographs: In present experiments, height of the separated white line in the photographs of Fig. 13 is not a true measure of the actual separated height. The exact relationship between the two is a function of the optical set-up. Similar problems are encountered in locating the actual shock position from schlieren photographs in the field of compressible aerodynamics[37]. These problems arise only with measurements which are normal to the plane of the knife edge. The quantities measured which are in parallel with the plane of the knife edge reflect a true measurement. Thus, the results shown in Figs. 14 and 15 indicate the true position of the boundary layer separation. Similar arguments hold for the results in Fig. 16, but only comparative studies regarding the separated height shown in Fig. 17 may be made.

Comparison With Approximate Computations: As outlined in Appendix A, some theoretical estimates of the position of boundary layer separation

using Thwaites approximate method were made. For the hemispherical nose the predicted value was found to be 87° and agrees very well with the observed value of 87° in both HSWT and FSWT. Predicted value of s/D at separation for the Swedish headform was found to be 0.82 for all Reynolds numbers whereas, the observed value changes from 0.82 to 0.84 with increase in Re_D from 2.7×10^5 to 8.78×10^5.

It is well known that at high enough Reynolds number, attached laminar boundary layers possess a point of instability after which the outside disturbances grow exponentially in amplitude until transition to turbulence sets in. A semi-empirical method developed by Smith and his associates[41] enables one to estimate the approximate position of transition and use of this method to predict transition on present bodies is detailed in Appendix B. The Reynolds number at which transition is to occur at the position of laminar boundary layer separation may be referred to as a "critical Reynolds number" designated by "$Re_{D_{crit}}$". Presumably for $Re_D > Re_{D_{crit}}$, no laminar boundary layer separation is possible. Roshko[42] refers to this Reynolds number as "second critical Reynolds number" and finds it to be about 5×10^6 for the case of a cylinder in rectilinear flow. Present computations from Appendix B indicate that $Re_{D_{crit}} \doteq 5 \times 10^6$ for the hemispherical nose and that $Re_{D_{crit}} \doteq 1.5 \times 10^6$ for the Swedish headform. This is in accord with present experimental observations that the boundary layer is still laminar at separation at a $Re_D \doteq 9 \times 10^5$ for the hemispherical nose and at a $Re_D \doteq 8.7 \times 10^5$ for the Swedish headform. During the present experiments it was not possible to attain critical Reynolds number for either

of the models, however it is noteworthy to point out that the length of the separated bubble decreased with increase in Re_D and length was only 4 percent of the model diameter at $Re_D \doteq 8.7 \times 10^5$ for the Swedish headform.

From pressure measurements on the hemispherical nose Rouse[43] indicates that $Re_{D_{crit}} \doteq 2 \times 10^5$, whereas from present experiments $Re_{D_{crit}}$ is found to be greater than 9×10^5. It is believed that this discrepancy has resulted from the use of pressure taps with a spacing of 12.5 percent of the body diameter by Rouse in the measurement of the pressure distribution. As may be seen from Fig. 16, the method of pressure distribution measurement by Rouse would not indicate the possibility of laminar separation for $Re_D > 10^5$.

5. DISCUSSION OF INCEPTION STUDIES

5.1 Hemispherical Nose

Visual Observations: Onset of cavitation took place in the form of a ring of macroscopic bubbles around the nose of the model. This type of inception may be termed "steady incipient bubble cavitation" following Kermeen's[4] description of desinent cavitation. Close observation indicated the presence of microscopic bubbles ahead of the macroscopic ones confirming similar observations by Parkin and Kermeen[4,22] on the same type of test body. As tunnel pressure was lowered further, cavitation bubbles became more profuse until a clear macroscopic attached cavity was formed on the model surface. This state of cavitation is termed "band inception". The small microbubbles characterizing the incipient bubble cavitation disappear although at the terminus of the attached cavity such bubbles are again seen. Kermeen[4] refers to this form of cavitation as "steady attached cavitation". The development just described was found to take place for all the test velocities used between 25 to 60 feet per second. This corresponds to Re_D between 3.78×10^5 to 9.06×10^5.

Relationship Between Boundary Layer Separation and Inception: With the help of the schlieren method it was possible to observe the inception process and the nature of real fluid flow past the model simultaneously. As can be seen from the photographs of Figs. 18 and 19, the entire process of inception takes place within the separated region. From photographs 18(a) and 19(d), it is evident that the first visible

macroscopic cavitation occurs in the transition region of the separated free shear layer (as mentioned earlier disappearance of the separated white line is taken to be beginning of the transition). As illustrated in the photographs 18(b) and 19(e), reduction in σ produces increasing amounts of macroscopic cavitation; at the same time the presence of microscopic bubbles starting from the position of laminar separation becomes apparent. Further reduction in σ results in the formation of a single macroscopic attached cavity as shown in the photograph 18(c) which also shows the disappearance of the incipient bubble cavitation observed in the earlier photographs. It may be noted here that the position of laminar separation has been shifted upstream by the presence of the cavitation.

It should be noted from the photographs 18(a) and 19(d) that the diameters of the macroscopic bubbles is approximately equal to the maximum separated height - H_m. Measurement of bubble sizes at 40 feet per second indicated that the macroscopic bubbles were of the order of 0.01 in. in diameter and the microscopic bubbles were of the order of 0.0025 in. in diameter. These values are in agreement with the previous measurements of Parkin and Kermeen[4, 22].

From the photograph in Fig. 18(a), it is important to note that inception of cavitation <u>does not</u> take place in the neighborhood of the minimum pressure point which is expected to lie upstream of the position of laminar separation.

<u>Further Details From Motion Picture Studies:</u> To get further detailed information about the inception process some motion pictures of

cavitation in the separated layer were taken at 4000 frames per second, and some of these are shown in the sequential photographs of Figs. 26(a) and 26(b). These photographs were taken at a tunnel velocity of 40 feet per second and a σ of 0.74. Also included at the top of the sequences are schlieren photographs taken at the same velocity and to the same scale. From frame-by-frame study of these motion pictures it could be deduced that both macroscopic and microscopic cavitation bubbles orginated in the transition region of the separated layer; the larger macroscopic bubbles were detached from the model surface to be collapsed downstream and the smaller microscopic bubbles before they could grow further were entrained in the reverse flow of the separated region and traveled upstream towards the position of the separation at about a velocity of one ft/sec. as compared to free stream velocity of 40 ft/sec. At present framing rates it was not possible to track the bubbles further. Parkin[22] however observed velocities of these small bubbles once in the free shear layer to be between 12 to 26 ft/sec.

These events were the ones most often observed but there were others with a different history. A few bubbles were observed to grow in the separated layer at a fixed position on the body surface as also observed by Parkin and Kermeen[22]; if the growth took place near the position of separation the bubbles became entrained into the free shear layer after growing to a size equal to that of the local separated height. If the growth took place downstream from the position of separation the bubble motion was similar to that described initially for the bubbles

which started from the transition region. Some bubbles were seen to circulate twice in the separated region before they were entrained in the free shear layer and others were seen to start from the transition region to be transported upstream for a distance after which they were swept downstream although still within the separated region. An example of this is shown in the photographs of Fig. 26(b). The important point to note from these complex bubble motions is that residence time of the bubbles in the separated region was estimated to be from 1 to 5 milliseconds and during this period they did not show any appreciable growth. The bubbles which grew at a fixed position on the model surface also had a growth time of the order of few milliseconds as also observed by Parkin and Kermeen but the growth of bubbles in the transition region was quite rapid and could not be photographed in any detail during present studies. Kermeen[4] indicates the growth time of these latter bubbles to be shorter than even a tenth of a millisecond.

Interpretation of Parkin's Observations: From the similarity of the present observations and those formerly carried out by Parkin[22] we may make the following important points

(a) microscopic bubble growth fixed on the body surface as observed in Parkin's experiments occurred in the laminar separated zone and not submerged in the attached boundary layer as reported by Parkin,

(b) stabilization of these bubbles occurred since they were in the separated zone, a region of very low velocities

and not due to pressure gradient forces as thought of by Parkin and subsequently considered by Holl[25] and Van der Walle[26] in inception scaling theories,

(c) upstream motion of these bubbles as observed by Parkin were due to the reverse motion of the fluid in the separated zone and not due to adverse pressure gradient effects as thought,

(d) it is mentioned in Parkin's report[22] that the macroscopic bubbles are sustained by the microscopic bubbles upstream, but present experiments indicate that the macroscopic and microscopic bubbles grew independently of each other,

(e) after a clear attached cavity was achieved, Parkin observed the suppression of the microscopic bubble growth. It is believed that this is due to the filling of the fully wetted separated layer with the cavity leaving only a small distance of about .02 in. between the position of viscous separation and the beginning of the cavity which may be seen in the photograph (c) of Fig. 18. Upstream secondary bubble motion observed by Parkin and shown in the Fig. 14 of Ref. (22) is, in fact, within this small region.

It should be mentioned that primarily the method of flow visualization differed between the present experiments and that conducted earlier. The dye streak method used by Parkin was not adequate to show the existence of a small laminar separation bubble; instead this

region was thought to be the transition region of the attached boundary layer.

Cavitation Inception Measurements: From Fig. 20, σ_i increases with increase in velocity for both bubble and band types of inception. Since inception was seen to occur downstream of the position of laminar separation, naturally the important pressure coefficient to compare σ_i with would be the negative value of the pressure coefficient at separation, $-c_{p_s}$. The value of $-c_{p_s} = .63$ shown in Fig. 20 is obtained with the help of pressure distribution measurements made by Kermeen[4] and the known value of the position of separation in the HSWT shown in Fig. 14. Also shown in Fig. 20 is the value of $-c_{p_{min}} = .74$.

It should also be noted that σ_i for incipient bubble cavitation at all test velocities is greater than $-c_{p_s}$, indicating that cavitation took place at local static pressures higher than the vapor pressure. This is suggestive that either gaseous cavitation was observed or the strong pressure fluctuations in the transition region were responsible for vaporous cavitation. From motion picture studies one may rule out the possibility of steady gaseous diffusion as the mechanism for the bubble growth, since the residence time of the cavitation bubbles was relatively short and this point has been discussed by Parkin[22] in some detail. It seems possible that a combination of convective gaseous diffusion[44], rectified gaseous diffusion[45] and vaporous cavitation could be responsible for the growth of macroscopic bubbles in the transition region.

For vaporous cavitation the pressure fluctuations would have to be of the order of 12 percent of the dynamic head at 30 feet per second and 25 percent of the dynamic head at 60 feet per second. Since no pressure fluctuation measurements under the present type of flow situations are available, further discussion on the origination of cavitation bubbles in the transition region would be of speculative nature.

It may be noted from Fig. 20 that band type of inception also occurs for $\sigma_i > -c_{p_s}$ indicating that this type of inception is definitely of gaseous type.

Comparison with Kermeen's Data: From Fig. 20, Kermeen's[4] data of desinent cavitation is in poor agreement with present values of σ_i for incipient bubble cavitation, but is in good agreement with present values of σ_i for incipient band cavitation. From Kermeen's report it is known that the desinent cavitation was of the bubble type, but the state of cavitation could either be that represented by Fig. 18(a) or Fig. 18(b). In fact, in Fig. 20 the uppermost value of the unfilled circle represents the upper bound of σ_i for incipient bubble cavitation, whereas the triangular filled values represent the lower bound. A better comparison with Kermeen's data will be made later in Section 6 and is shown in Fig. 30.

Before any comparison with Kermeen's results is made, it should be made certain that the position of laminar separation did not differ appreciably in the two cases. Of course, there is no direct evidence of the above point but there is some indirect evidence. In

Fig. 24 of Ref. (4) a photograph is shown with macroscopic cavitation and also microscopic cavitation ahead of it; the starting position of the latter is mentioned to be 88.7° from the stagnation point. The present studies show (see Fig. 18(b)) the same type of cavitation and the starting position of the microscopic bubbles is seen roughly to coincide with the position of the boundary layer separation. Thus, with this observation in mind, the position of the boundary layer separation in Kermeen's work must be taken to be about 88° as compared to 87° observed on the present model. In this event $-c_{p_s}$ in Kermeen's case would then be about 0.6.

5.2 Swedish Headform

Observations of Inception: Inception was always sudden and in the form of a fully developed cavity or was of band type. Typical photographs of inception are shown in (d) of Fig. 24 and also (d) of Fig. 25. An important point to note is that inception takes place in the neighborhood of the position of the boundary layer separation ($s/D \doteq .83$) which lies considerably downstream of the position of minimum pressure point[43] ($s/D \doteq .62$). This was the case for all the test velocities which ranged from 25 to 60 feet per second, corresponding to Re_D of 3.66×10^5 to 8.78×10^5. Motion pictures taken at 4000 frames per second of cavitation in the separated layer produced only sketchy details of the inception process. A large macroscopic bubble would suddenly appear in the separated region on a frame of the motion picture film and by the next frame a fully developed cavity would be formed. However, some details of the desinent cavitation were observed as shown in the photographs of Fig. 27 taken at a velocity of 40 ft/sec and $\sigma \doteq .46$. It may be

seen that last traces of cavitation exist in the transition region of the separated free shear layer. It would be too premature to conclude from this that inception also took place in the transition region of the separated free shear layer even though on the hemispherical nose inception and desinence were observed to take place in the same region of the flow.

Cavitation Inception Measurements: From Fig. 21, except at a velocity of 30 feet per second the inception indexes reproduce quite well. At 30 feet per second considerable scatter exists. Comparison of the average data of Fig. 21 with that obtained by Acosta[9] on the same Swedish headform is shown in the next Fig. 22. The comparison is very good except at a velocity of 30 feet per second and at this velocity the difference in the $\overline{\sigma}_i$ is about .04. It is also seen that $\overline{\sigma}_i$ increases with increase in velocity; this trend was also observed for the case of the hemispherical nose.

Comparison of $\overline{\sigma}_i$ with $-c_{p_s}$: Also shown on Fig. 22 is the negative value of the pressure coefficient at separation which is obtained with the help of pressure distribution measurements made by Rouse[43] and the observed position of the boundary layer separation from Fig. 15. It should be noted that $\overline{\sigma}_i$ is closely related to $-c_{p_s}$ rather than $-c_{p\,min}$ which is .6 for the Swedish headform. The difference between $\overline{\sigma}_i$ and $-c_{p_s}$ starts with a value of about 0.075 at a velocity of 26 feet per second and gradually decreases to zero at a velocity of 51 feet per second.

6. IMPORTANT PHYSICAL PARAMETERS FOUND IN INCEPTION

We have seen on both test bodies inception of cavitation to be influenced by the presence of the laminar separation. However, inception characteristics were different in the sense that $\sigma_i > -c_{p_s}$ for the hemispherical nose and $\sigma_i < -c_{p_s}$ for the Swedish headform in the same Reynolds number range. An attempt will be made to explain the above mentioned difference from schlieren observations shown in Fig. 17.

As mentioned earlier in section 4 one of the principle differences in the nature of real fluid flow past the two bodies was in the observation that height of the separated layer for the case of the hemispherical nose was 2 to 3 times larger than for the case of the Swedish headform.

This difference in height may influence the magnitude and frequency of the pressure fluctuations in the transition region of the separated free shear layer and at least for the hemispherical nose inception was seen to occur in this region. Gaster[40] has conducted some qualitative investigations of the above mentioned point, for example he observed that dominant unstable frequency in the attached boundary layer upstream of separation was about 200 cycles per second, but on the free shear layer it was observed to be about 1000 cycles per second. Detailed measurements of pressure fluctuation needed for present analysis are not available, thus the reasoning has to be speculative in nature.

Present observations indicate that vertical extent of the laminar separated region significantly controls the maximum size of the bubble

which may reside in the region. From motion pictures of the electrolysis bubbles, the following information was obtained which may help understand the above point:

Model	U	d_m in.	τ_r sec.	H_m in.
Hem. Nose	30	2.5×10^{-3}	6.5×10^{-3}	.012
"	40	2×10^{-3}	4.4×10^{-3}	.0084
Swed. Head.	30	1.1×10^{-3}	6.6×10^{-3}	.005

where d_m is the maximum diameter of the bubble stabilized in separated zone in inches, τ_r is the residence time of the above bubble in seconds, and H_m is the maximum separated height from Fig. 17.

It may be seen that d_m is proportional to H_m. It should be seen that for vaporous cavitation to occur at $P = P_v$ the diameter of the bubble should be greater than 10^{-3} in.[14]. Still the conditions which determine the origination of the microscopic bubbles without electrolysis remains to be found. It is these conditions which may determine the incipient conditions and not the actual magnitude of d_{max} even though latter may be important for visual method of determining inception. From Fig. 17, for both models, d_m decreases with increase in velocity and thus one may expect σ_i to decrease with increase in velocity, but this is contrary to the observations of Figs. 20 and 22. From this one may conclude for the present Reynolds number range, that the height of the separated layer probably plays an important role in determining the magnitude of pressure fluctuation in the transition region which in

turn might determine the value of σ_i. But this may not hold true in generality.

Under any circumstance, separation does influence the process of inception significantly. The importance of c_{p_s} has been brought about earlier and with this in mind a new cavitation inception coefficient is hereby proposed

$$\sigma_i^* = -\frac{(c_{p_s} + \bar{\sigma}_i)}{(1-c_{p_s})}$$

with expected additional important parameters of the Reynolds number based on momentum thickness at separation -$Re^*_{\theta_s}$, and possibly an additional length parameter, say H_e/θ_s where H_e is a relevant length. It is tempting to think that this length might be proportional to maximum height of the separated layer although there is now no such basis to determine such a length.

Average inception data from present studies on the hemispherical nose (incipient band cavitation), Swedish headform, Acosta's data[9] and Kermeen's data[4] are plotted in terms of σ_i^* versus $Re^*_{\theta_s}$ in Fig. 30. Kermeen's data is taken from Fig. 22 corresponds to the values when clear steady attached cavity was first formed or according to present terminology when band type inception occurred. Therefore, it may be seen now that when known state of cavitation is the same in Kermeen's and the present case the corresponding $\bar{\sigma}_i$ values agree quite well. The method of obtaining $-c_{p_s}$ for the hemispherical nose in Kermeen's case was discussed in Section 5.1. If it is band type inception and the corresponding value of σ_i^* is negative, then it may be concluded that the

type of cavitation is gaseous in nature. This being the case for the hemispherical nose cavitation observed in the present and Kermeen's case.

We have seen that cavitation inception process is influenced by the presence of a laminar separation on a certain class of bodies and under these conditions σ_i may be considerably different from $-c_{p\,min}$. Furthermore, it is also observed that for such bodies depending on the shape, σ_i may be closely correlated with $-c_{p_s}$. But, from the present experimental program no explanation is found for the observed size effect on σ_i for geometrically similar bodies of certain shape for a fixed Reynolds number. Examples of such dependence are well known and, in particular, Parkin and Holl[5] have observed this effect on a hemispherical nose and a 1.5 calibre ogive. However, it is believed that proper foundations have now been laid by the present experimental program to address the above mentioned size effect in future work.

7. SUGGESTED CORRELATION TO PREDICT σ_i FOR BODIES WITH ATTACHED BOUNDARY LAYERS

It is well known that attached laminar boundary layer and also laminar separated free shear layer possess a point of instability after which the outside disturbances grow exponentially in amplitude. The rate of growth in general is determined by the local Reynolds number and local pressure gradient forces. Such spatial growth of disturbances can be computed for an attached laminar boundary layer with the help of recent computations made by A. M. O. Smith[46]. It has been proposed empirically[41] that if the amplitude of the initial disturbances grows by a factor of $\exp^7$ to $\exp^9$, transition takes place and the boundary layer becomes turbulent. Detailed calculations with the help of results from Ref. (46) in determining the position of boundary layer transition using above criterion is explained in Appendix B. Using such calculations the position of transition has been estimated as a function of Re_D for a 1.5 calibre ogive with cylindrical afterbody. $Re_{D\,crit}$ for 1.5 calibre ogive is estimated to be 6.3×10^5; comments regarding the importance of $Re_{D\,crit}$ have been made earlier in section 4. Thus, after knowing the position of transition and pressure distribution on the headform[43], one can determine the value of the pressure coefficient at the position of transition (designated by $c_{p_{tr}}$). Variation of $c_{p_{tr}}$ with Re_D for 1.5 calibre ogive is shown in Fig. B.5 of Appendix B.

A comparison of $-c_{p_{tr}}$ and desinent cavitation number σ_d for a two inch 1.5 calibre ogive taken from Ref. (5) is shown in Fig. 31. These

results show the close correlation of σ_d with $-c_{p_{tr}}$.

The above finding is yet to be verified by direct experiments. However, in the case of separated flows, inception of cavitation was related to the transition region of the separated free shear layer, a region of strong pressure fluctuations. Thus, the comparison afforded in Fig. 31 suggests that the somewhat similar fluctuations in the transition region of the boundary layer might also be responsible for cavitation inception on bodies not having a laminar boundary layer separation.

8. DISCUSSION OF ELECTROLYSIS STUDIES

Swedish Headform: We have seen in Fig. 22 that σ_i for the Swedish headform was considerably lower than $-c_{p\,min}$ and in some cases even lower than $-c_{p_s}$. The above observation indicates that just prior to incipient conditions liquid in the neighborhood of the minimum pressure point is under an actual tension. It seemed possible when this work was started that this tension could not be supported if an abundant supply of surface nuclei formed by electrolysis were to be made available. To investigate this aspect of cavitation inception such nuclei were provided at three different levels of tunnel pressure at a constant velocity of 30 ft/sec. At this velocity σ_i under natural conditions was found to be about 0.427, and photograph (d) of Fig. 24 illustrates this condition.

The first experiment was carried out at a cavitation index of $\sigma = 0.852$ which is greater than $-c_{p\,min}$, $-c_{p_s}$ and σ_i. It may be seen from Fig. 24(a) that the electrolysis bubbles do not show any growth, but they reside in the separated zone much longer than anywhere else on the model. From motion picture studies it could be deduced that bubbles larger than about 10^{-3} in. in diameter stayed less than 10^{-4} seconds in the separated zone except one bubble which was noticed to be entrained in the reverse flow and its residence time was found to be about 5 milliseconds.

The second test was carried out for a value of $\sigma = 0.544$ which is less than $-c_{p\,min}$ but greater than $-c_{p_s}$ and normal σ_i; from (b) of Fig. 24, it may be seen that electrolysis bubbles cavitated readily

starting from the minimum pressure point.

The third and last value $\sigma = .437$ was less than $-c_{p\,min}$ and $-c_{p_s}$ but is still greater than σ_i; from (c) of Fig. 24, profuse cavitation from electrolysis bubbles starting from the minimum pressure point is apparent. However, the presence of electrolysis bubbles did not trigger a steady cavity and the cavitation observed completely disappeared as soon as the production of electrolysis bubbles was stopped.

Similar results were observed at other velocities except the physical appearance of cavitation from electrolysis bubbles, as illustrated in the photographs of Fig. 25, changed with increase in velocity. In Fig. 25(a), at 30 feet per second cavitation occurred as isolated, large, macroscopic bubbles. At a velocity of 55 feet per second, as shown in Fig. 25(c), streaks were exhibited and at an intermediate velocity of 40 feet per second both types are observed simultaneously as may be seen in Fig. 25(b).

Hemispherical Nose: From Fig. 23(a), it may be seen that for $\sigma > \sigma_i$ but less than $-c_{p\,min}$, electrolysis bubbles do cavitate only in the transition region of the separated free shear layer as was the case under natural incipient conditions. For a slightly lower σ, cavitation is also observed in the minimum pressure area as shown in Fig. 23(b). In Fig. 23(c) a photograph of cavitation for $\sigma < \sigma_i$ under natural conditions is shown and it may be observed that cavitation is in the separated layer and thus begins downstream of the minimum pressure point as previously discussed. The next photograph Fig. 23(d) shows that

electrolysis bubbles readily cavitate starting from approximately the minimum pressure point at the same value of σ.

Remarks: It may be said from the above studies that with a steady supply of sufficient nuclei one can, in fact, observe steady cavitation when $\sigma \doteq -c_{p\,min}$, and this relationship may be used to determine $-c_{p\,min}$ for complex flows. On the Swedish headform, just prior to inception, a considerable portion of the liquid is at pressures below vapor pressure, but even under these conditions a momentary supply of artificial nuclei did not trigger a steady attached cavity. Only reduction of σ to σ_i produced a steady attached cavity.

9. CONCLUSIONS AND SUMMARY

A schlieren method of flow visualization widely used in the field of compressible aerodynamics has been successfully used for the same purpose in water tunnel experiments. This method has shown the hemispherical nose to have a viscous laminar boundary layer separation at a $Re_D = 9.06 \times 10^5$ and the Swedish headform to have separation at a $Re_D = 8.78 \times 10^5$. Approximate boundary layer stability calculations indicate $Re_{D\,crit} \doteq 5 \times 10^6$ for the hemispherical nose as opposed to previous $Re_{D\,crit} \doteq 2 \times 10^5$ indicated by Rouse[43] and used heretofor by all researchers in the area of cavitation inception. Similar calculations indicate $Re_{D\,crit} \doteq 1.5 \times 10^6$ for the Swedish headform. The length of the laminar separated zone on both the models decreased monotonically with increase in Reynolds number.

On the hemispherical nose, cavitation inception in the form of cavitation bubbles was seen to first occur in the transition region of the separated free shear layer. With reduction in σ the viscous separated region was observed to fill with the cavitation bubbles until a clear attached cavity was formed. Present observations regarding cavitation inception on a hemispherical nose strongly indicate that similar observations by Parkin were within the viscous separated region and <u>not</u> submerged in the attached boundary layer as was formerly thought.

On the Swedish headform cavitation inception in the form of a clear attached cavity was seen to take place within the separated region.

For bodies with viscous laminar separation the important pressure coefficient to correlate σ_i with is found to be the negative value of the c_p at the point of laminar separation, $-c_{p_s}$. Other important parameters found were Reynolds number and a length parameter which is a measure of the height of the viscous separated layer.

For the Swedish headform σ_i compared favorably with $-c_{p_s}$ and inception always occurred for $\sigma_i \leq -c_{p_s}$; the equality sign to hold true at high Reynolds numbers. For the hemispherical nose, inception always occurred for $\sigma_i \geq -c_{p_s}$; it is believed the turbulent fluctuations in the transition region of the separated layer and gaseous type of cavitation may be responsible for the above observation.

From present experiments no explanation could be offered for the observed size effect on σ_i for geometrically similar bodies at fixed Reynolds numbers. The schlieren method may be useful in shedding light on this question in future work.

Computation of the pressure coefficient at transition, $c_{p_{tr}}$, on 1.5 calibre ogive for $Re_D > Re_{D\,crit}$ when viscous laminar separation is absent, has shown that $\sigma_d \doteq -c_{p_{tr}}$. This finding has yet to be verified experimentally.

LIST OF FIGURE CAPTIONS - PART I

Fig. 1. Cavitation inception number versus velocity at maximum acoustic pressure for a series of 6 hemispheres with cylindrical afterbody of diameter-D (Ref. 4).

Fig. 2. Results of a comparative cavitation inception tests on a modified ellipsoidal headform sponsored by the International Towing Tank Conference. Taken from Fig. 8 of Ref. (7).

Fig. 3. Schematic drawing showing the schlieren set-up in the Free Surface Water Tunnel.

Fig. 4. Schematic diagram showing the mounting of a two inch hemispherical nose in the Free Surface Water Tunnel. Additionally the different places of temperature measurements to obtain heat transfer data are shown.

Fig. 5. Schematic diagram of the schlieren set-up in the High Speed Water Tunnel.

Fig. 6. Illustration of light source side of the schlieren system. On the far right is the spark gap source, followed by deflecting mirror and columnating lens. The white box on the far left is the steady light source. A plano convex correction lens is shown taped on the tunnel window.

Fig. 7. Illustration of camera side of the schlieren system. In this figure the first lens is the focusing lens, followed by the cut-off knife edge placed just before the camera box itself. The camera box is 80 in. long.

Fig. 8. A drawing showing the details of placing the electric heater inside the Swedish headform. The dark shaded area is the heater.

Fig. 9. Diagram showing the geometrical details of the Swedish headform.

Fig. 10. Diagram showing the geometrical details of the hemispherical nose.

Fig. 11. A schlieren photograph showing the laminar separation bubble on a two inch hemispherical nose at a Reynolds number of 10^5. The flow is from right to left. Also noticed is the gradual break-up of the separated free shear layer and its subsequent reattachment to the model surface.

Fig. 12. Photographs illustrating, that the position or extent of laminar separation is not influenced by the change of model surface temperature. Top photograph is with surface temperature about 10°F below the free stream water temperature and the bottom is with surface temperature about 10°F above. Both photographs are of a two inch hemispherical nose at $Re \doteq 2.5 \times 10^5$.

Fig. 13. Schlieren photographs illustrating the change in extent of laminar separation bubble with increase in tunnel velocity or Reynolds number for both the test models. The top two photographs (a) and (g) are taken with no model heating at a tunnel velocity of 40 ft/sec. (a) $Re_D = 5.85 \times 10^5$, (b) $Re_D = 2.93 \times 10^5$, (c) $Re_D = 4.39 \times 10^5$, (d) $Re_D = 5.85 \times 10^5$, (e) $Re_D = 7.31 \times 10^5$, (f) $Re_D = 8.78 \times 10^5$, (g) $Re_D = 6.04 \times 10^5$, (h) $Re_D = 3.02 \times 10^5$, (i) $Re_D = 4.53 \times 10^5$, (j) $Re_D = 6.04 \times 10^5$ (k) $Re_D = 7.55 \times 10^5$, (ℓ) $Re_D = 9.06 \times 10^5$.

Fig. 14. Variation of laminar boundary layer separation position on the hemispherical nose with tunnel velocity. Also shown is the effect of temperature change on the position of separation.

Fig. 15. Variation of the position of boundary layer separation on the Swedish headform with change in tunnel velocity.

Fig. 16. Variation of the length of the laminar separated bubble estimated from schlieren photographs with tunnel velocity for both the test models.

Fig. 17. Variation of the maximum height of the laminar separated bubble indicated by the schlieren photographs with velocity for both the test models.

Fig. 18. Sequence showing the progressive development of cavitation on the hemispherical nose in the laminar boundary layer separated region at a tunnel velocity of 40 ft/sec. corresponding $Re_D = 6.04 \times 10^5$. The dark patches above the model surface are cavitating areas.

Fig. 19. Partial sequence showing the progressive development of cavitation on the hemispherical nose in the separated region at a tunnel velocity of 60 ft/sec. corresponding $Re_D = 9.06 \times 10^5$

Fig. 20. Variation of cavitation inception number wtih tunnel velocity on the hemispherical nose for two types of incipient conditions. Also included are Kermeen's data.

Fig. 21. Variation of cavitation inception number for the Swedish headform with tunnel velocity. Inception was always of the "band" type.

Fig. 22. Comparison of present average cavitation inception data with that obtained by Acosta[9] on the same Swedish headform and also with the negative value of the pressure coefficient at laminar separation.

Fig. 23. Sequential photographs illustrating the effect of introducing artificial surface nuclei by electrolysis on the hemispherical nose at different tunnel pressures. The photograph (c) is under natural cavitating conditions. U = 28 ft/sec., $\sigma \doteq .72$, $-c_{p\,min} \doteq .74$, $-c_{p_s} \doteq .63$.

Fig. 24. Photographs illustrating the effect of introducing artificial surface nuclei by electrolysis on the Swedish headform at different tunnel pressures. Cavitation observed in photographs (b) and (c) would not be present at the corresponding cavitation numbers without electrolysis. Photograph (d)

shows the natural incipient cavitation. U = 31 ft/sec., $\overline{\sigma}_i \doteq .4$, $-c_{p\,min} = .6$, $-c_{p_s} = .46$.

Fig. 25. Photographs illustrating the change in the physical appearance of cavitation produced due to electrolysis bubbles with increase in tunnel velocity on the Swedish headform. For comparison physical appearance of cavitation under natural conditions is shown in the photograph (d).

Fig. 26. Sequential photographs showing two different types of upstream motion of the microscopic bubbles within the separated layer on the hemispherical nose. The free stream flow is from left to right. The dark patches at the downstream end of the photographs is the macroscopic cavitation readily observable to the naked eye. U = 40 ft/sec., $\sigma = .74$.

Fig. 27. Sequential photographs illustrating the nature of desinent cavitation on the Swedish headform. Last traces of cavitation are seen to exist at the end of the separated layer. U = 40 ft/sec., $\sigma \doteq .46$. The top schlieren photograph is at U = 30 ft/sec. The free stream flow is from left to right.

Fig. 28. Variation of the length of the laminar separated bubble for the two test models in non-dimensional form with Reynolds number. Also shown is similar data obtained by Gaster[40] in wind tunnel studies.

Fig. 29. Variation of non-dimensional maximum height of the laminar separated bubble indicated by the schlieren photographs for both the test models with Reynolds number.

Fig. 30. Variation of cavitation inception coefficient introduced in present work with Reynolds number for different models.

Fig. 31. Comparison of incipient cavitation index for 1.5 calibre ogive with the negative value of the pressure coefficeint at the predicted point of transition for $Re_D > Re_{D\,crit}$.

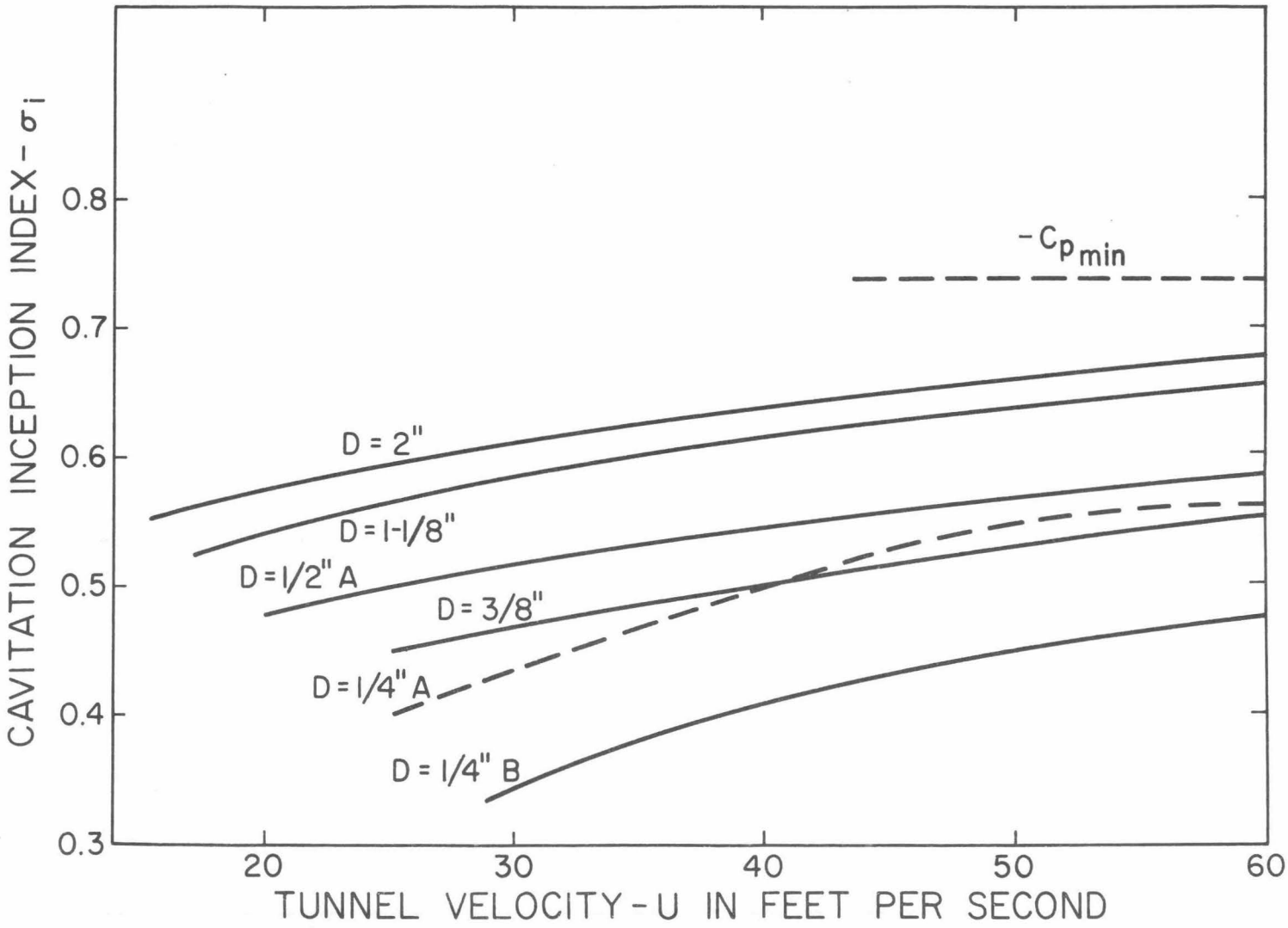

Fig.1. Cavitation inception number versus velocity at maximum acoustic pressure for a series of 6 hemispheres with cylindrical afterbody of diameter-D (Ref.4.).

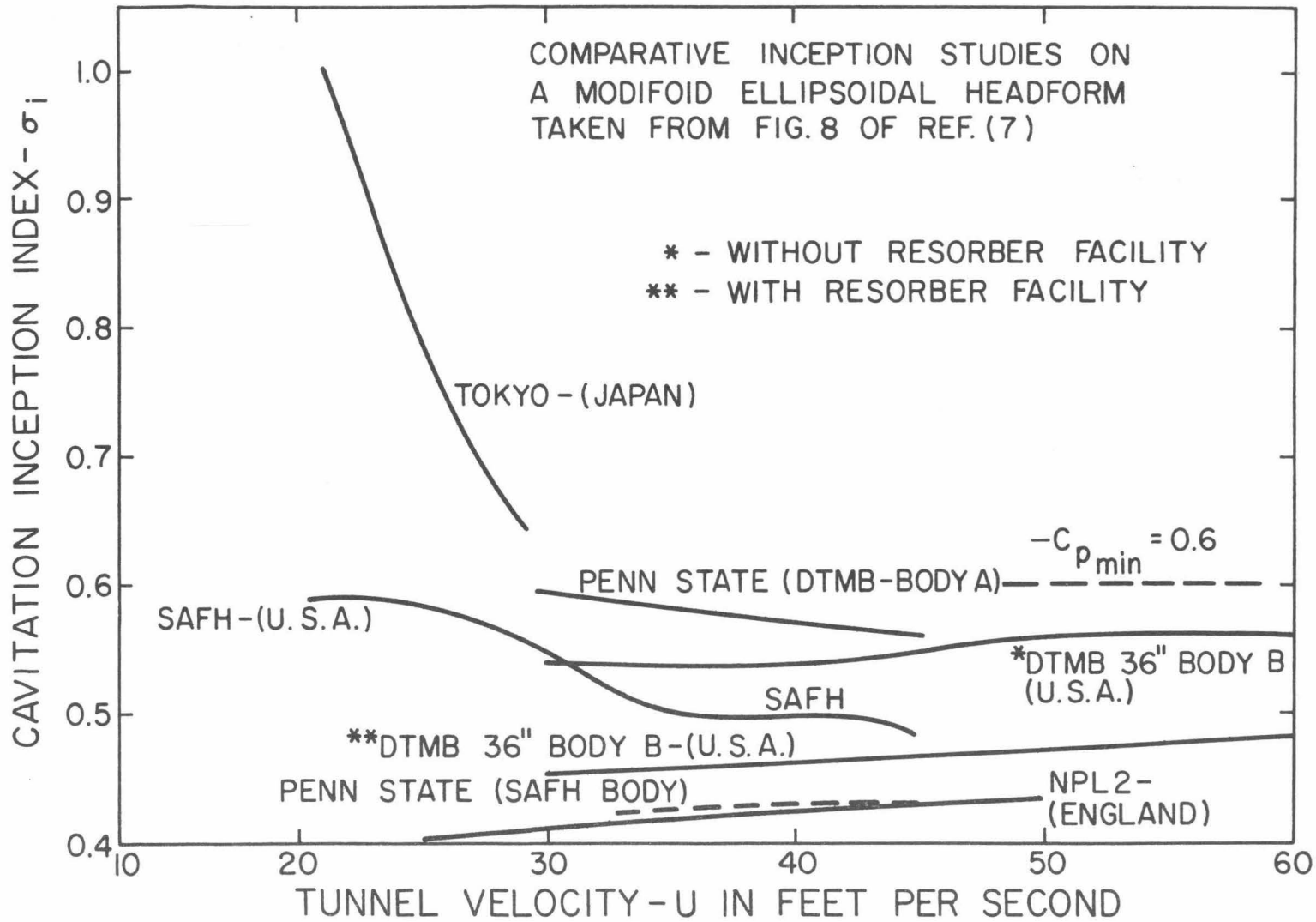

Fig. 2. Results of a comparative cavitation inception test on a modified ellipsoidal headform sponsored by the International Towing Tank Conference. Taken from Fig. 8 of Ref. (7).

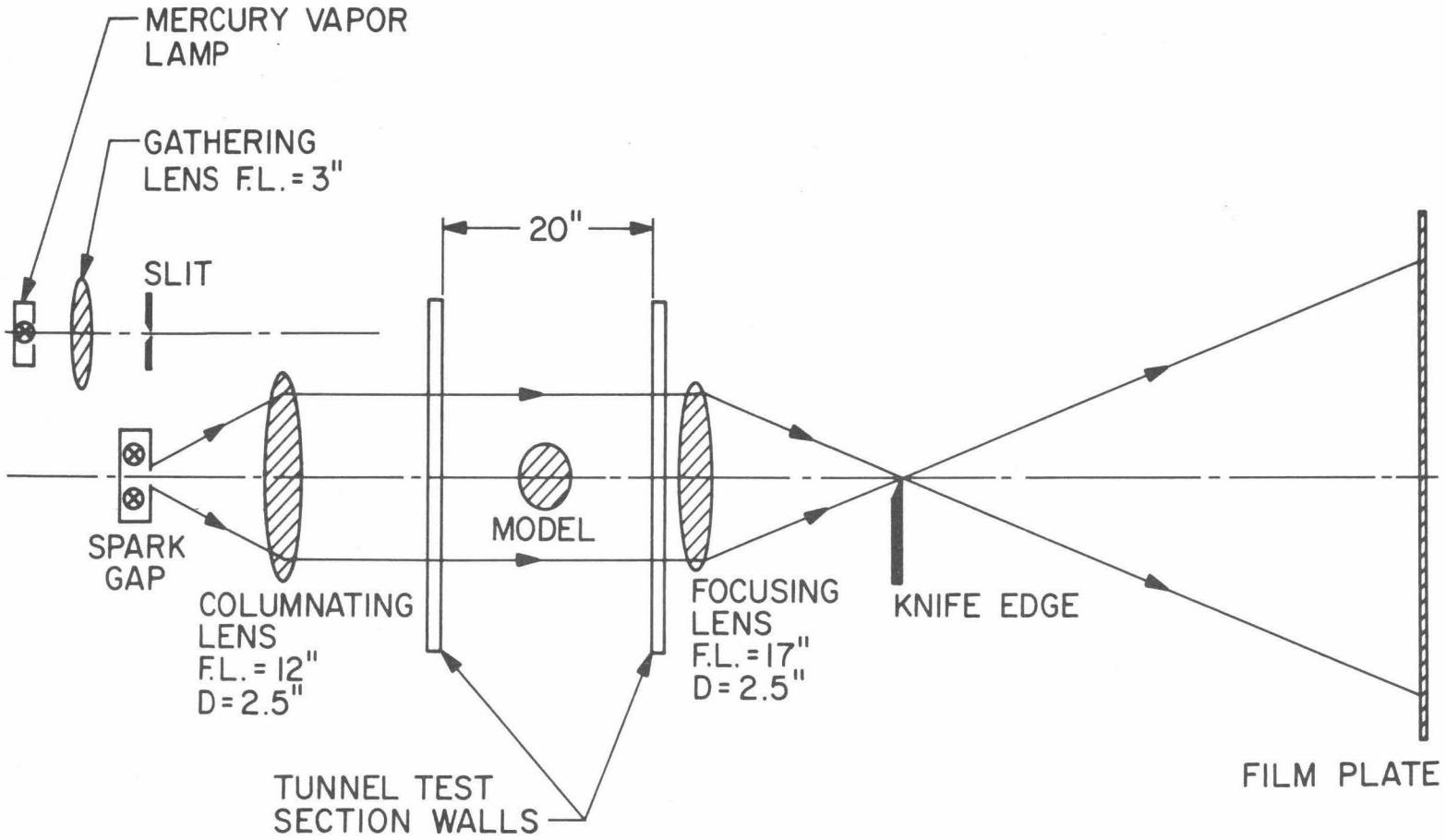

Fig. 3. Schematic drawing showing the schlieren set-up in the Free Surface Water Tunnel.

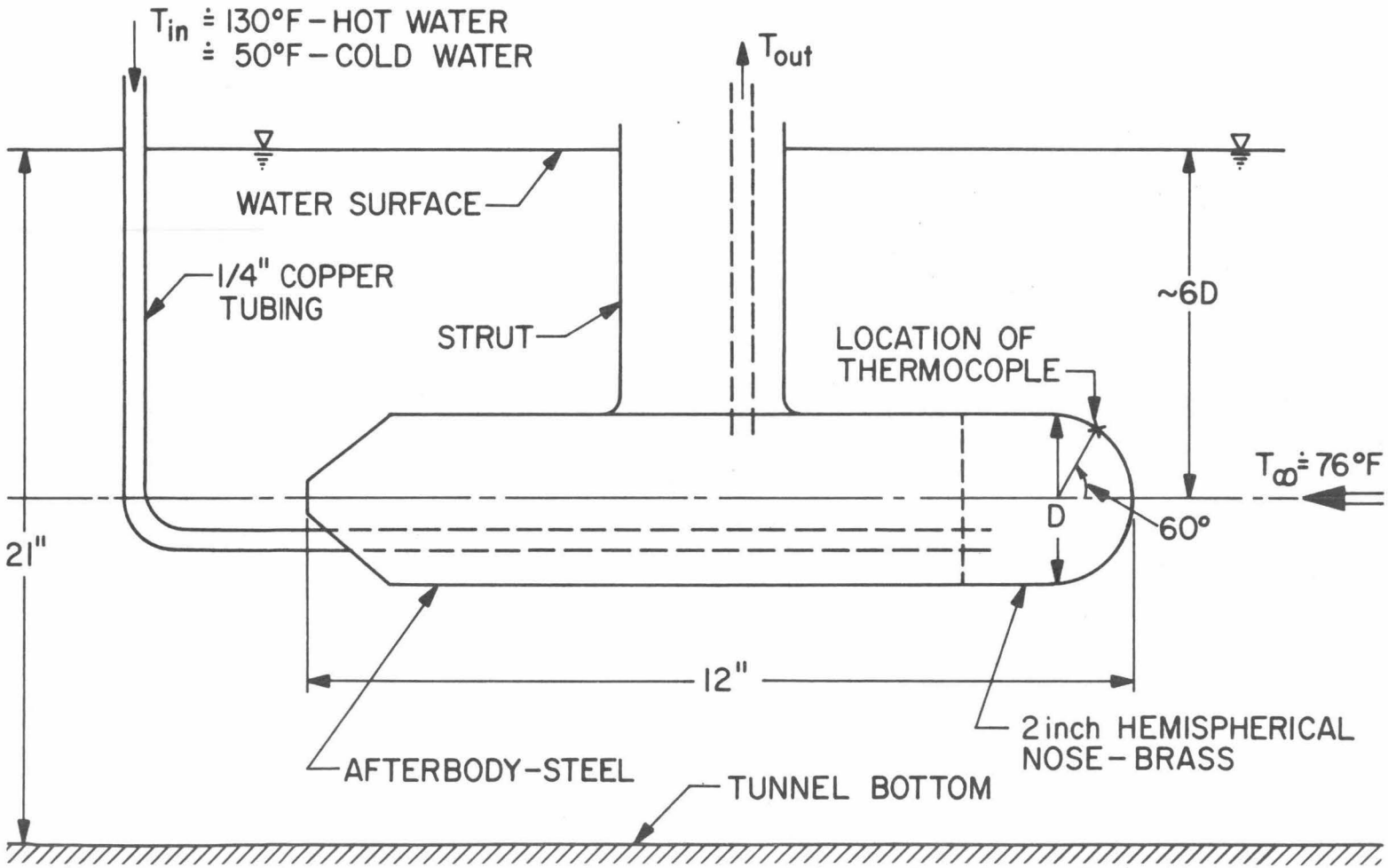

Fig. 4. Schematic diagram showing the mounting of a two inch hemispherical nose in the Free Surface Water Tunnel. Additionally the different places of temperature measurements to obtain heat transfer data are shown.

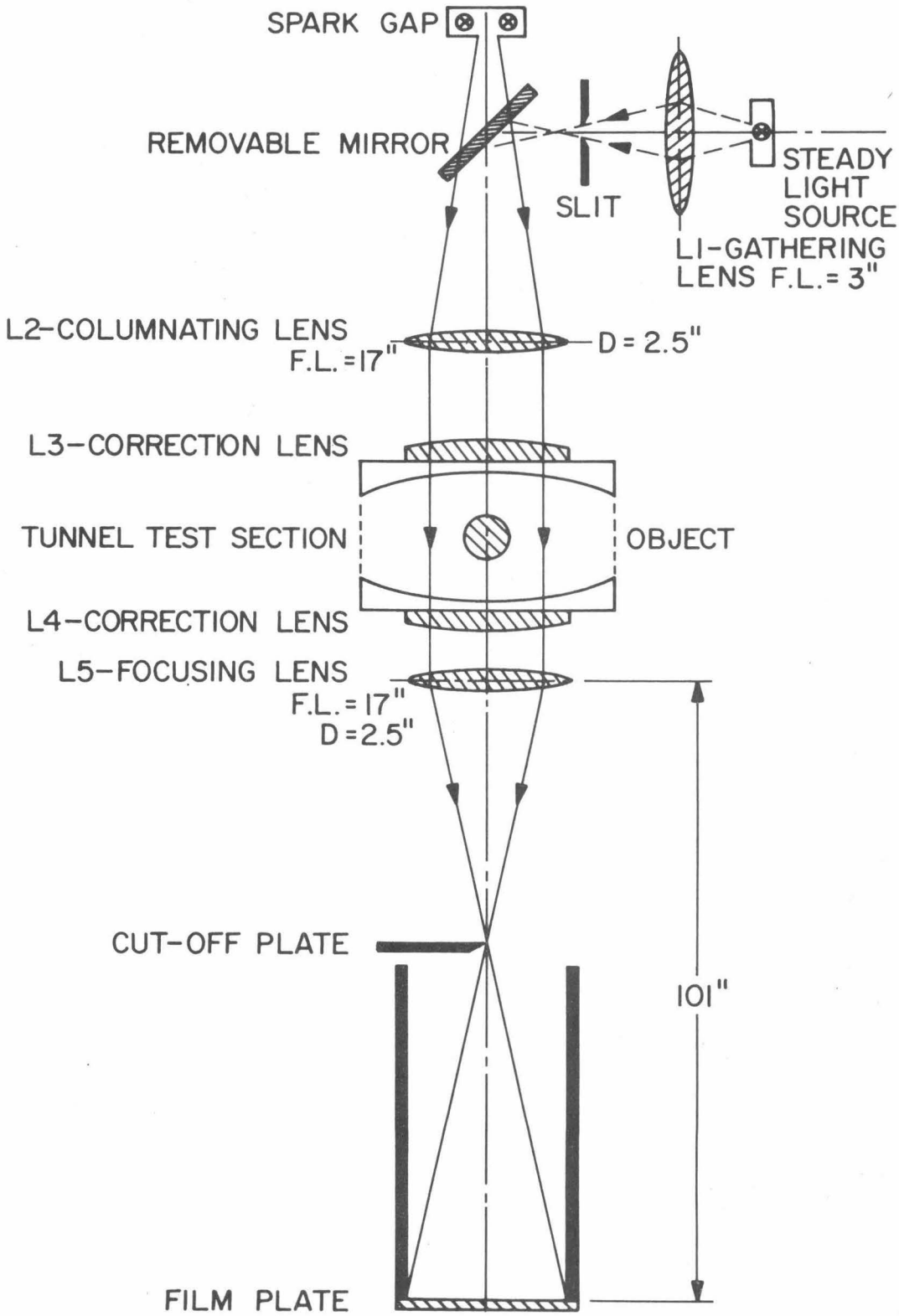

Fig. 5. Schematic diagram of theschlieren set-up in the High Speed Water Tunnel.

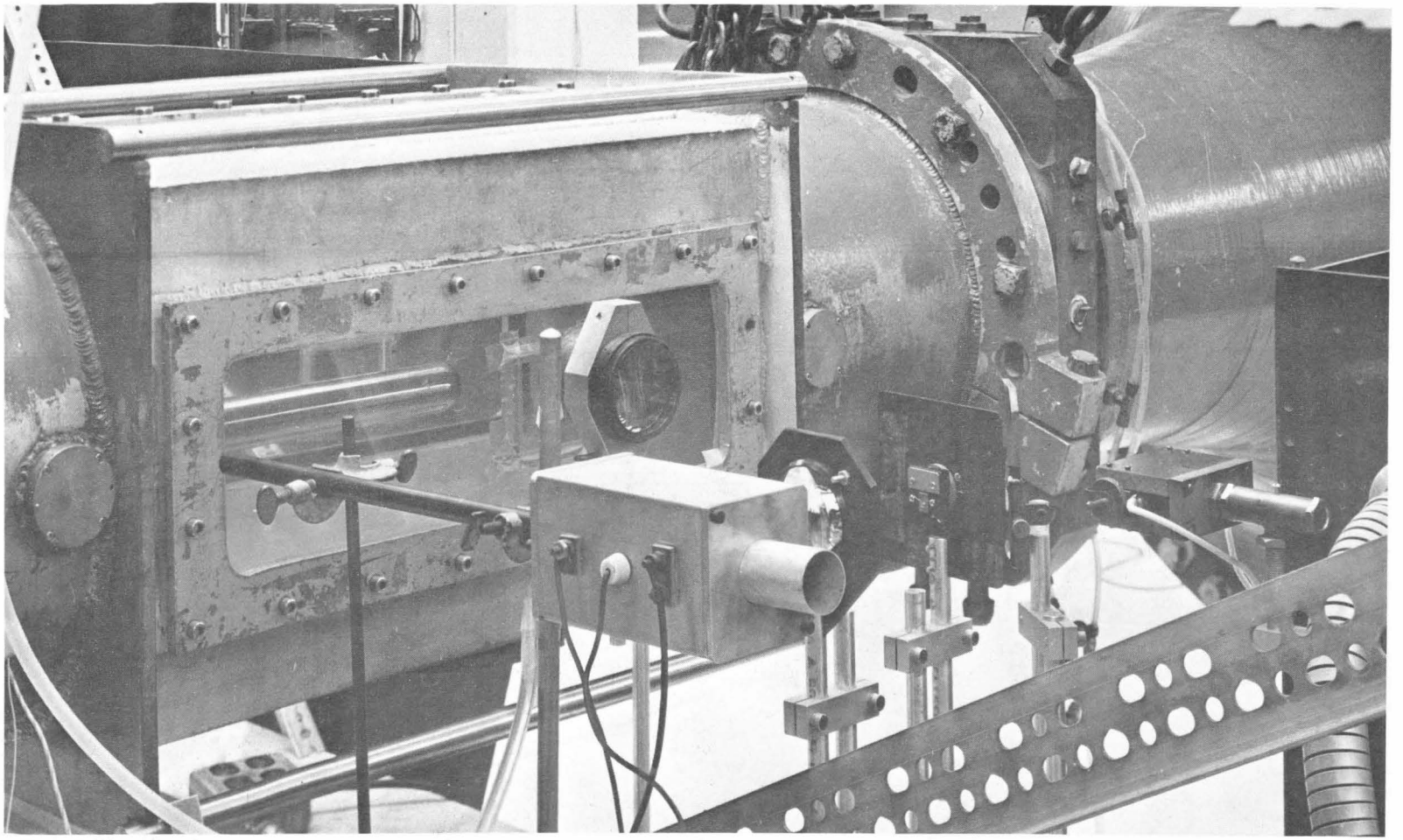

Fig. 6. Illustration of light source side of the schlieren system. On the far right is the spark gap source, followed by deflecting mirror and columnating lens. The white box on the far left is the steady light source. A plano convex correction lens is shown taped on the tunnel window.

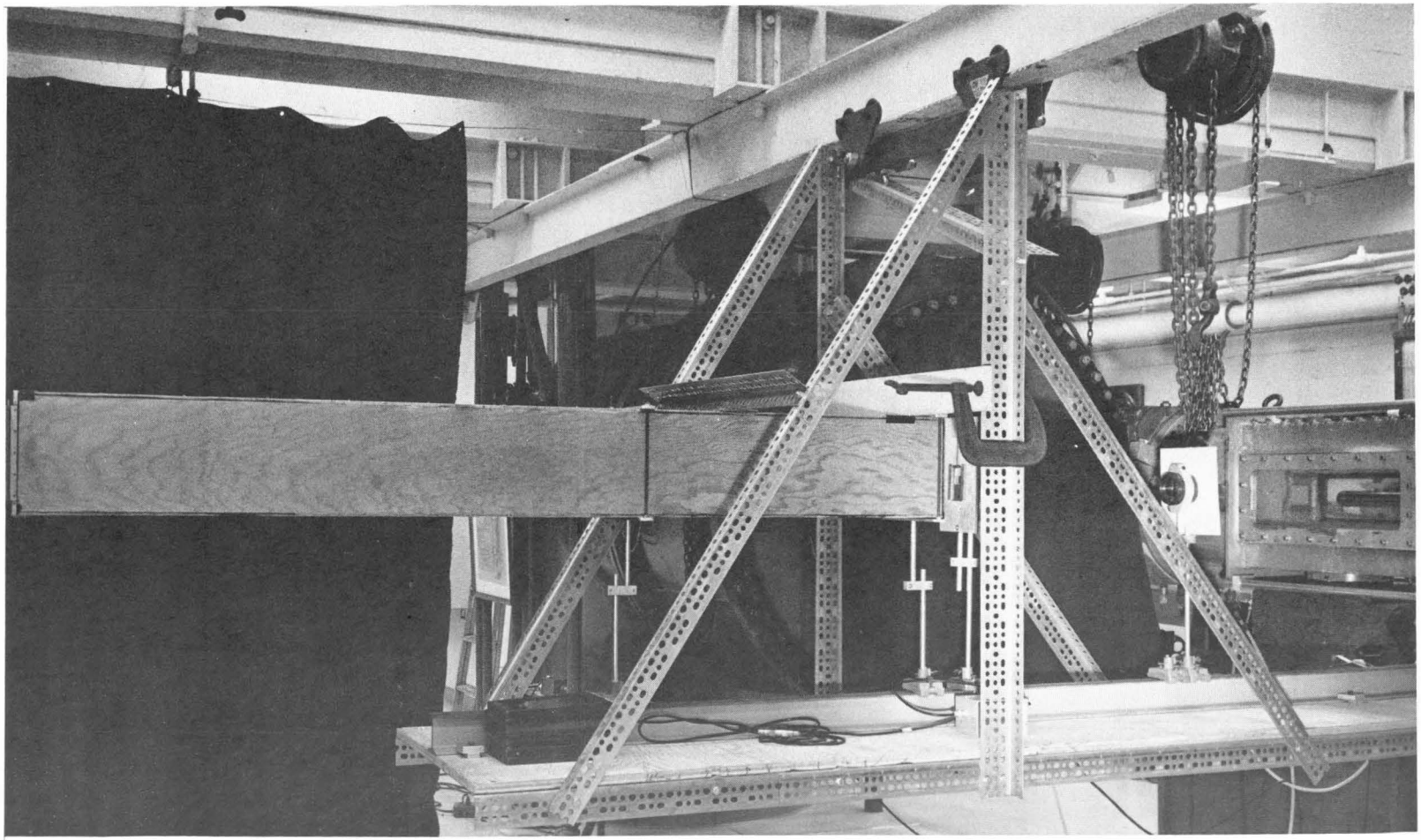

Fig. 7. Illustration of camera side of the schlieren system. In this figure, the first lens is the focusing lens, followed by the cut off knife edge placed just before the camera box itself. The camera box is 80 in. long.

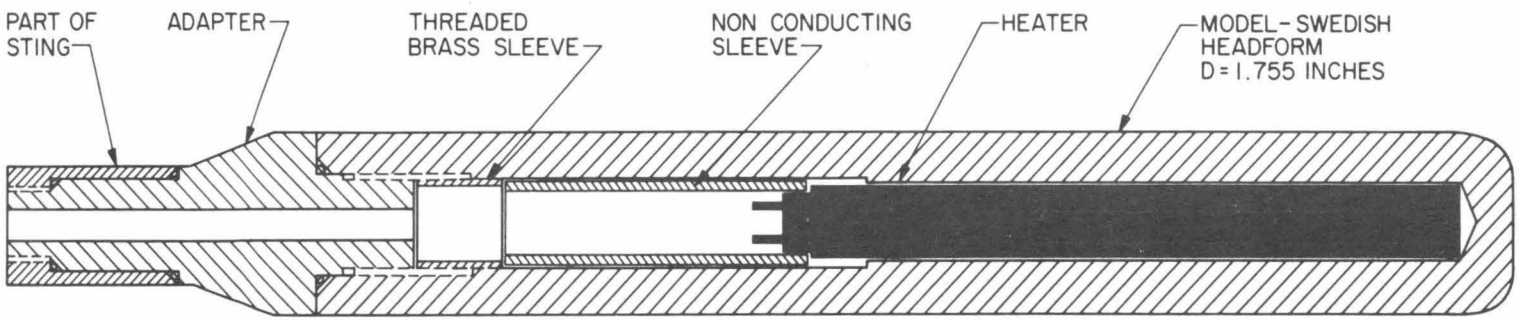

Fig. 8. A drawing showing the details of placing the electric heater inside the Swedish headform. The dark shaded area is the heater.

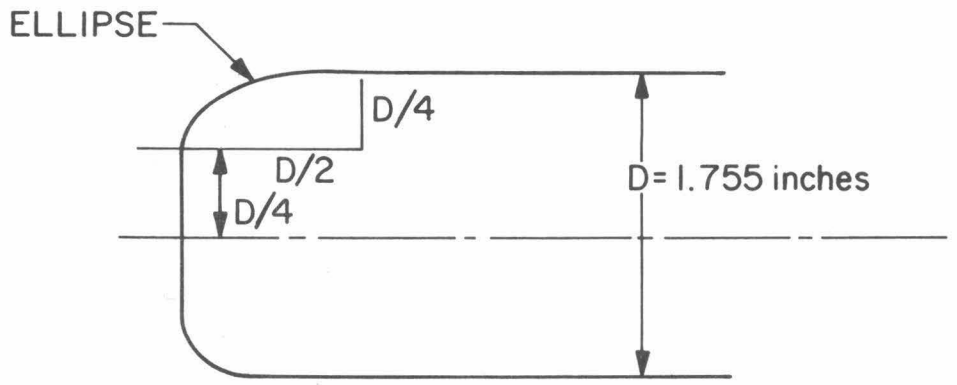

MATERIAL - STAINLESS STEEL
SURFACE FINISH - SMOOTH
AXISYMMETRIC

Fig. 9. Diagram showing the geometrical details of the Swedish headform.

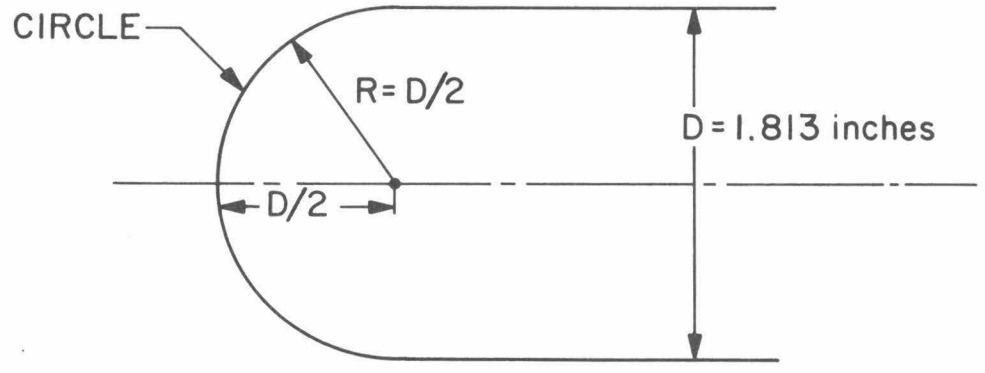

MATERIAL- BRASS
SURFACE FINISH- SMOOTH
AXISYMMETRIC

Fig. 10. Diagram showing the geometrical details of the hemispherical nose.

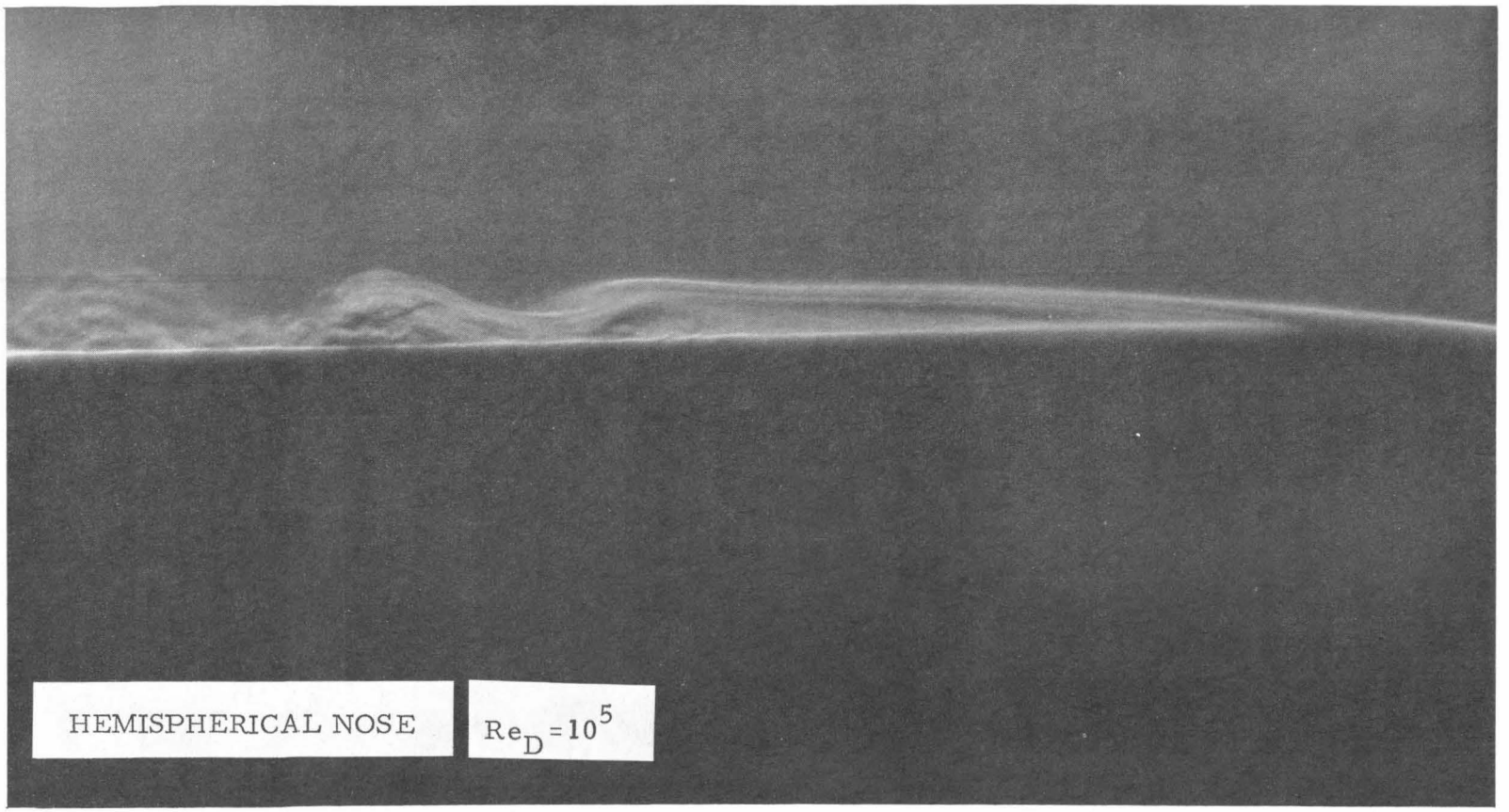

Fig. 11. A schlieren photograph showing the laminar separation bubble on a two inch hemispherical nose at a Reynolds number of 10^5. The flow is from right to left. Also noticed is the gradual break up of the separated free shear layer and its subsequent reattachment to the model surface.

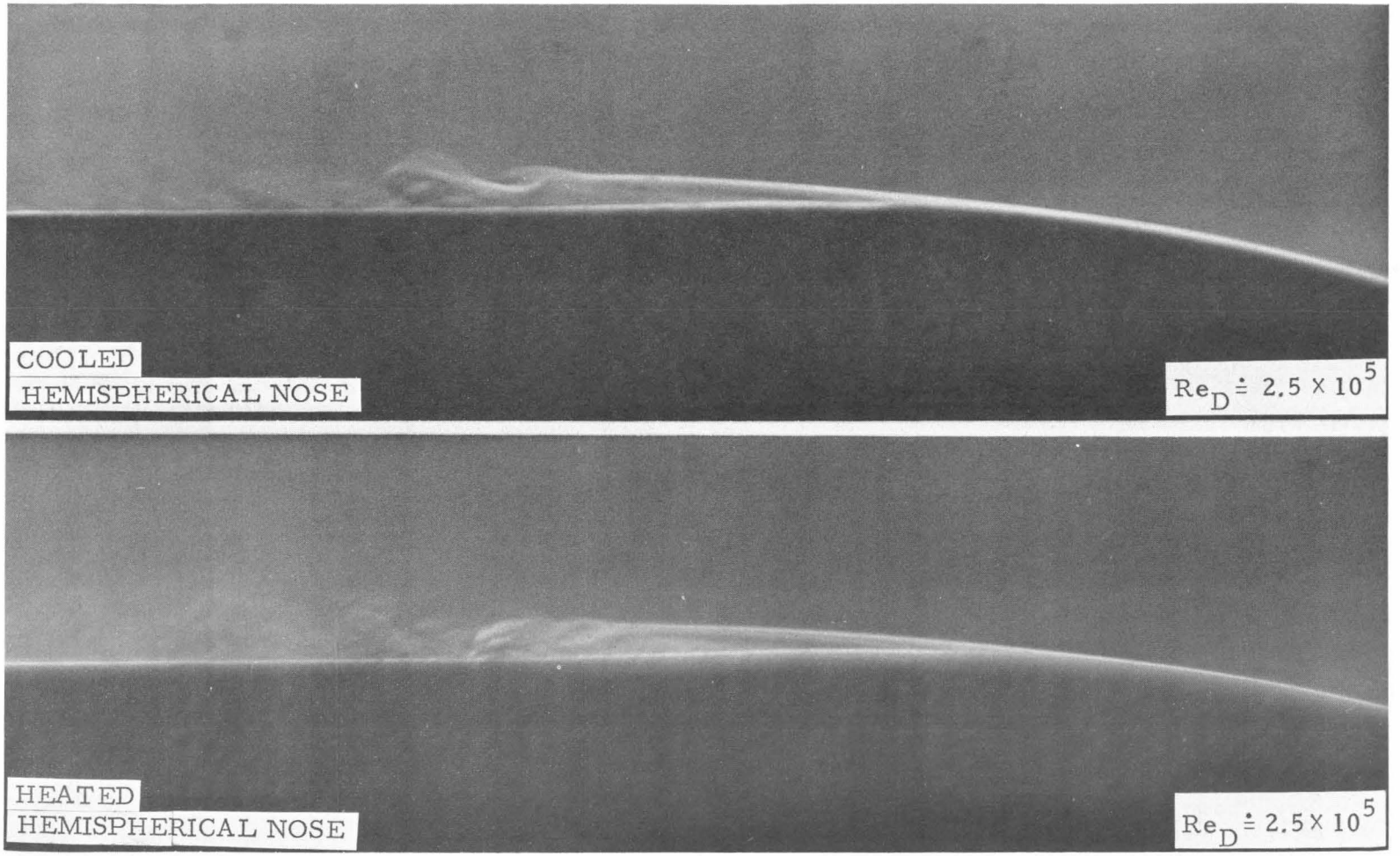

Fig. 12 Photograph illustrating, that the position or extent of laminar separation is not influenced by the change of model surface temperature. Top photograph is with surface temperature about 10°F below the free stream water temperature and the bottom is with surface temperature about 10°F above. Both photographs are of a two in. hemispherical nose at $Re_D \doteq 2.5 \times 10^5$.

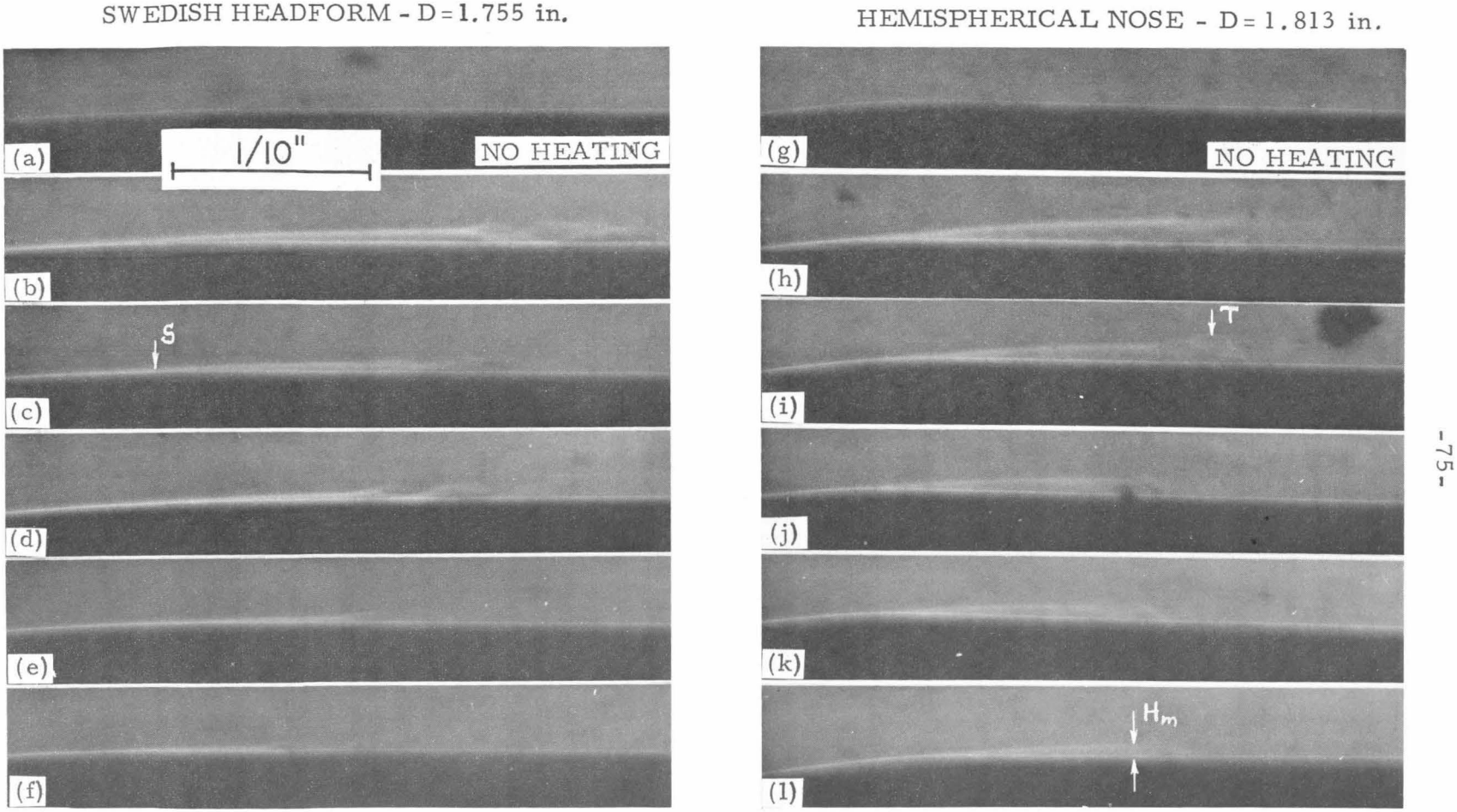

Fig. 13. Schlieren photographs illustrating the change in extent of laminar separation bubble with increase in tunnel velocity or Reynolds number for both the test models. The top two photographs (a) and (g) are taken with no model heating at a tunnel velocity of 40 ft/sec. (a) $Re_D = 5.85 \times 10^5$, (b) $Re_D = 2.93 \times 10^5$, (c) $Re_D = 4.39 \times 10^5$, (d) $Re_D = 5.85 \times 10^5$, (e) $Re_D = 7.31 \times 10^5$, (f) $Re_D = 8.78 \times 10^5$, (g) $Re_D = 6.04 \times 10^5$, (h) $Re_D = 3.02 \times 10^5$, (i) $Re_D = 4.53 \times 10^5$, (j) $Re_D = 6.04 \times 10^5$, (k) $Re_D = 7.55 \times 10^5$, (ℓ) $Re_D = 9.06 \times 10^5$

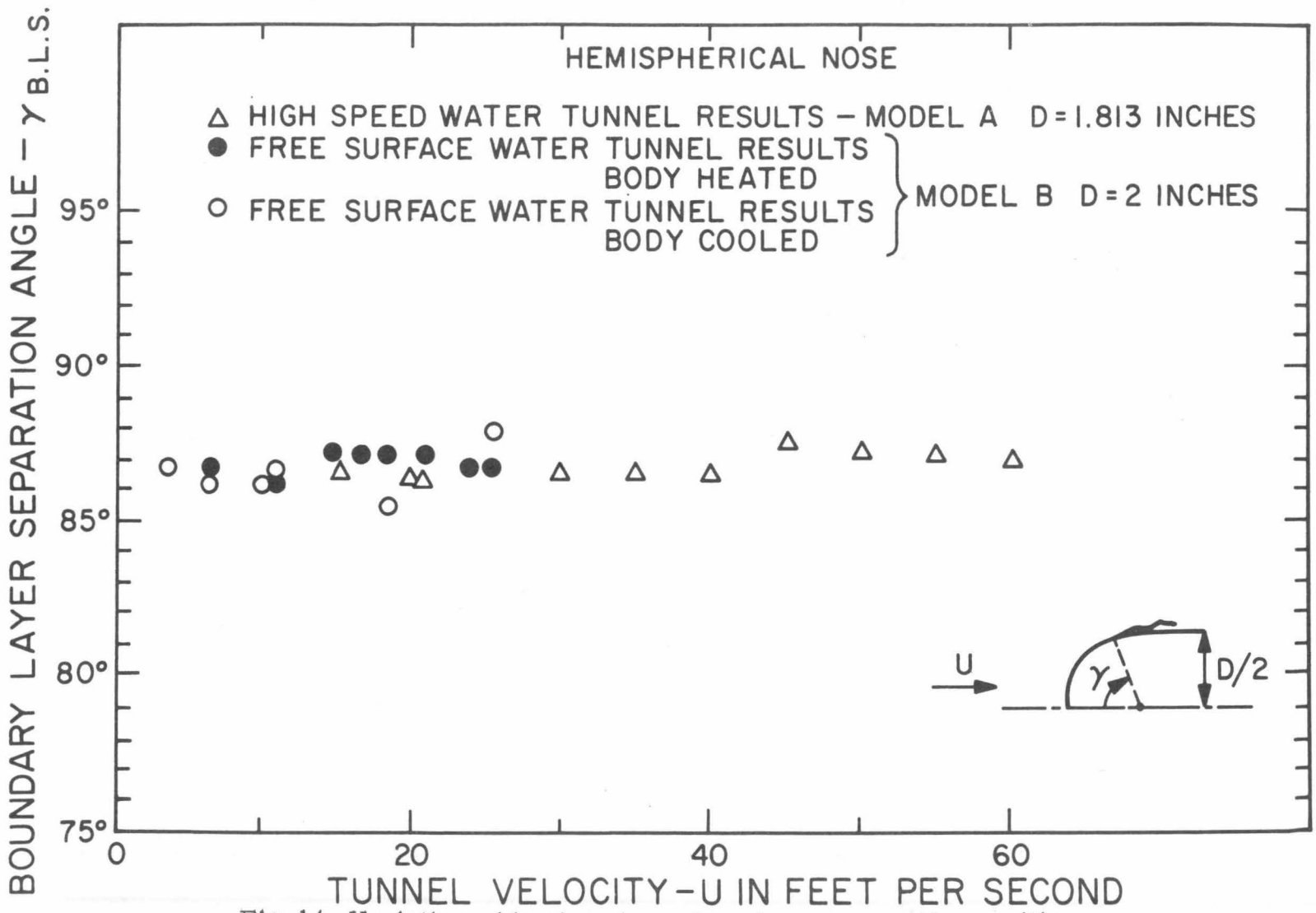

Fig. 14. Variation of laminar bou ndary layer separation position on the hemispherical nose with tunnel velocity. Also shown is the effect of temperature change on the position of separation.

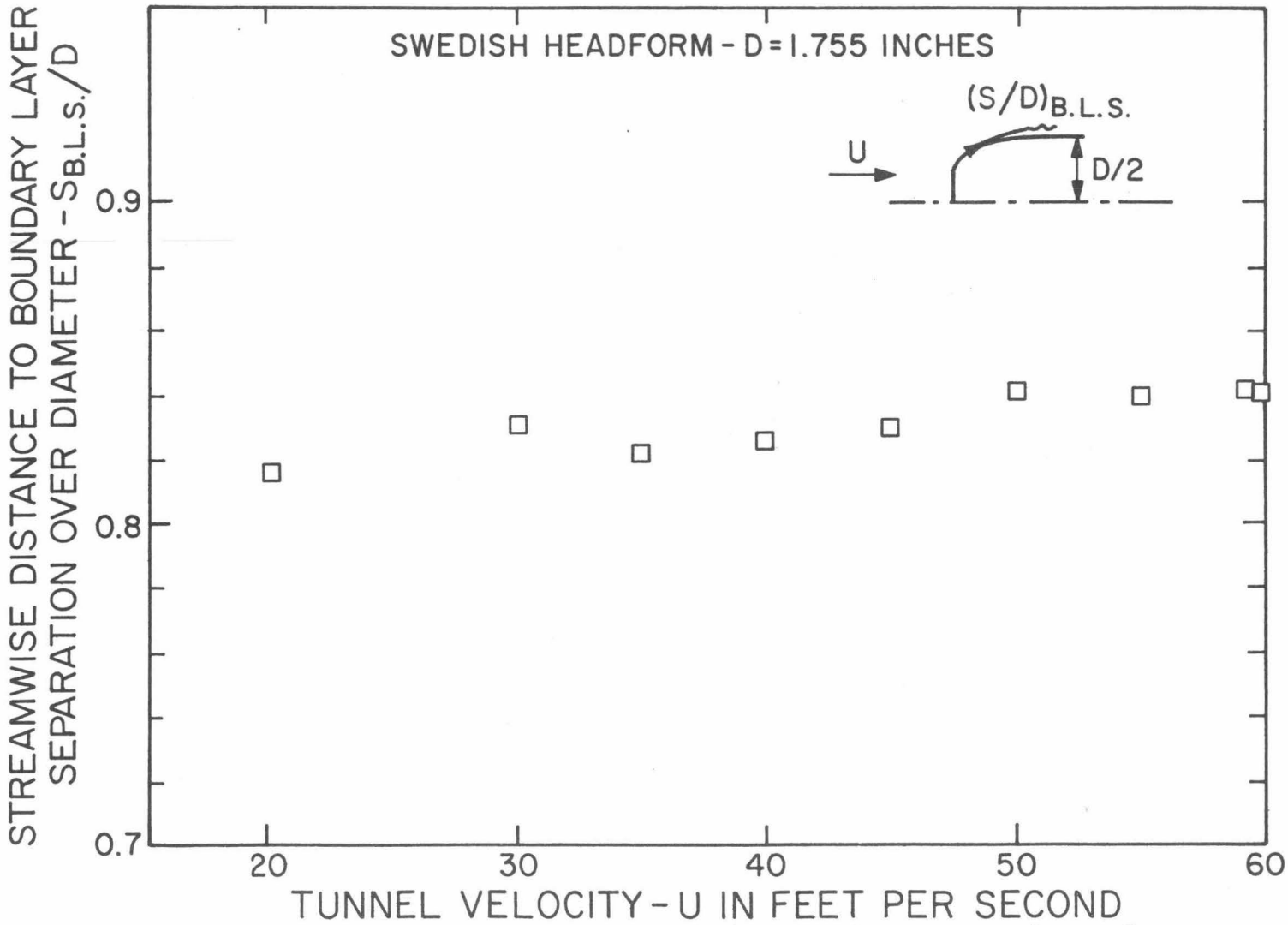

Fig.15. Variation of the position of boundary layer separation on the Swedish headform with change in tunnel velocity.

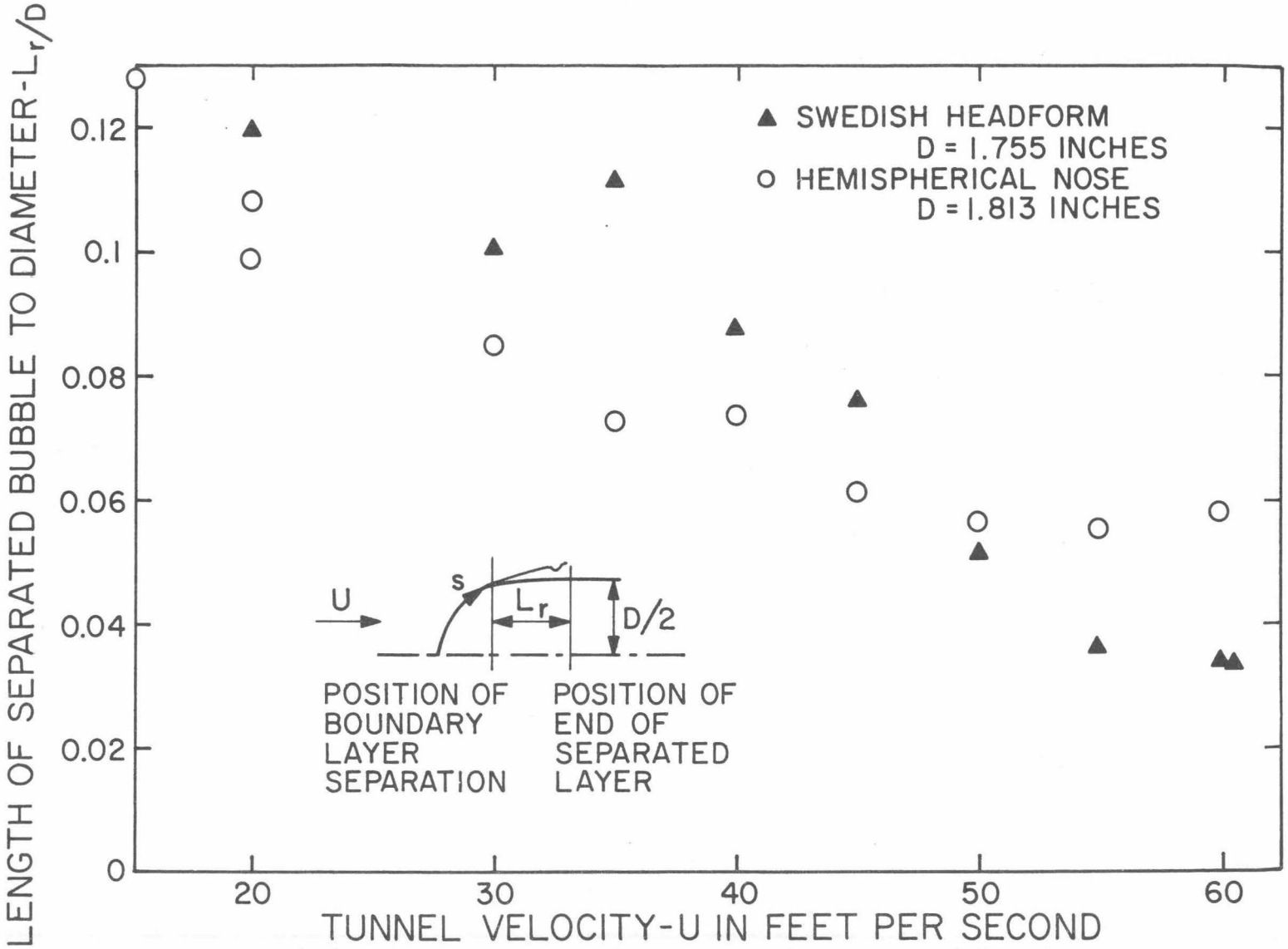

Fig. 16. Variation of the length of the laminar separated bubble estimated from schlieren photographs with tunnel velocity for both the test models.

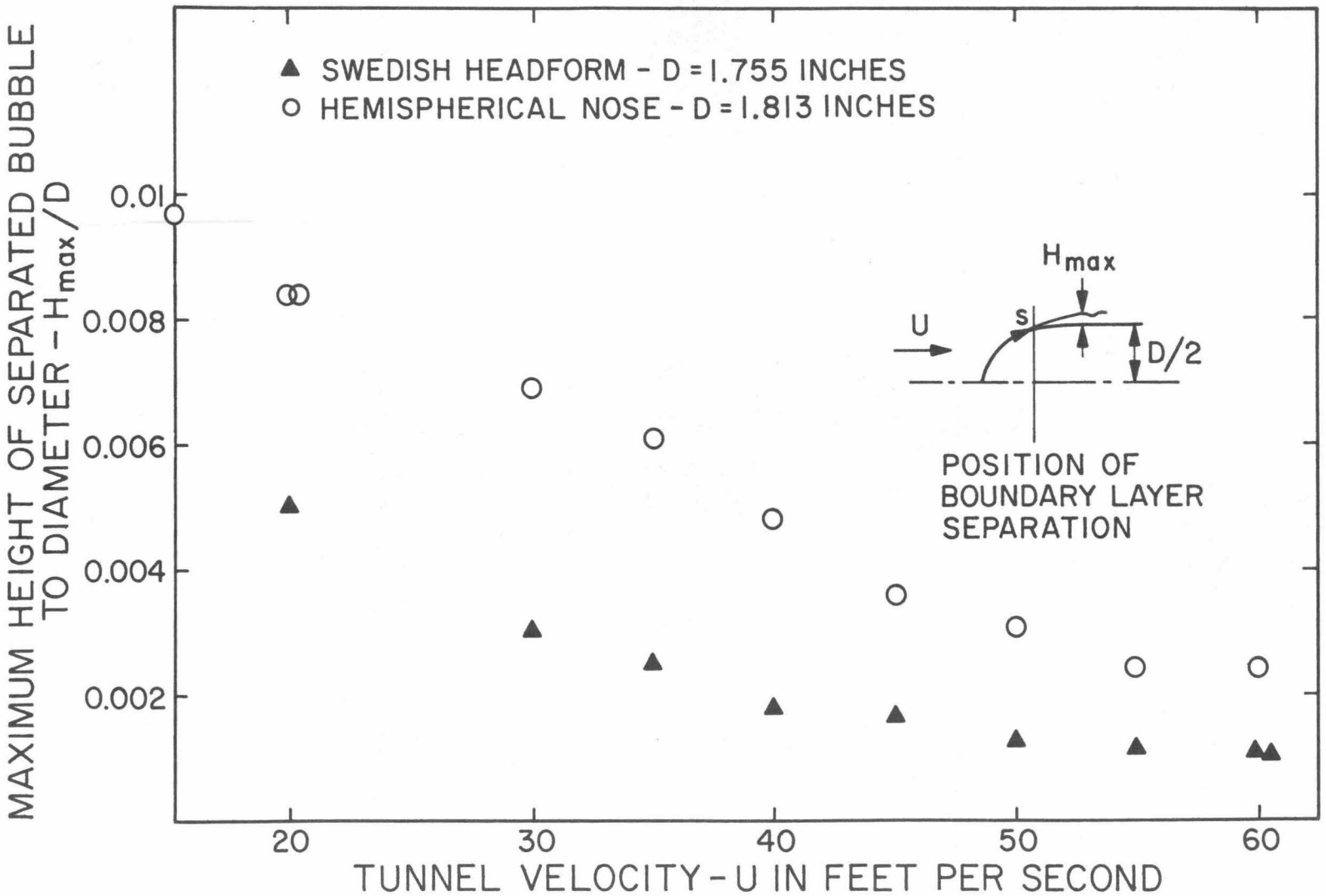

Fig. 17. Variation of the maximum height of the laminar separated bubble indicated by the schlieren photographs with velocity for both the test models.

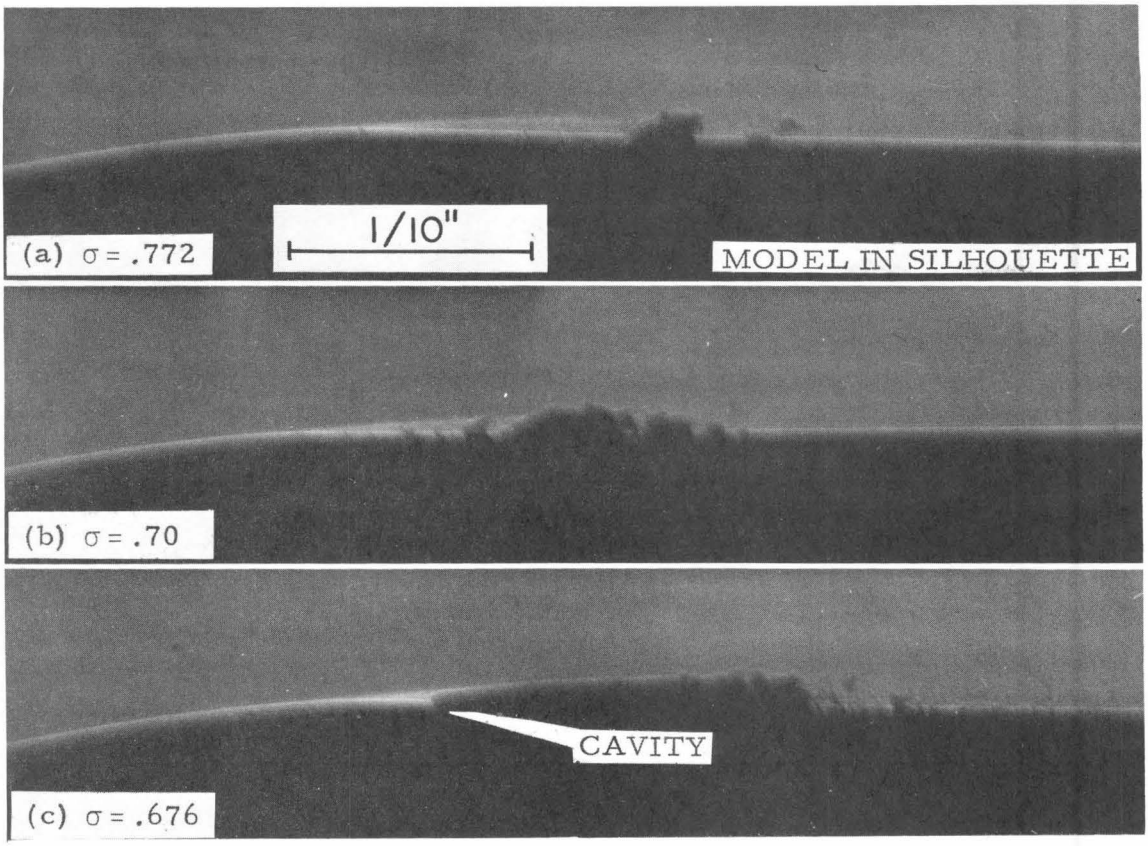

Fig. 18. Sequence showing the progressive development of cavitation on the hemispherical nose in the laminar boundary layer separated region at a tunnel velocity of 40 ft/ sec. corresponding $Re_D = 6.04 \times 10^5$. The dark patches above the model surface are cavitating areas.

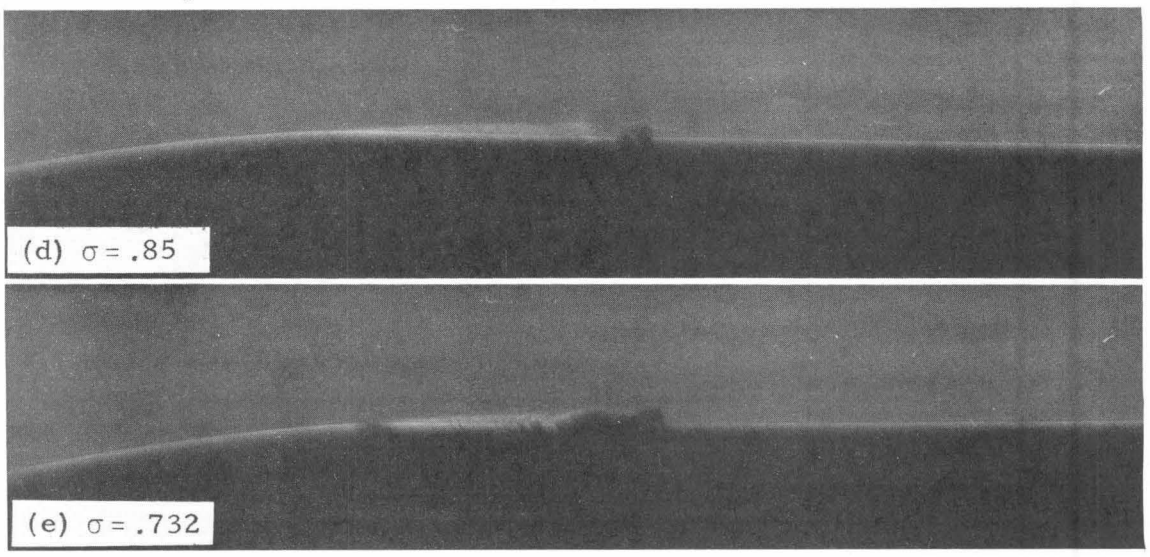

Fig. 19. Partial sequence showing the progressive development of cavitation on the hemispherical nose in the separated region at a tunnel velocity of 60 ft/sec. corresponding $Re_D = 9.06 \times 10^5$.

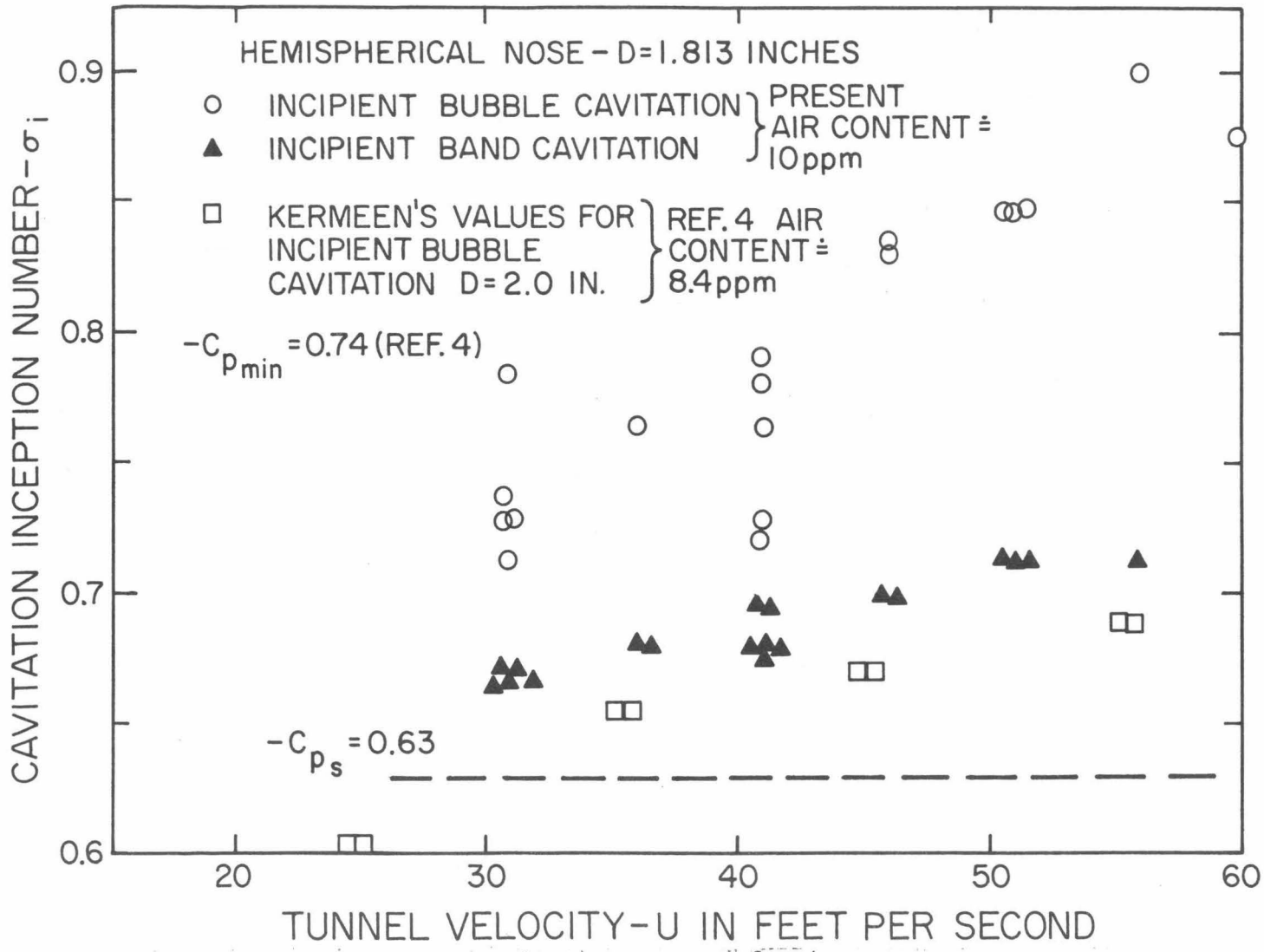

Fig. 20. Variation of cavitation inception number with tunnel velocity on the hemispherical nose for two types of incipient conditions. Also included are Kermeen's data.

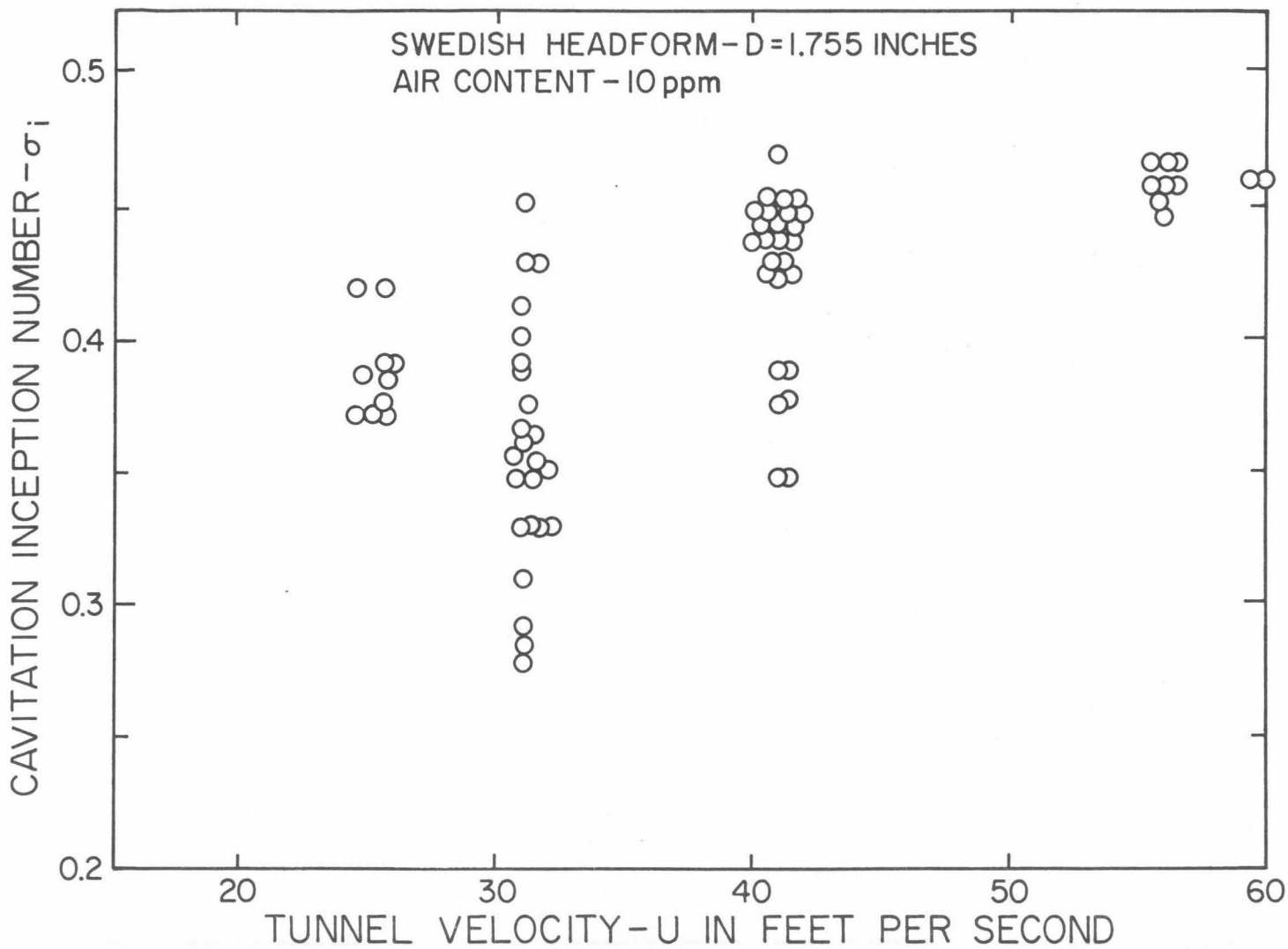

Fig. 21. Variation of cavitation inception number for the Swedish headform with tunnel velocity. Inception was always of the "band" type

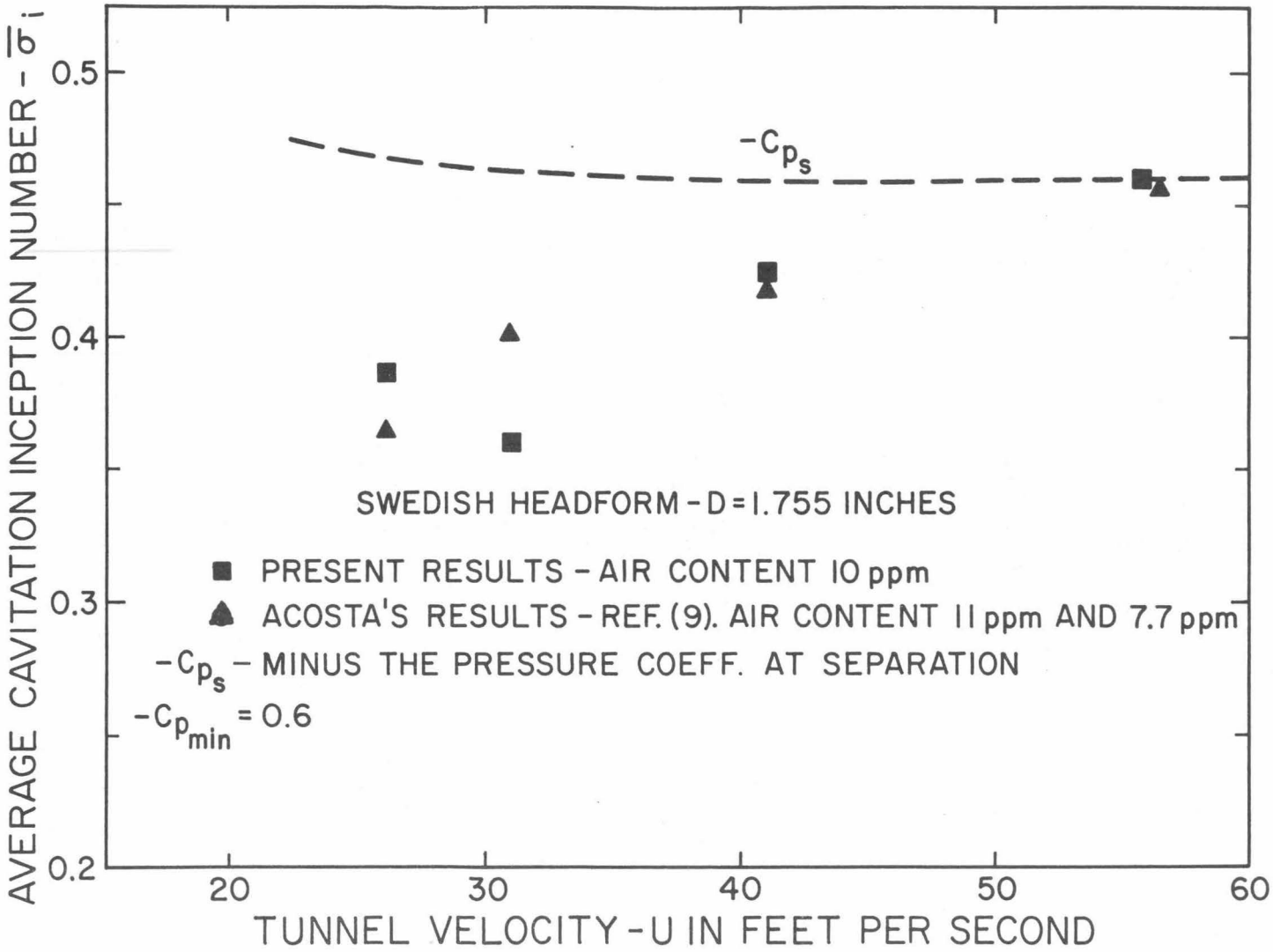

Fig. 22. Comparison of present average cavitation inception data with that obtained by Acosta[9] on the same Swedish headform and also with the negative value of the pressure coefficient at laminar separation.

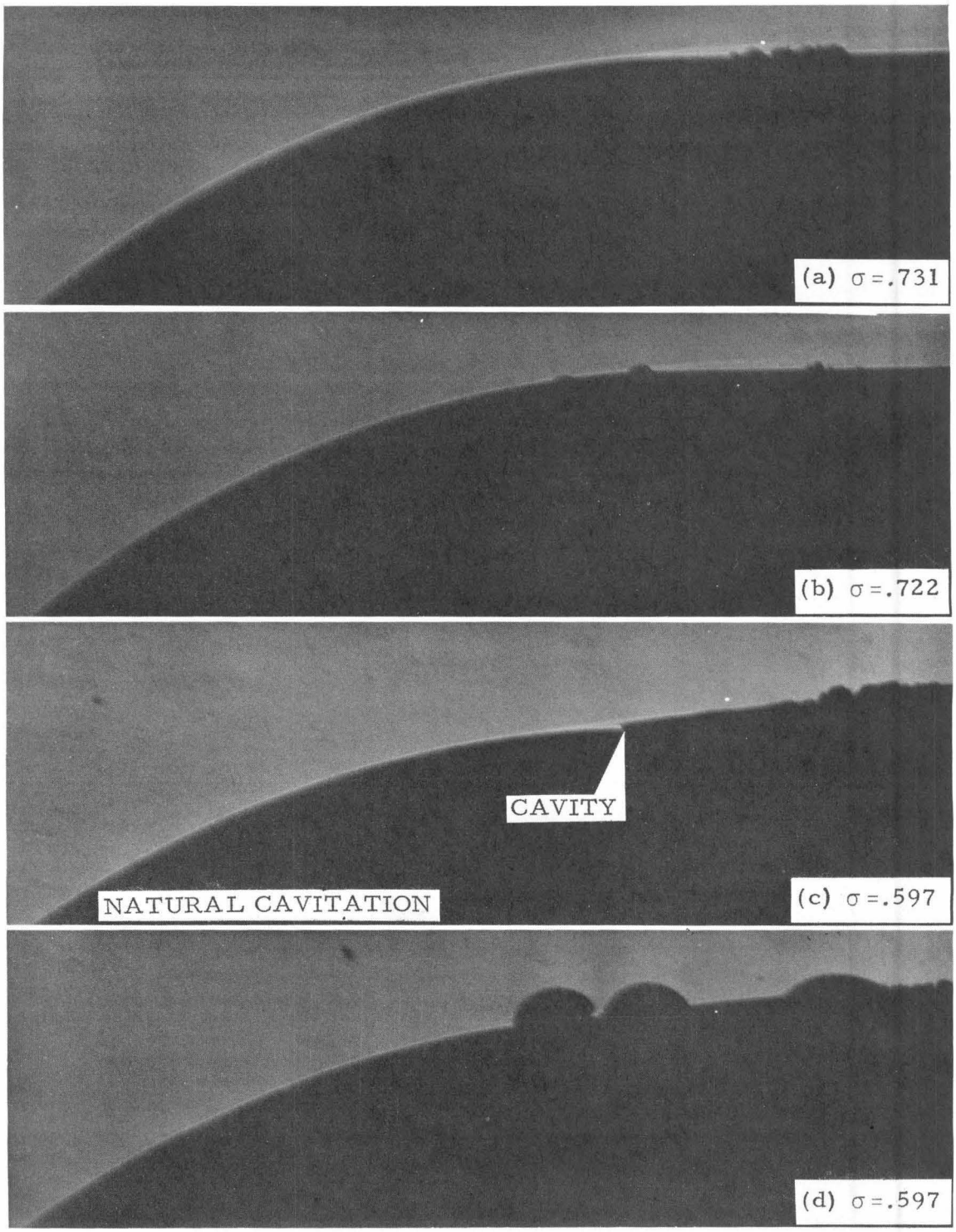

Fig. 23. Sequential photographs illustrating the effect of introducing artificial surface nuclei by electrolysis on the hemispherical nose at different tunnel pressures. The photograph (c) is under natural cavitating conditions. U = 28 ft/sec., $\sigma_i \doteq .72$, $-c_{p\,min} \doteq .74$, $-c_{p_s} \doteq .63$

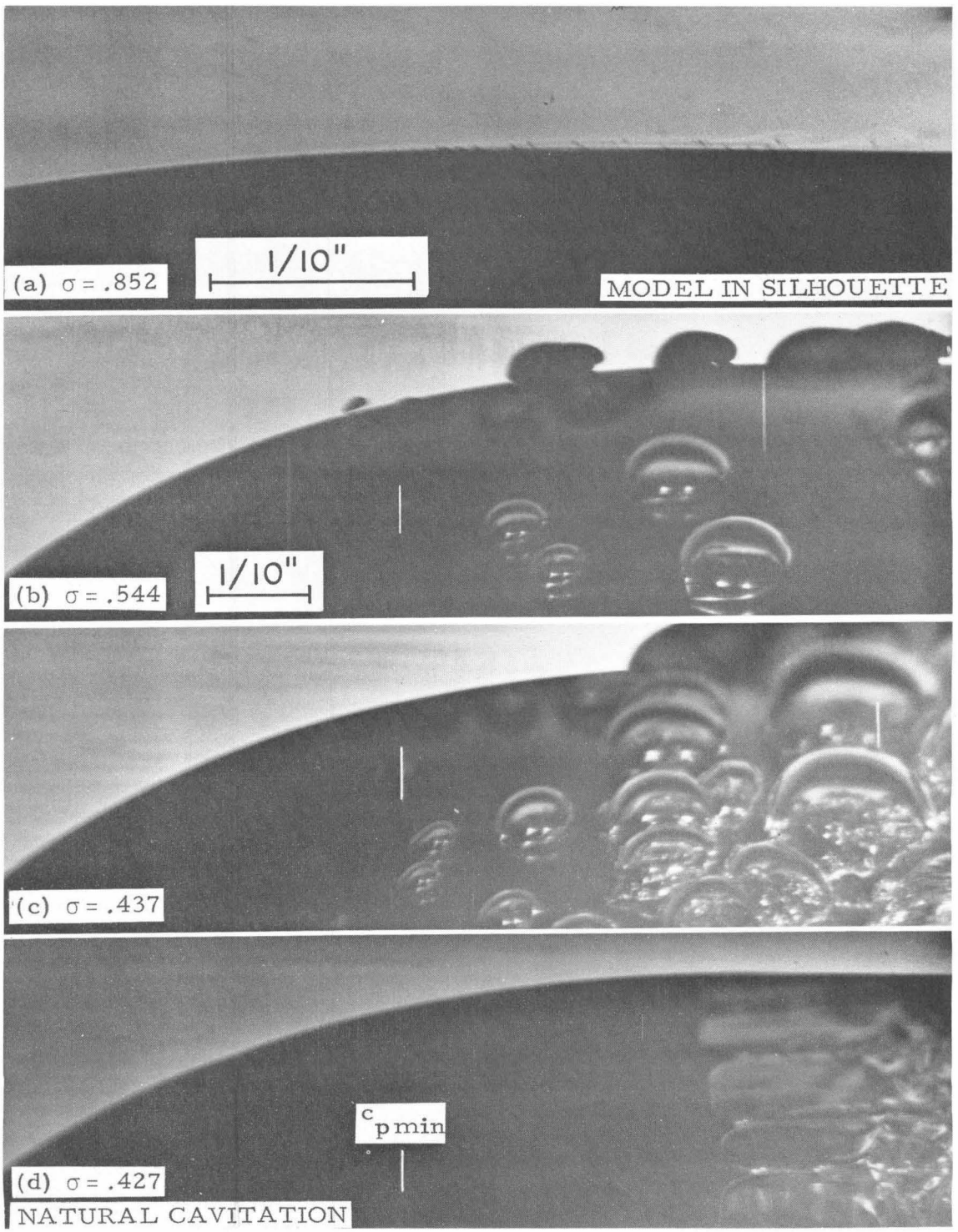

Fig. 24. Photographs illustrating the effect of introducing artificial surface nuclei by electrolysis on the Swedish headform at different tunnel pressures. Cavitation observed in photographs (b) and (c) would not be present at the corresponding cavitation numbers without electrolysis. Photograph (d) shows the natural incipient cavitation. U = 31 ft/sec., $\overline{\sigma_i} \doteq .4$, $-c_{p\,min} = .6$, $-c_{p_s} = .46$.

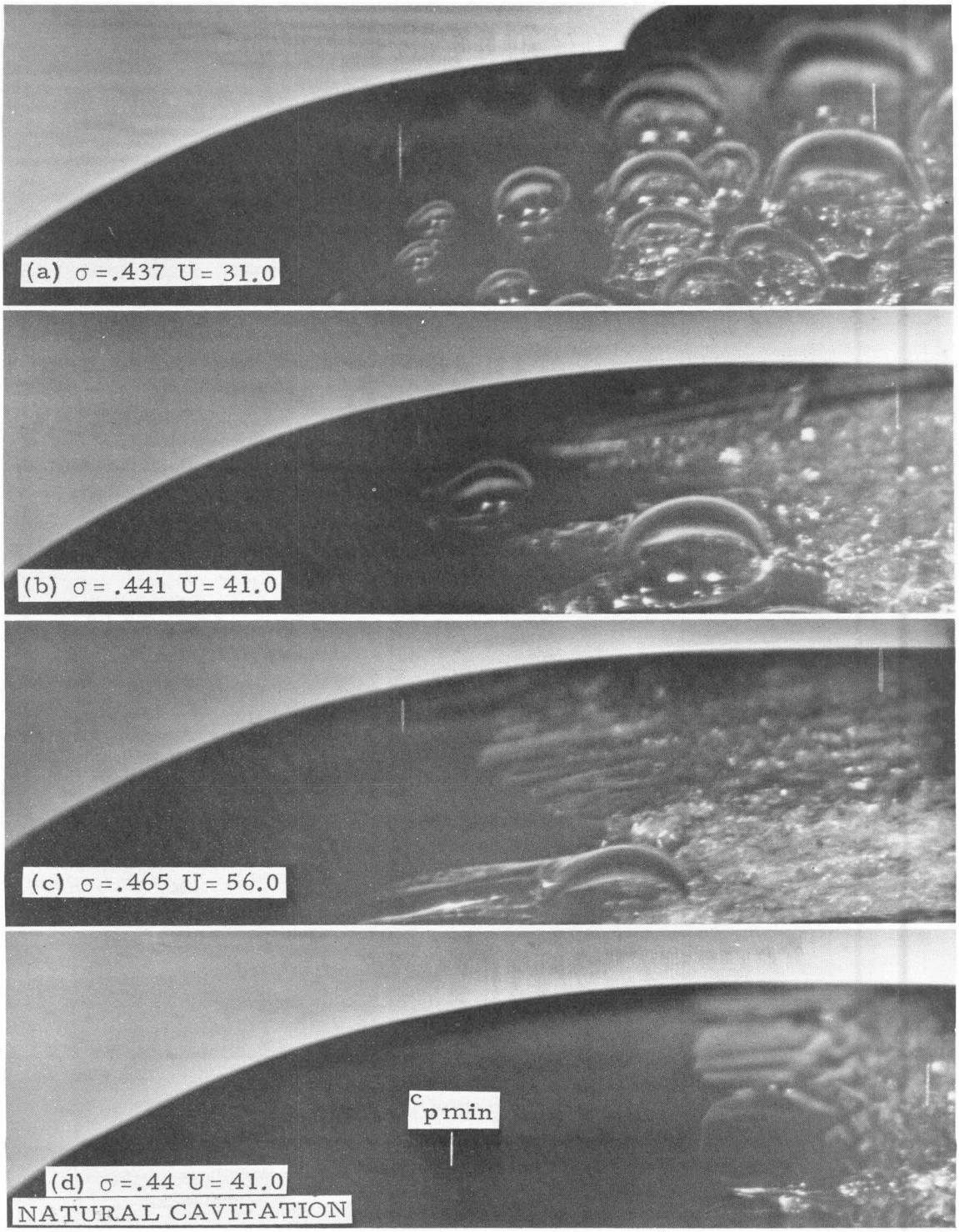

Fig. 25. Photographs illustrating the change in the physical appearance of cavitation produced due to electrolysis bubbles with increase in tunnel velocity on the Swedish headform. For comparison physical appearance of cavitation under natural conditions is shown in the photograph (d).

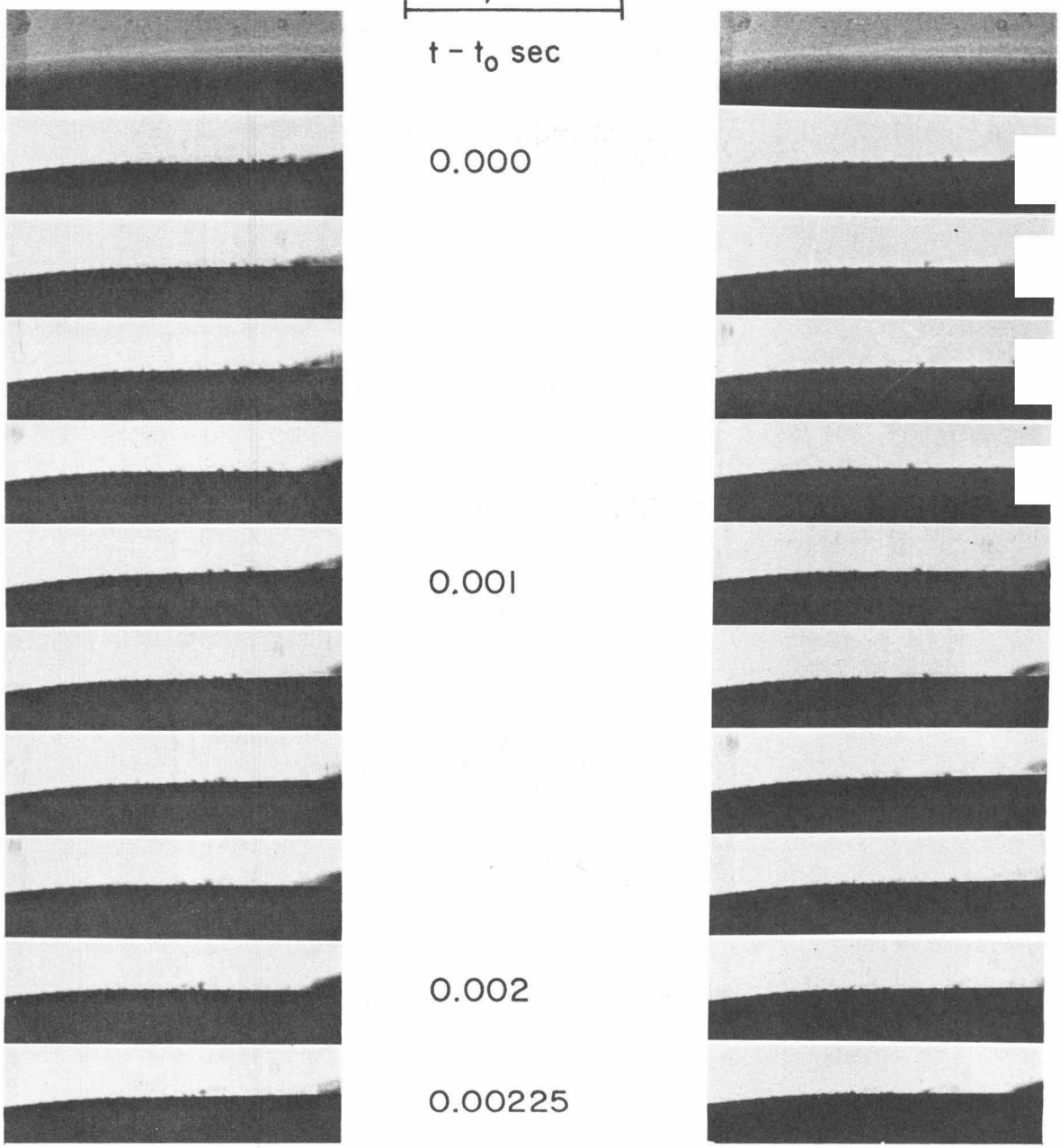

Fig. 26a

Fig. 26b

Fig. 26. Sequential photographs showing two different types of upstream motion of the microscopic bubbles within the separated layer on the hemispherical nose. The free stream flow is from left to right. The dark patches at the downstream end of the photographs is the macroscopic cavitation readily observable to the naked eye. U = 40 ft/sec., σ = .74.

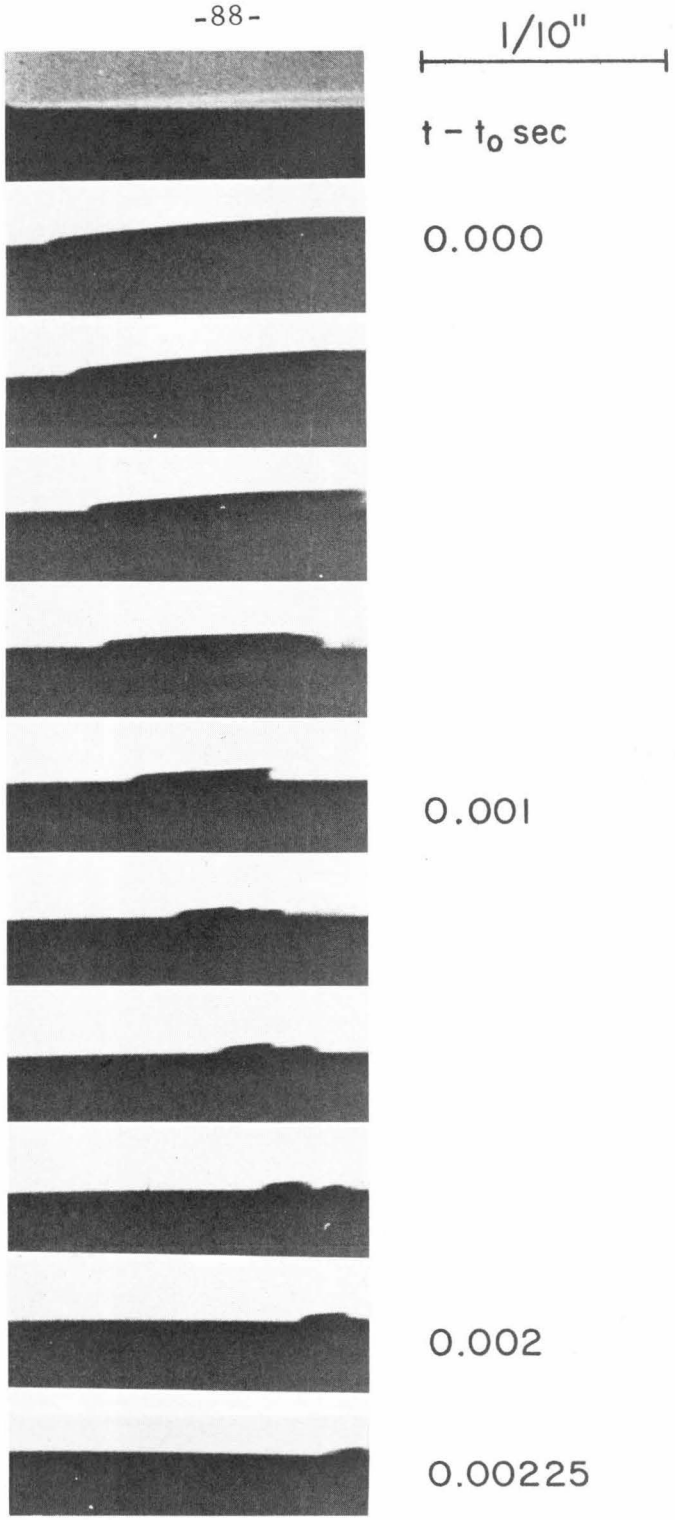

Fig. 27. Sequential photographs illustrating the nature of desinent cavitation on the Swedish headform. Last traces of cavitation are seen to exist at the end of the separated layer. U = 40 ft/sec., σ = .46. The top schlieren photograph is at U = 30 ft/sec. The free stream flow is from left to right.

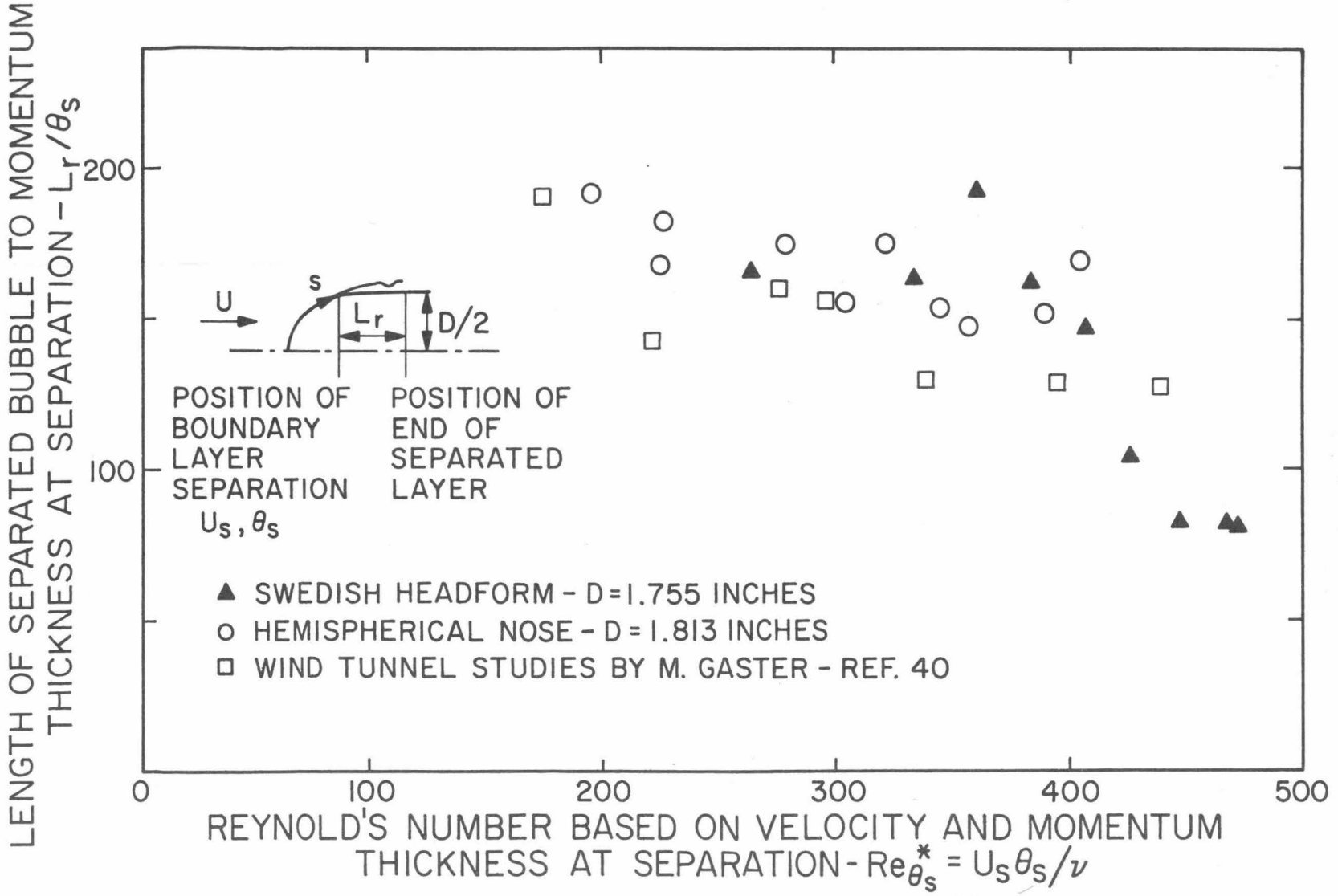

Fig. 28. Variation of the length of the laminar separated bubble for the two test models in non-dimensional form with Reynolds number. Also shown is similar data obtained by Gaster[40] in wind tunnel studies.

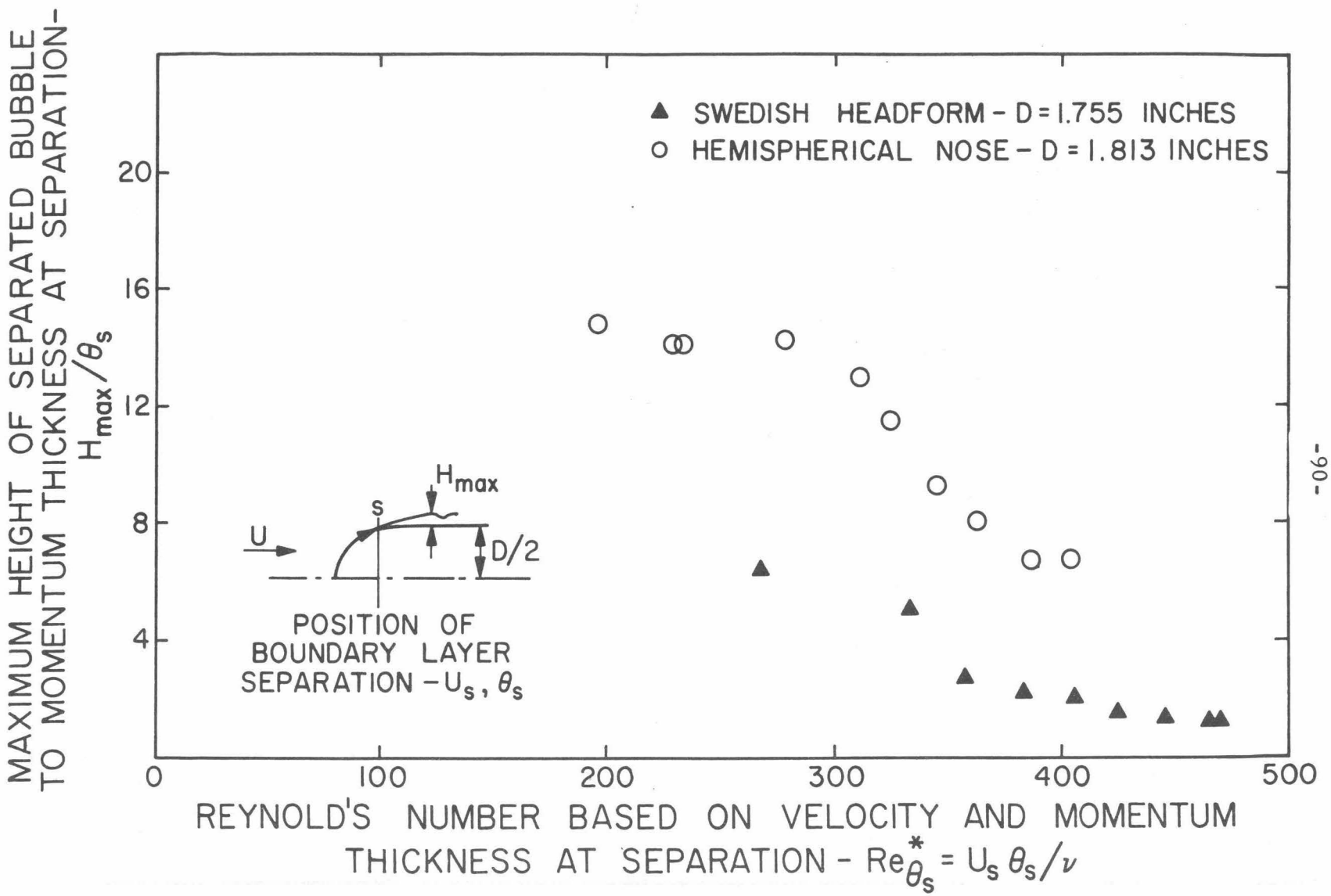

Fig. 29. Variation of non-dimensional maximum height of the laminar separated bubble indicated by the schlieren photographs for both the test models with Reynolds number.

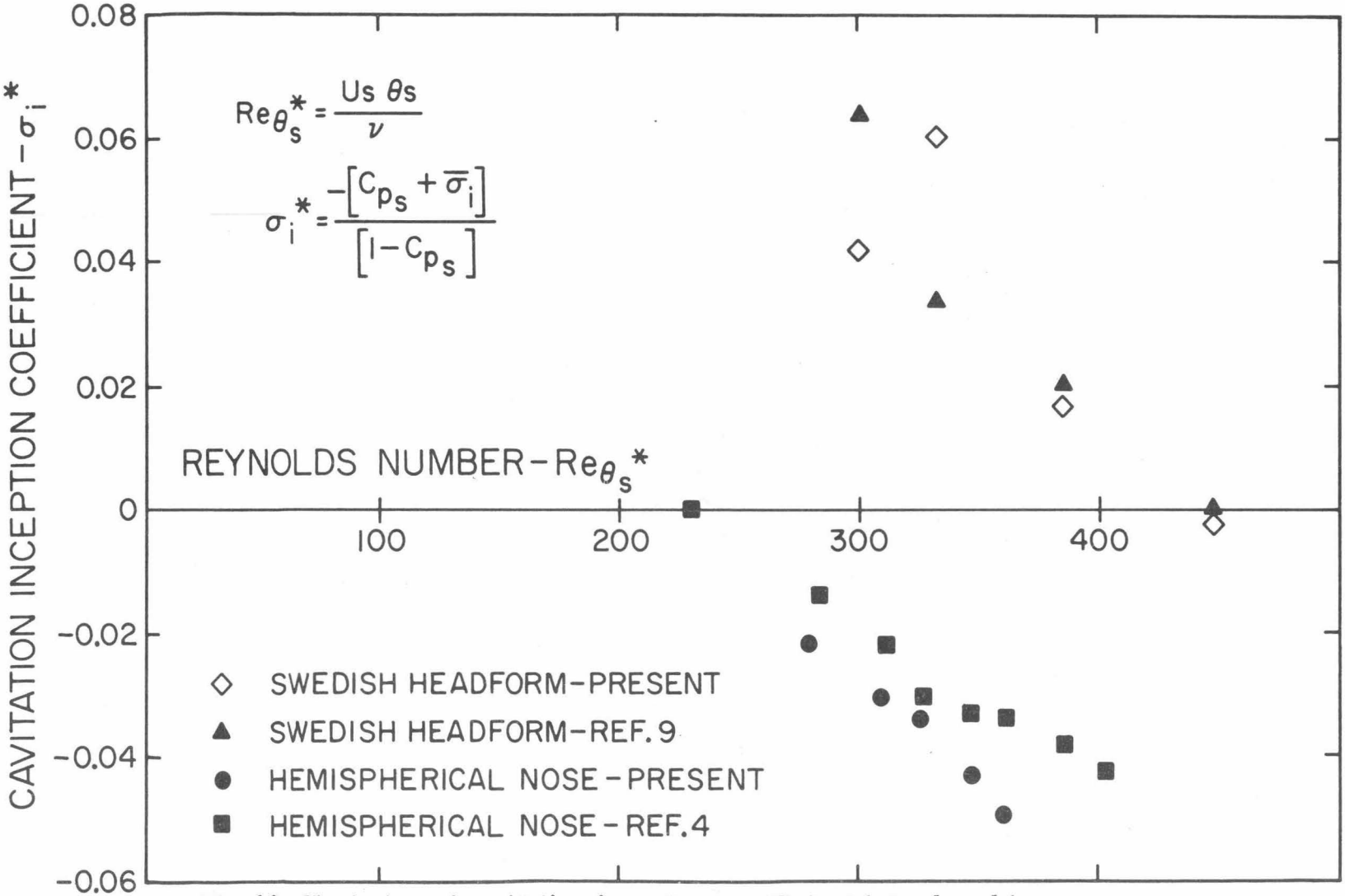

Fig. 30. Variation of cavitation inception coefficient introduced in present work with Reynolds number for different models.

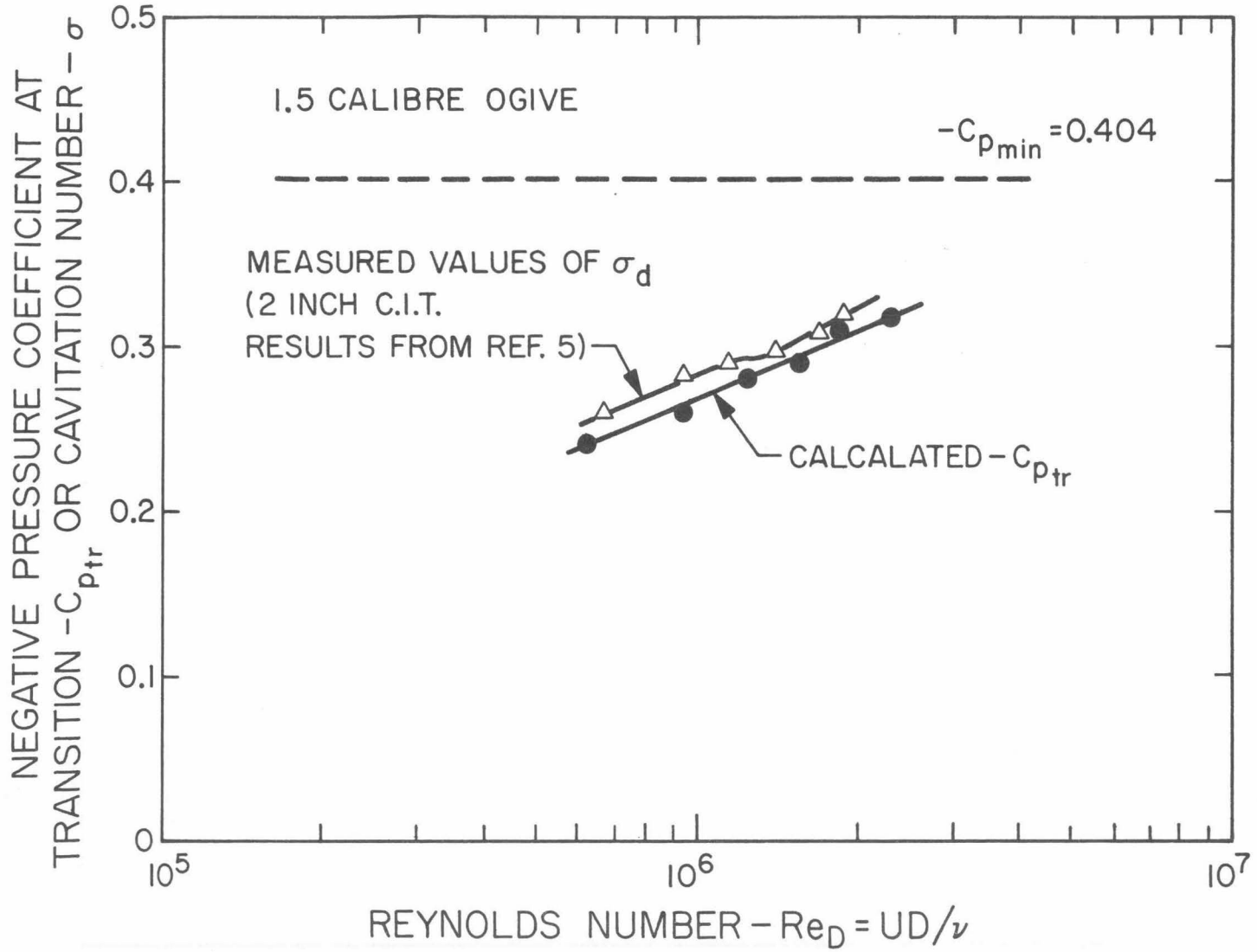

Fig. 31. Comparison of incipient cavitation index for 1.5 calibre ogive with the negative value of the pressure coefficient at the predicted point of transition for $Re_D > Re_{D\,crit}$.

PART II

A SEMI-EMPIRICAL METHOD TO PREDICT CAVITATION SEPARATION ON SMOOTH BODIES

1. INTRODUCTION

In Part I, we have considered the problem of cavitation inception on bodies which possess laminar boundary layer separation. In the present section we are concerned with the problem of subsequent cavitation development on such bodies with the reduction of σ sufficiently below that of σ_i. In particular, we are interested in viscous effects on the beginning position of the developed cavity, which we may call the position of cavitation separation.

In order to predict analytically the force coefficients on bodies with fully developed cavities, a knowledge of the position of cavitation separation is essential. Bodies with sharp corners such as discs, wedges and sharp-edged hydrofoils at large angles of attack possess cavitation separation whose position is known apriori and force coefficients for such bodies can be predicted quite well within the potential flow approximations[47]. But, for the case of smooth bodies the condition of "smooth separation" is used to predict the position of cavitation detachment[47]. The above mentioned condition does not take into account the possibilities of real fluid effects on the position of cavitation separation. Recent experimental studies[48, 6] have shown that the position of cavitation separation on smooth bodies does depend on Reynolds number or is influenced by viscous effects. Further, it was also observed that the experimentally found position of cavitation separation lies considerably downstream than that predicted by the

condition of smooth separation. On a sphere[48] the difference was of the order of 40° at an Re_D of 10^4 and, the difference decreased with increase in Re_D.

Similar results were noted for the case of a bi-convex hydrofoil[6]. On this hydrofoil, linearized theory with cavitation separation positions determined by smooth separation condition predicted positive lift coefficients at small positive angles of attack. Experiments, on the contrary, showed negative lift coefficients at the same angles of attack. This discrepancy was directly related to the erroneous prediction of cavitation separation position by the smooth separation criterion. This example illustrates the extremely important role the position of the point of cavitation separation has in determining overall forces, yet very little attention has been devoted to this subject.

In the latter study[6] it is mentioned that two different types of cavitation separation are observed on a smooth body, namely a) viscous laminar cavitation separation and b) nucleate cavitation separation. Physical appearance of these two types of separation is very different as illustrated by the two photographs of Fig. 1. Brennen[48] has observed the type (a) separation on a sphere even at Reynolds number of 10^6. From present studies of Part I, we have a better idea of what is physically involved in the two types of separation. It must be concluded that viscous laminar cavitation separation is observed only on bodies which possess a laminar boundary layer separation under non-cavitating conditions. For such bodies it was observed in Part I that inception of cavitation does take place first within the separated layer and if for

some reason it did not, as was the case when electrolysis bubbles were introduced, nucleate type separation was observed on the same body and at the same Reynolds number as shown by Fig. 24(c) and Fig. 24(d) of Part I. Thus, it is apparent that the type of cavitation separation to be expected on a smooth body is dependent on the complete history of cavitation development.

Part II is intended to take a deeper look at the nature of real fluid flow in the neighborhood of viscous laminar cavitation separation with the help of the schlieren method as flow visualization technique. Furthermore, an attempt will be made to develop a semi-empirical method of predicting cavitation separation on bodies which possess laminar boundary layer separation under fully wetted conditions with the hope that the present method will be superior to that of using the smooth separation condition.

2. EXPERIMENTAL PROCEDURE

The same experimental methods described in section 2 of Part I were used for present work. Schlieren silhouette photographs of the fully developed cavity were taken with the spark gap light source for both the models, at various tunnel velocities and cavitation numbers. Such a photograph is illustrated in Fig. 2 for the Swedish headform taken at a tunnel velocity of 25.6 ft/sec. and $\sigma = 0.39$. It should be noted from this photograph that the cavity separation is preceded by the laminar boundary layer separation. The streamwise distance between the two separations is denoted by "λ". With the help of such photographs it was possible to determine the position of the boundary layer separation, the position of cavitation separation and hence the distance between the two, λ.

3. DISCUSSION OF EXPERIMENTAL RESULTS

Variation of the angular position of the cavity separation with tunnel velocity and cavitation number for the hemispherical nose is shown in Fig. 3. From this Fig. 3 it may be seen that the position of the cavity separation shifts upstream by about 12° with a decrease of σ from .65 to .25, and it shifts downstream by about 8° for a decrease in tunnel velocity from 55 ft/sec. to 25 ft/sec. Similar results have been noted for a sphere[48] in the same Reynolds number range. Figure 4 shows the variation of the angular position of the boundary layer separation which precedes the cavity separation on the hemispherical nose as a function of tunnel velocity and σ. It is important to note from this Fig. 4, that unlike the position of the cavity separation, the position of the boundary layer separation preceding it is <u>independent</u> of the tunnel velocity.

Variation of the streamwise position of the cavity separation and the boundary layer separation preceding it for the Swedish headform as function of the tunnel velocity and σ is shown in Figs. 5 and 6. It may be noticed that the results are similar to that observed for the hemispherical nose and discussed earlier. From the way results are presented in Ref. (9) it is not possible to make a direct comparison between the presently observed positions of the cavity separation and that obtained by Acosta[9]. But, from Fig. 5 it may be seen that the general agreement between the two results mentioned above is fairly good.

The ratio of λ to the diameter of the model, D, is plotted against σ for various tunnel velocities for the hemispherical nose in Fig. 7 and for the Swedish headform in Fig. 8. From these figures it may be noted that λ/D increases with decrease in tunnel velocity, but is almost constant with change in σ or at least did not show any consistent dependence with σ for a fixed velocity. To elucidate the latter point more clearly, the variation of λ/D is plotted against σ in Figs. 9 and 10 for both the models, but at only two velocities for which the maximum amount of data was obtained. These two figures illustrate the point that λ/D is almost independent of σ, even though for the Swedish headform at a tunnel velocity of 40 ft/sec. the scatter is considerable. It should be noted that in general the values of λ/D were quite small; the maximum being 0.07 and the minimum of 0.01 thus, some scatter in the measurement of these small distances should be expected.

With the earlier observation of the independence of λ/D with σ, it is justifiable to take an average value of λ/D for all the meaningful cavitation numbers and this average will be denoted by λ^*/D. Variation of λ^*/D with tunnel velocity for both the models is shown in Fig. 11. Each data point in Fig. 11 represents the averaged value of λ/D along the horizontal axis of the Figs. 7 and 8 at the corresponding velocity.

It is evident that one can determine the position of cavitation separation once the position of the boundary layer separation preceding it and the quantity λ is known. On present models, observations strongly suggest that the position of the boundary layer separation preceding the cavity separation is dependent only on σ, but is

independent of the tunnel velocity and the quantity λ is only dependent on the tunnel velocity, but is independent of σ. Next an attempt will be made to generalize the above mentioned observations based on physical arguments to obtain a correlation using the present results. Then this correlation will be applied to predict cavitation separation on a sphere and a cylinder.

4. A CORRELATION FOR BOUNDARY LAYER SEPARATION WITH CAVITATION

In Part I we have seen the importance of the pressure coefficient at boundary layer separation in cavitation inception; it was also observed that the beginning of the macroscopic cavitation commenced only for cavitation numbers lower than the negative value of the pressure coefficient mentioned above. Since fully developed cavitation occurs for lower cavitation numbers than for the incipient conditions it was found appropriate to use the difference of the values as the significant parameter which may be expressed in a normalized form as $[1+\sigma/(c_{p_s})_{N.C.}]$. This term will be denoted by σ', and it may be thought of as a measure of the extent of cavitation.

As may be seen from Fig. 18(c) of Part I, the presence of the macroscopic cavity shifts the location of the original boundary layer separation upstream to a new position. It seems appropriate that one should consider only this shift as a physically important quantity. Further it was observed that for the same change in the parameter σ', the above mentioned shift was two to three times larger on the Swedish headform than the hemispherical nose. It is believed that this is due to the fact that the hemispherical nose possesses a steeper pressure gradient approaching the point of boundary layer separation (see e.g., Fig. A.1, Appendix A). To take into account the above observations it seemed appropriate to normalize the shift in the boundary layer separation by the distance between the minimum pressure point and

the position of the boundary layer separation. The latter distance was taken to be that existing under non-cavitating conditions. Symbolically, the non-dimensional groups found were,

$$\sigma' = \left[1 + \sigma/(c_{p_s})_{N.C.}\right] \quad \text{and} \quad \Phi = \left[\frac{(s_{B.L.S.}/D)_{N.C.} - (s_{B.L.S.}/D)_{\sigma}}{(s_{B.L.S.}/D)_{N.C.} - (s c_{p\,min}/D)_{N.C.}}\right]$$

A plot of σ' versus Φ for the present models is shown in Fig. 12 and it may be said that the data collapses fairly well. In the construction of Fig. 12 the following information was utilized:

a) $(s_{B.L.S.}/D)_{N.C.} \doteq 0.83$ for the Swedish headform and is obtained from Fig. 15 of Part I. Corresponding $(c_{p_s})_{N.C.} \doteq -.46$ from Fig. A.1 of Appendix A.

b) $(s_{B.L.S.}/D)_{N.C.} \doteq 0.758$ for the hemispherical nose and is obtained from Fig. 14 of Part I. Corresponding $(c_{p_s})_{N.C.} \doteq -.63$ from Fig. A.1 of Appendix A.

c) $(s_{B.L.S.}/D)_{N.C.} - (s\,c_{p\,min}/D)_{N.C.} \doteq 0.2$ for the Swedish headform and is obtained from $(s_{B.L.S.}/D)_{N.C.} \doteq 0.83$ and Fig. A.1 of Appendix A where $(s\,c_{p\,min}/D)_{N.C.} \doteq 0.63$.

d) $(s_{B.L.S.}/D)_{N.C.} - (s\,c_{p\,min}/D)_{N.C.} \doteq 0.078$ for the hemispherical nose and is obtained from $(s_{B.L.S.}/D)_{N.C.} \doteq 0.758$ and Fig. A.1 of Appendix A where $(s\,c_{p\,min}/D)_{N.C.} \doteq 0.68$.

A straight line approximation for the data shown in Fig. 12 gives

$$\Phi = 2.37\left[1 + \sigma/(c_{p_s})_{N.C.}\right] \qquad (1)$$

It is clear that more data is needed to extrapolate the present data with a straight line. But, later we will see that when this straight

line approximation is used to compute the position of cavitation separation on a sphere at σ' as high as .9 good agreement is obtained with experimentally observed values.

Therefore, for given information under non-cavitation conditions and σ, it is possible to determine the position of the boundary layer separation which precedes cavitation separation with the help of Equation (1).

5. A CORRELATION FOR THE DISTANCE BETWEEN THE TWO SEPARATIONS

The physical appearance of cavitation occurring on present models as represented by Fig. 1(b) has striking similarity with the physical appearance of cavitation (in the form of air entrainment) occurring in the diverging sections of oil film lubrication bearings as illustrated by Taylor[49]. Even though the two flow configurations are quite different especially in terms of inertial effects, the similarity is provided from the fact that cavitation on the present models occurs in the separated zone of the viscous laminar boundary layer (see Fig. 18 of Part I) where inertial effects may be quite small as compared to the inertial effects in the outer flow. Pearson[50] has conducted some experiments which are similar in nature to that conducted by Taylor[49], but with a simpler apparatus. The apparatus consisted of a symmetric wedge with divergence angle of 1/20 placed over a flat plate with a minimum clearance of 0.004 in. and the region between the two was filled with different types of liquids possessing high viscosities compared to water. The symmetric wedge was terminated at $x = +1$ in. and $x = -1$ in. in the notation of Fig. 13. It was drawn at measured constant speed perpendicular to planes $x = \text{const}$. This resulted in the suction of an air cavity between the diverging section of the apparatus and the position of the meniscus was determined with flash photographs. The air cavity possessed a characteristic instability in the z-direction with alternate presence of air fingers and fully wetted regions. This is very

similar to the physical appearance of cavitation on present bodies as shown in Fig. 1(b).

For the problem studied by Pearson, the important dimensionless group was found to be $\frac{\mu U_0}{T}$ with h_0 as the pertinent length parameter. $\frac{\mu U_0}{T}$ is commonly known as Taylor-Saffman parameter and is the ratio of Weber number to Reynolds number, both based on U_0. The physical conditions under which cavitation occurs on the present models is shown in Fig. 14, and the similarity with conditions shown in Fig. 13 is very suggestive. With this in mind the important dimensionless group was taken to be Taylor-Saffman parameter with Weber number based on local velocity at separation and Reynolds number based on free stream velocity. In the present symbolic notation, the parameter would be $\frac{\mu U}{T}\left[1-(c_{p_s})_{N.C.}\right]$. The length parameter equivalent to h_0 was chosen to be the momentum thickness at separation.

As discussed earlier it was noted that λ was independent of σ and this allows us to choose the pertinent variables in determining λ at any cavitation number and the most useful condition to choose would be that under non-cavitating conditions or for $\sigma >> 1$. Thus, the non-dimensional groups chosen were $\lambda^*/(\theta_s)_{N.C.}$ and $\frac{\mu U}{T}\left[1-(c_{p_s})_{N.C.}\right]$. A plot of these quantities for the present models is shown in Fig. 15. The value of $(\theta_s)_{N.C.}$ was estimated by Thwaite's approximate method as outlined in Appendix A. Also included in Fig. 14 are results obtained by Pearson (see Fig. 11 of Ref. (50)); b/h_0 in Pearson's experiments is equivalent to $\lambda^*/(\theta_s)_{N.C.}$ for the present experiments and $\frac{\mu U_0}{T}$ is equivalent to $\frac{\mu U}{T}\left[1-(c_{p_s})_{N.C.}\right]$. It may be noted from Fig. 15 that the

agreement between present results and that of Pearson's may be considered quite good especially for low values of the Taylor-Saffman parameter. This agreement indicates that the ideas put forth in determining the distance between the two separations are along the right lines, but further improvements with more data are very desirable. It should be noted that in the present analysis, the possible role of another geometrical parameter equivalent to the wedge angle in Pearson's experiments is not considered. In our problem the above mentioned parameter would be equivalent to the angle of boundary layer separation. Neglect of this parameter may be responsible for some of the scatter in the observed data of Fig. 15.

A straight line approximation for the data of present models in Fig. 15 gives,

$$\lambda^*/(\theta_s)_{N.C.} = 130 - 312 \frac{\mu U}{T} [1 - (c_{p_s})_{N.C.}]. \qquad (2)$$

Since, λ^* can never be negative it should be taken that

$$\lambda^*/(\theta_s)_{N.C.} = 0 \quad \text{for} \quad \frac{\mu U}{T} [1 - (c_{p_s})_{N.C.}] > .42$$

and for values of $\frac{\mu U}{T} [1 - (c_{p_s})_{N.C.}] \leq .42$, equation (2) should be used to evaluate λ^*.

6. THE COMPLETE CORRELATION

One can express the cavity separation position as the sum of the position of the boundary layer separation preceding it and the distance between the two or,

$$(s_{C.S.}/D) = (s_{B.L.S.}/D) + (\lambda^*/D) \tag{3}$$

using the correlations obtained earlier in equations (1) and (2), equation (3) may be written as

$$(s_{C.S.}/D) = (s_{B.L.S.}/D)_{N.C.} - 2.37\left[1 + \frac{\sigma}{(c_{p_s})_{N.C.}}\right] \times$$

$$\left[(s_{B.L.S.}/D)_{N.C.} - (s\, c_{p\,min}/D)_{N.C.}\right] + \tag{4}$$

$$(\theta_s/D)_{N.C.}\left\{130 - 312\frac{\mu U}{T}\left[1 - (c_{p_s})_{N.C.}\right]\right\}.$$

Therefore, in general

$$(s_{C.S.}/D) = (s_{C.S.}/D)\left[Re_D,\ \sigma,\ (c_{p_s})_{N.C.},\ We\right]. \tag{5}$$

To use equation (4), the knowledge of the pressure distribution on the headform under non-cavitating conditions is a requirement and the position of the boundary layer separation should be known or may be estimated from the method outlined in Appendix A. The method of estimating $(\theta_s)_{N.C.}$ is explained in the same Appendix. It should be noted that equation (4) is valid only for $\frac{\mu U}{T}\left[1 - (c_{p_s})_{N.C.}\right] < .42$; for values of this term greater than 0.42, the third term vanishes.

7. COMPUTATIONS USING THE COMPLETE CORRELATION

Computations were carried out to predict the position of cavitation separation on spheres and a cylinder for various Reynolds number range and cavitation numbers. For these calculations it is convenient to convert equation (4) in terms of angular positions, then

$$\gamma^{\circ}_{C.S.} = (\gamma_{B.L.S.})^{\circ}_{N.C.} - 2.37\left[1+\frac{\sigma}{(c_{p_s})_{N.C.}}\right]\left[(\gamma_{B.L.S.})^{\circ}_{N.C.} - (\gamma c_{p\,min})^{\circ}_{N.C.}\right]$$

$$+ \left(\frac{360}{3.14}\right)\left[\left(\frac{\theta_s}{D}\right)_{N.C.}\right]\left\{130 - 312\,\frac{\mu U}{T}\left[1-(c_{p_s})_{N.C.}\right]\right\}^{\circ} \qquad (6)$$

where γ represents the angular position from the stagnation point. The following information under non-cavitating conditions was obtained with the help of experimental pressure distributions from various references,

SPHERE

a) $10^4 < Re_D < 10^5$ - From Ref. (51) — Below the first critical Reynolds number

$(\gamma_{B.L.S.})_{N.C.} \doteq 82.5^{\circ}$

$(\gamma c_{p\,min})_{N.C.} \doteq 74^{\circ}$

$(c_{p_s})_{N.C.} \doteq -.4$

b) $Re_D = 2 \times 10^5$ - From Ref. (51) — At the first critical Reynolds number

$(\gamma_{B.L.S.})_{N.C.} \doteq 82.5^{\circ}$

$(\gamma c_{p\,min})_{N.C.} \doteq 72.5^{\circ}$

$(c_{p_s})_{N.C.} \doteq -.46$

c) $Re_D > 3 \times 10^5$ - From Ref. (51) — Above the first critical Reynolds number

$(\gamma_{B.L.S.})_{N.C.} \doteq 109°$

$(\gamma c_{p\,min})_{N.C.} \doteq 90°$

$(c_{p_s})_{N.C.} \doteq -1.02°$

CYLINDER

$10^4 < Re_D < 10^5$ - From Ref. (42) — Below the first critical Reynolds number

$(\gamma_{B.L.S.})_{N.C.} \doteq 80°$

$(\gamma c_{p\,min})_{N.C.} \doteq 70°$

$(c_{p_s})_{N.C.} \doteq -1.1875$

Momentum thickness at the boundary layer separation under non-cavitating conditions was estimated by Thwaite's method and is shown in Fig. A.5 of Appendix A.

SAMPLE CALCULATIONS - SPHERE

$U = 10$ ft/sec., $\sigma = .1$, $D = 1/2"$

$Re_D \cong 4 \times 10^4$ from Appendix A $\Rightarrow (\theta_s/D)_{N.C.} \cong 14 \times 10^{-4}$

$\mu = 2.05 \times 10^{-5} \frac{lb\,f - sec.}{ft^2}$, $T = .0047 \frac{lb\,f}{ft}$

and from Ref. (51), as mentioned above

$(\gamma_{B.L.S.})_{N.C.} \cong 82.5°$, $(\gamma c_{p\,min})_{N.C.} \cong 74°$, $(c_{p_s})_{N.C.} \cong -.4$

$\therefore \quad \frac{\mu U}{T} [1 - (c_{p_s})_{N.C.}] \cong .061$, $[1 + \frac{\sigma}{(c_{p_s})_{N.C.}}] = .75.$

Using above values in expression (6) one gets

$$\gamma_{C.S.} = 82.5° - [2.37\,(.75)(82.5° - 74°)]$$

$$+ \left\{\frac{360}{3.14} \times 14 \times 10^{-4} \times [130 - 312\,(.061)]\right\}^{\circ}$$

$$\gamma_{C.S.} \cong 82.5° - 15° + 17.8° \cong 85.3°.$$

Similar calculations for sphere and cylinder at various Reynolds number and cavitation numbers are shown in Figs. 16, 17 and 18.

8. COMPARISON WITH EXPERIMENTS

Also shown in Figs. 16, 17 and 18 are experimentally found positions of cavitation separation obtained by Brennen[48, 52]. Also marked is the position of cavitation separation obtained theoretically by using the smooth separation condition and computed by Brennen[53].

From Fig. 16, at $\sigma = .1$ the calculated values follow the same trend with Re_D as the experimentally observed values and are within 7°. From Fig. 17, at $\sigma = .25$ the agreement is much better and the calculated values are within 4° of that found experimentally and similar results are seen for $\sigma = 0.5$ in the same Fig. 17. The important point to note from these figures is that the slope of the calculated curves and experimentally found curves is in excellent agreement for all Reynolds numbers and cavitation numbers. From Fig. 17, at $\sigma = 0.25$, the discontinuity in the observed positions just before and after the first $Re_{D\,crit}$ for a sphere is also predicted from present calculations.

From Fig. 18, for a cylinder the agreement is very good at an Re_D of 10^4 but gradually differs by about 10° at Re_D of 10^5.

Prediction of the position of cavitation separation for three different fluids which possess different values of μ/T is shown in Fig. 19. The value of the coefficient of surface tension, T, for mercury is about 8 times that of water and for benzene it is one-half of that for water. It may be concluded from Fig. 19 that for low Reynolds number range ($Re_D < 8 \times 10^4$), viscous forces dominate in determining the position of cavitation separation on a sphere and this is consistent with the experimental observations of Brennen[52].

9. CONCLUDING REMARKS

The proposed method to predict the position of cavitation separation applies only to bodies which possess laminar boundary layer separation under fully wetted conditions.

On such bodies with a fully developed cavity, cavitation separation is observed to be preceded by a laminar boundary layer separation and the distance between the two separations shows a strong dependence on Reynolds number.

The present method is based on data acquired on only two different models; further acquisition of data on different bodies with present experimental techniques would strengthen the validity of and may improve the proposed empirical method.

The predicted values of the position of cavitation separation based on present methods on a sphere for Reynolds number range of 10^4 to 10^6 showed good agreement with the experimentally observed values and are far superior to that predicted by the smooth separation condition used in classical free streamline analysis.

LIST OF FIGURE CAPTIONS - PART II

Fig. 1. Photographs illustrating the striking difference in the physical appearance of cavitation in the cases of nucleate cavitation separation and viscous laminar cavitation separation.

Fig. 2. Silhouette schlieren photograph showing existence of the laminar boundary layer separation upstream of cavitation separation on the Swedish headform with a fully developed cavity. $U = 25.6$ ft/sec., $\sigma = .39$. The actual distance between the two separations is 0.11 in.

Fig. 3. Variation of angular position of cavitation separation with tunnel velocity and cavitation number for the hemispherical nose.

Fig. 4. Variation of angular position of boundary layer separation under cavitating conditions with tunnel velocity and cavitation number for the hemispherical nose.

Fig. 5. Variation of the streamwise position of cavitation separation on the Swedish headform with tunnel velocity and cavitation number.

Fig. 6. Variation of the streamwise position of the boundary layer separation under cavitating conditions on the Swedish headform with tunnel velocity and cavitation number.

Fig. 7. Variation of the streamwise distance between the position of boundary layer separation and the cavity separation with tunnel velocity and cavitation number for the hemispherical nose.

Fig. 8. Variation of the streamwise distance between the position of boundary layer separation and the cavity separation with tunnel velocity and cavitation number for the Swedish headform.

Fig. 9. Data of Fig. 7 at only two velocities for which maximum amount of data was obtained.

Fig. 10. Data of Fig. 8 at only two velocities for which maximum amount of data was obtained.

Fig. 11. Variation of the streamwise distance between the position of boundary layer separation and the cavity separation at any cavitation number with tunnel velocity for both the test models.

Fig. 12. A correlation plot to determine the position of boundary layer separation under cavitating conditions.

Fig. 13. A schematic drawing showing the apparatus used by Pearson[50] to study the entrainment of an air cavity in the diverging section of a wedge.

Fig. 14. A schematic drawing showing the physical conditions under which cavitation occurs on the present models.

Fig. 15. A correlation plot to determine the distance from the position of boundary layer separation to the position of cavitation separation.

Fig. 16. Comparison of presently calculated position of cavitation separation with experimentally observed position on sphere for $10^4 < Re_D < 10^6$ at $\sigma = .1$.

Fig. 17. Comparison of presently calculated position of cavitation separation with experimentally observed position on sphere for $10^4 < Re_D < 10^6$ at $\sigma = .25$ and .5.

Fig. 18. Comparison of presently calculated position of cavitation separation with experimentally observed position on cylinder for $10^4 < Re_D < 10^5$ at $\sigma = .5$.

Fig. 19. Comparison of calculated position of cavitation separation on sphere at $\sigma = .1$ for three different liquids with different physical properties.

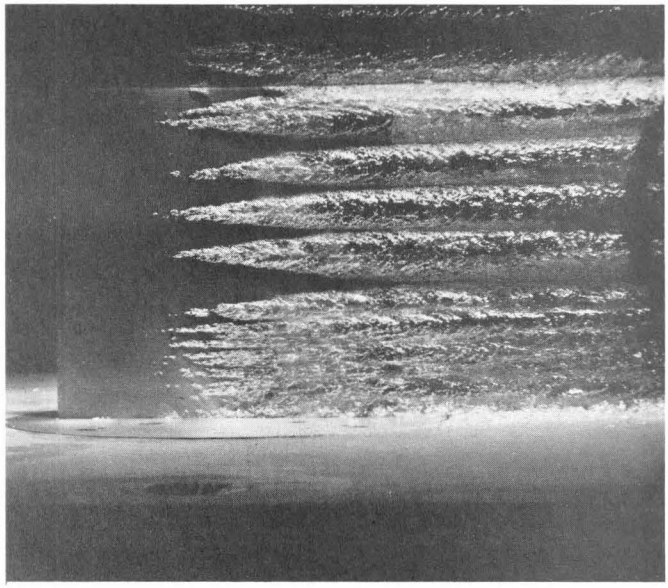

Plate 1: Cavitation on a bi-convex hydrofoil showing nucleate cavitation separation.
U = 51 ft/sec σ = .11 Ref. 6

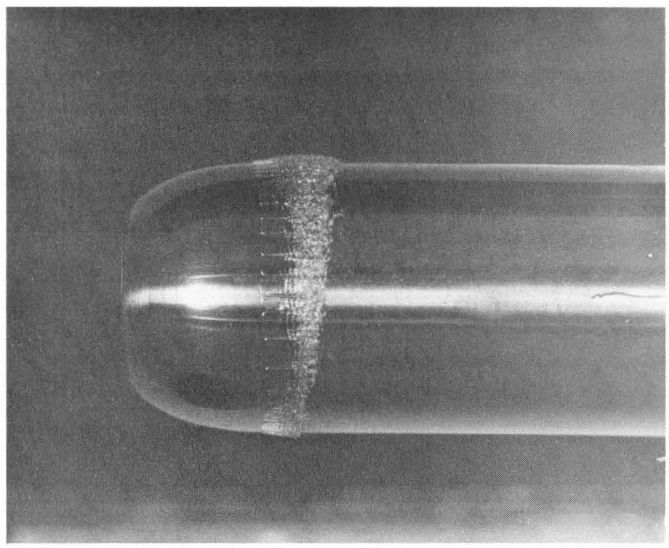

Plate 2: Cavitation on Swedish headform showing viscous laminar cavitation separation.
(Courtesy of Dr. A. J. Acosta)
U = 40 ft/sec σ = .424 Ref. 9

Fig. 1. Photographs illustrating the striking difference in the physical appearance of cavitation in the cases of nucleate cavitation separation and viscous laminar cavitation separation.

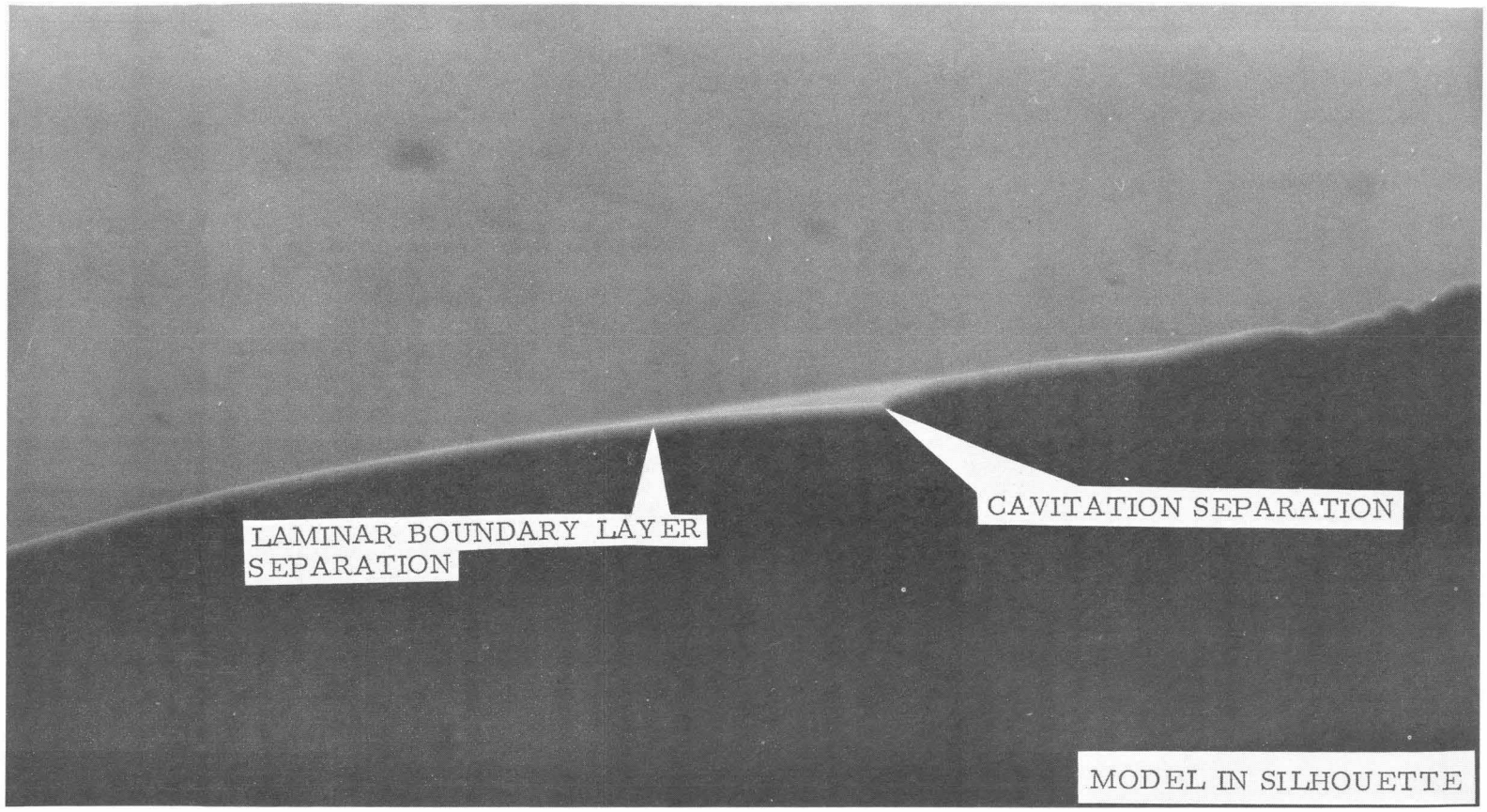

Fig. 2. Silhouette schlieren photograph showing the existence of the laminar boundary layer separation upstream of cavitation separation on the Swedish headform with a fully developed cavity. $U = 25.6$ ft/sec., $\sigma = .39$. The actual distance between the two separations is 0.11 in.

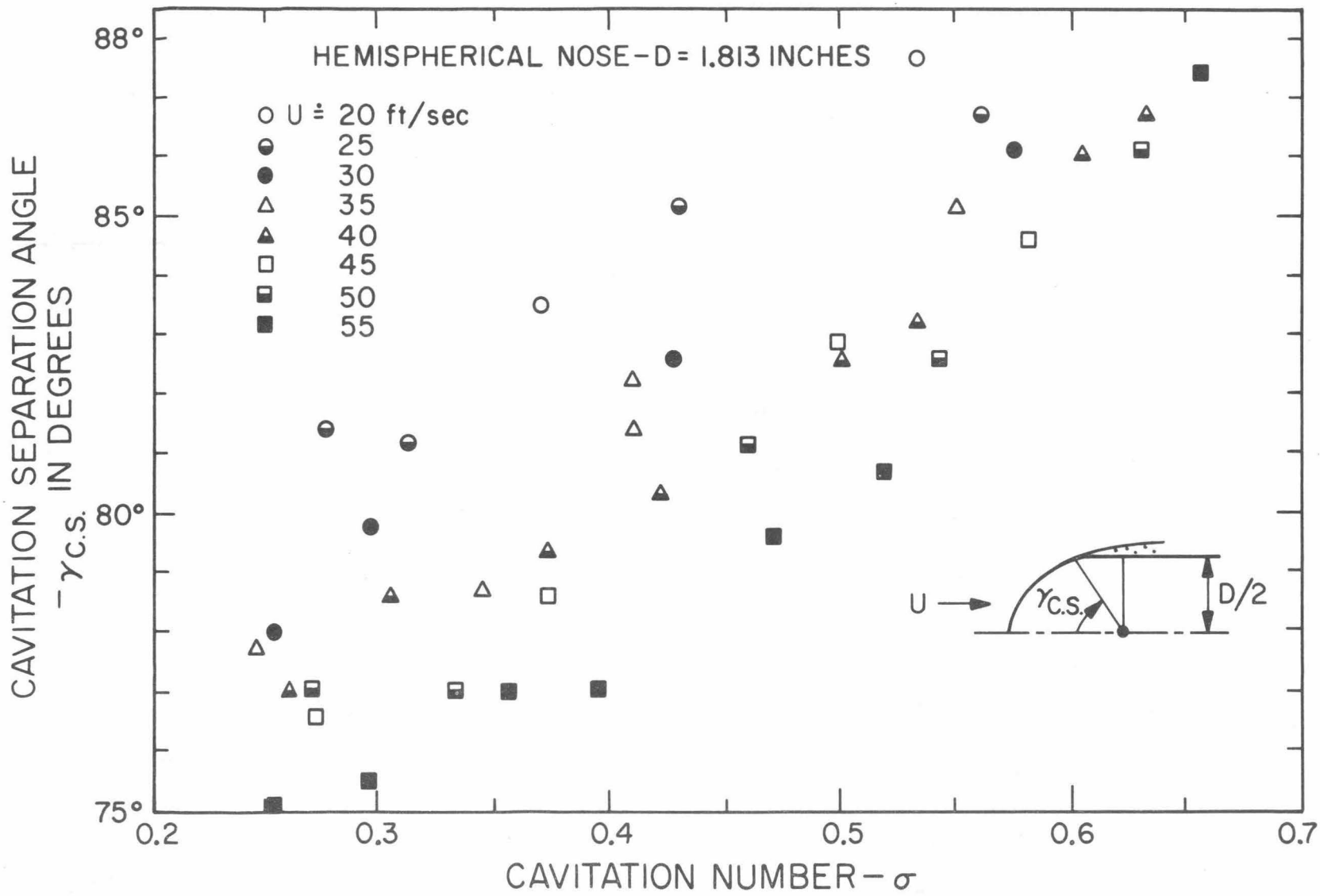

Fig.3. Variation of angular position of cavitation separation with tunnel velocity and cavitation number for the hemispherical nose.

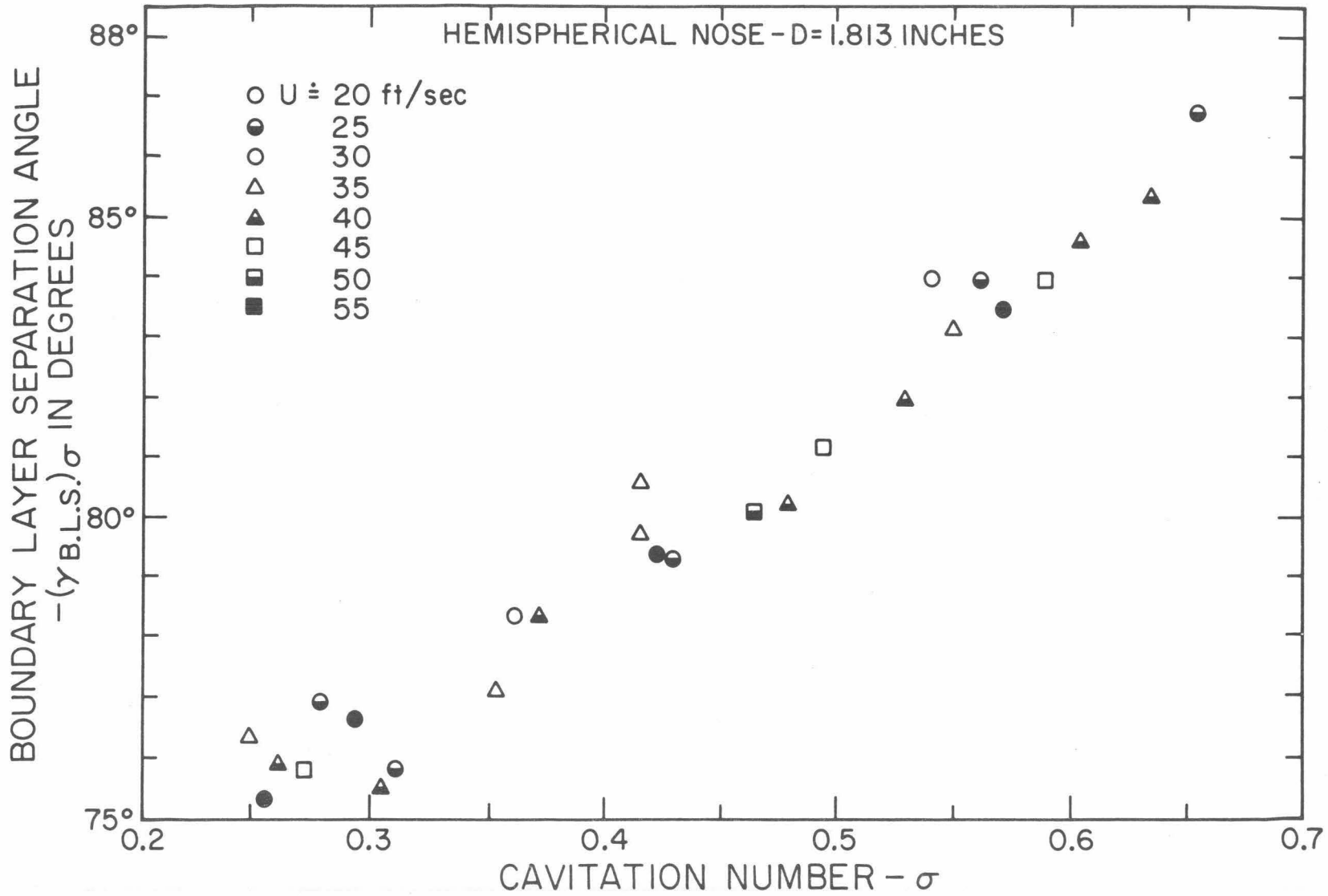

Fig.4. Variation of angular position of boundary layer separation under cavitating conditions with tunnel velocity and cavitation number for the hemispherical nose.

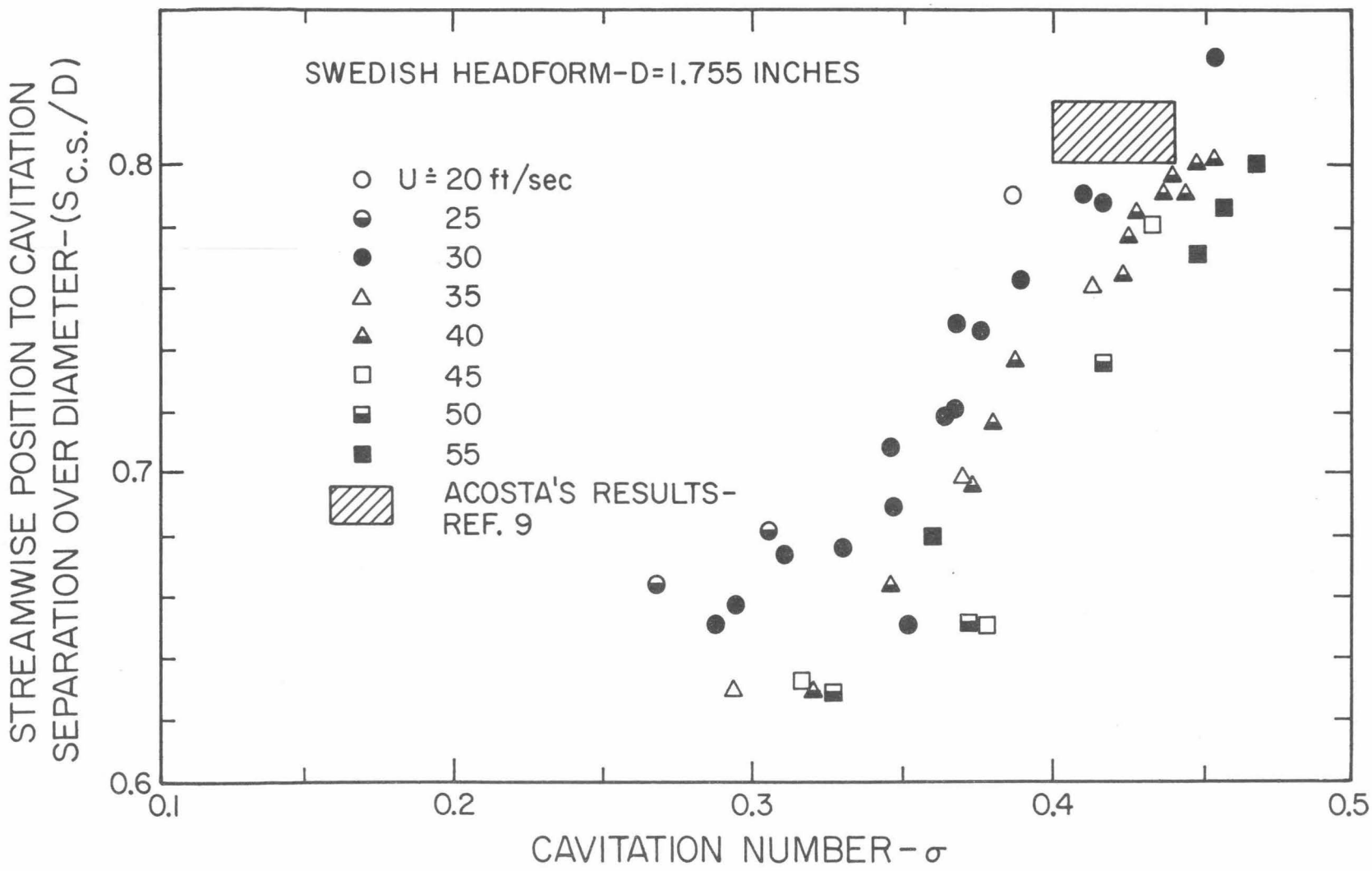

Fig.5. Variation of the streamwise position of cavitation separation on the Swedish headform with tunnel velocity and cavitation number.

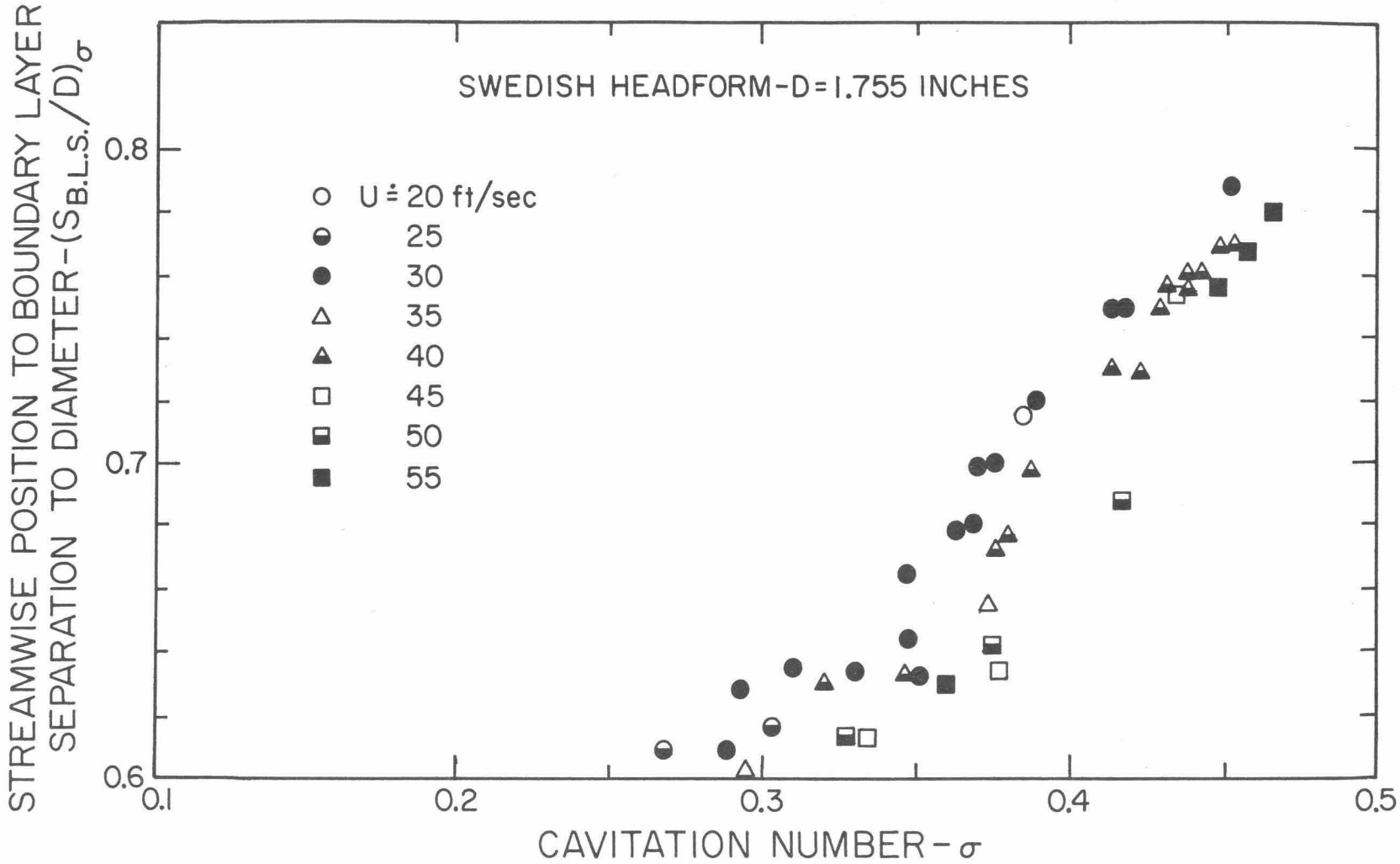

Fig.6. Variation of the streamwise position of the boundary layer separation under cavitating conditions on the Swedish headform with tunnel velocity and cavitation number.

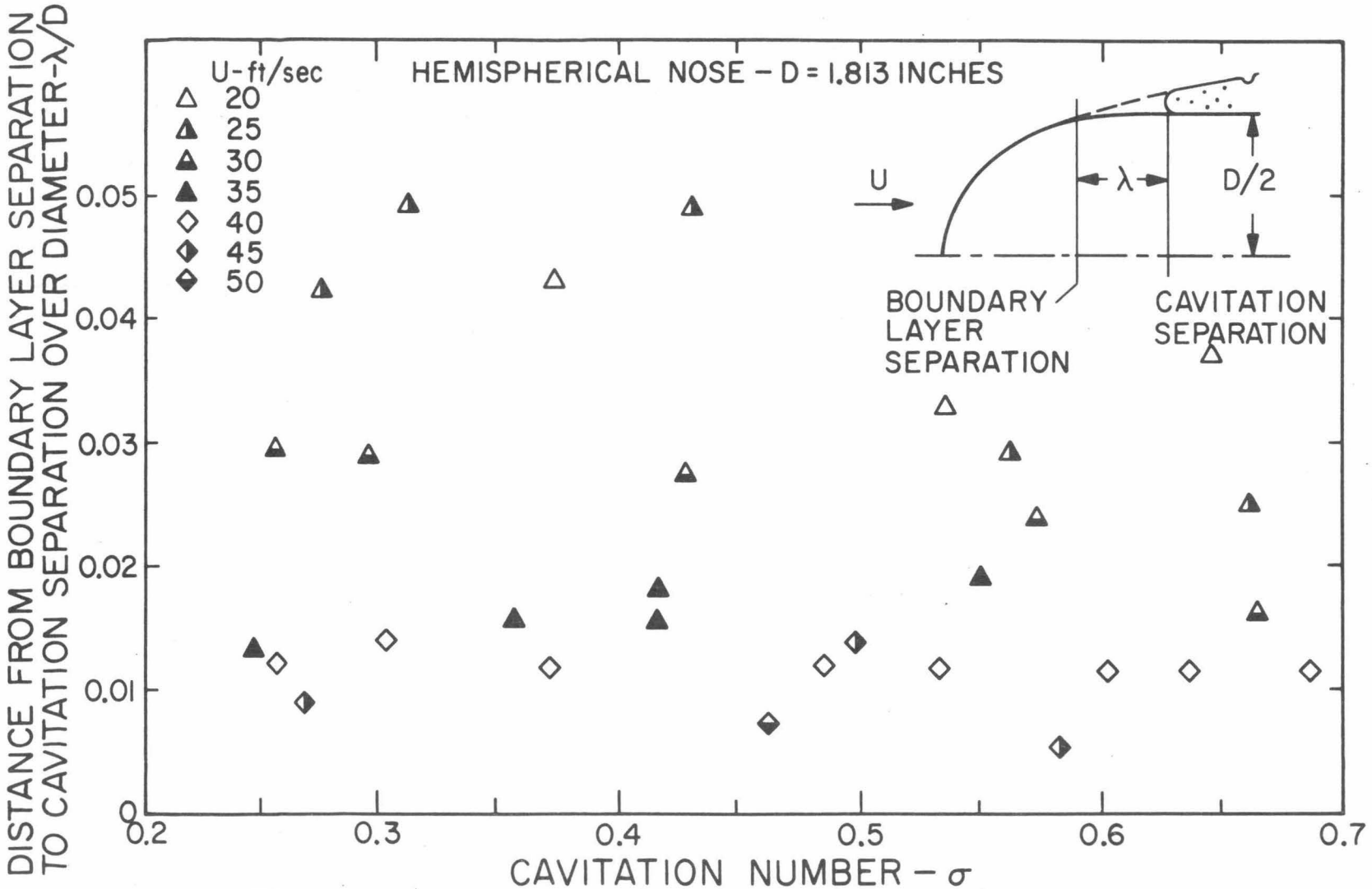

Fig.7. Variation of the streamwise distance between the position of boundary layer separation and the cavity separation with tunnel velocity and cavitation number for the hemispherical nose.

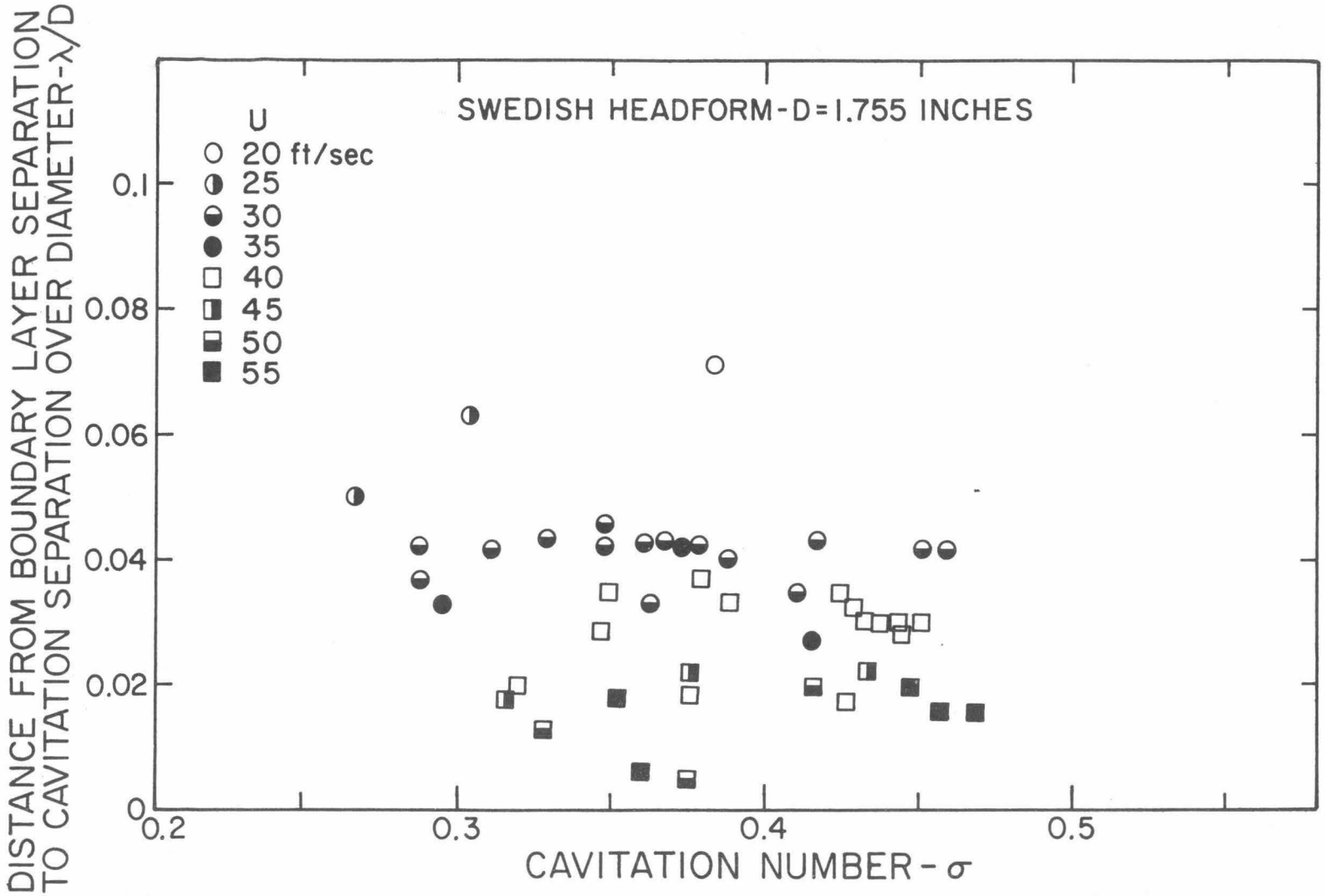

Fig. 8. Variation of the streamwise distance between the position of boundary layer separation and the cavity separation with tunnel velocity and cavitation number of the Swedish headform.

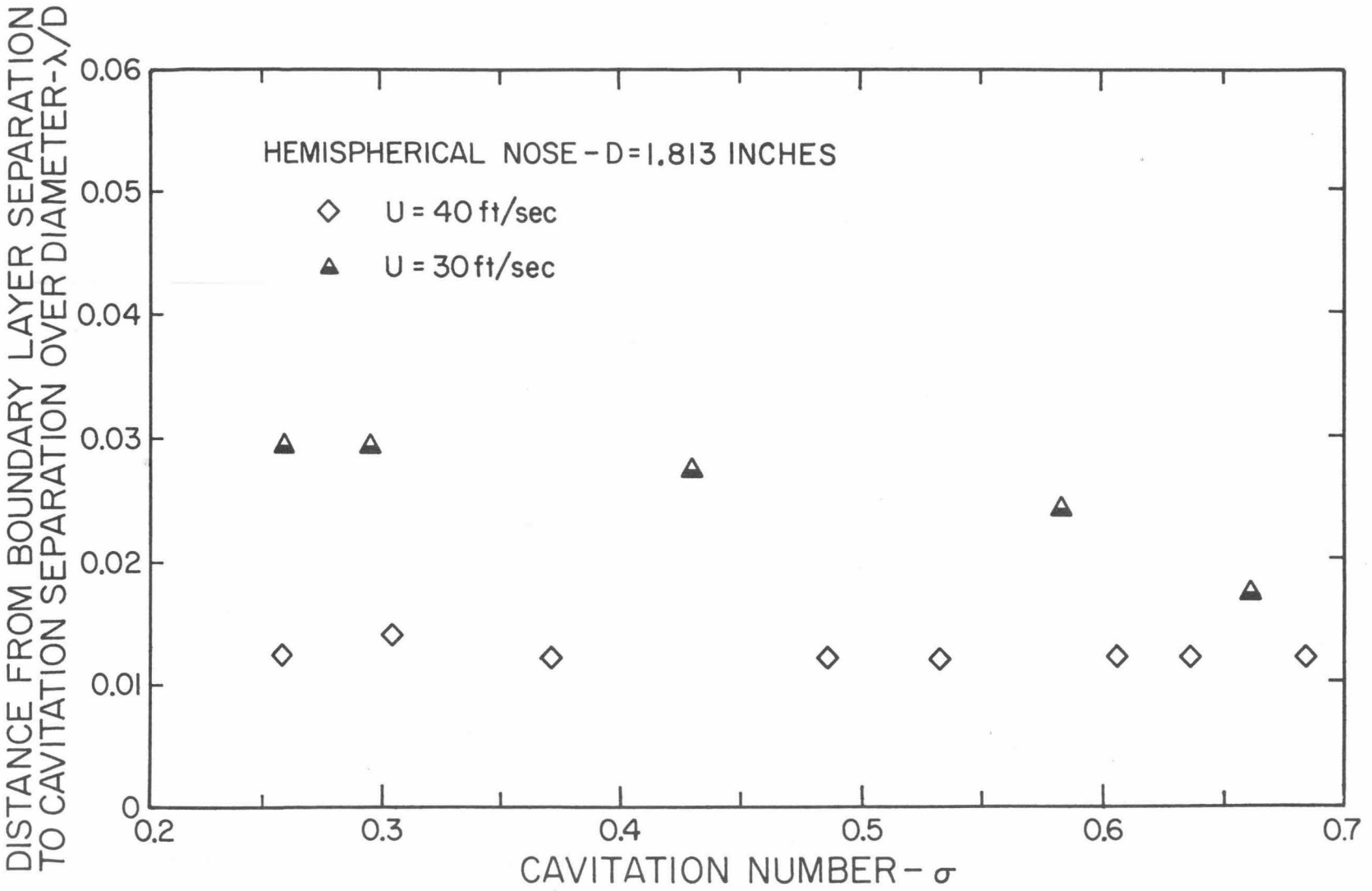

Fig. 9. Data of Fig. 7 at only two velocities for which maximum amount of data was obtained.

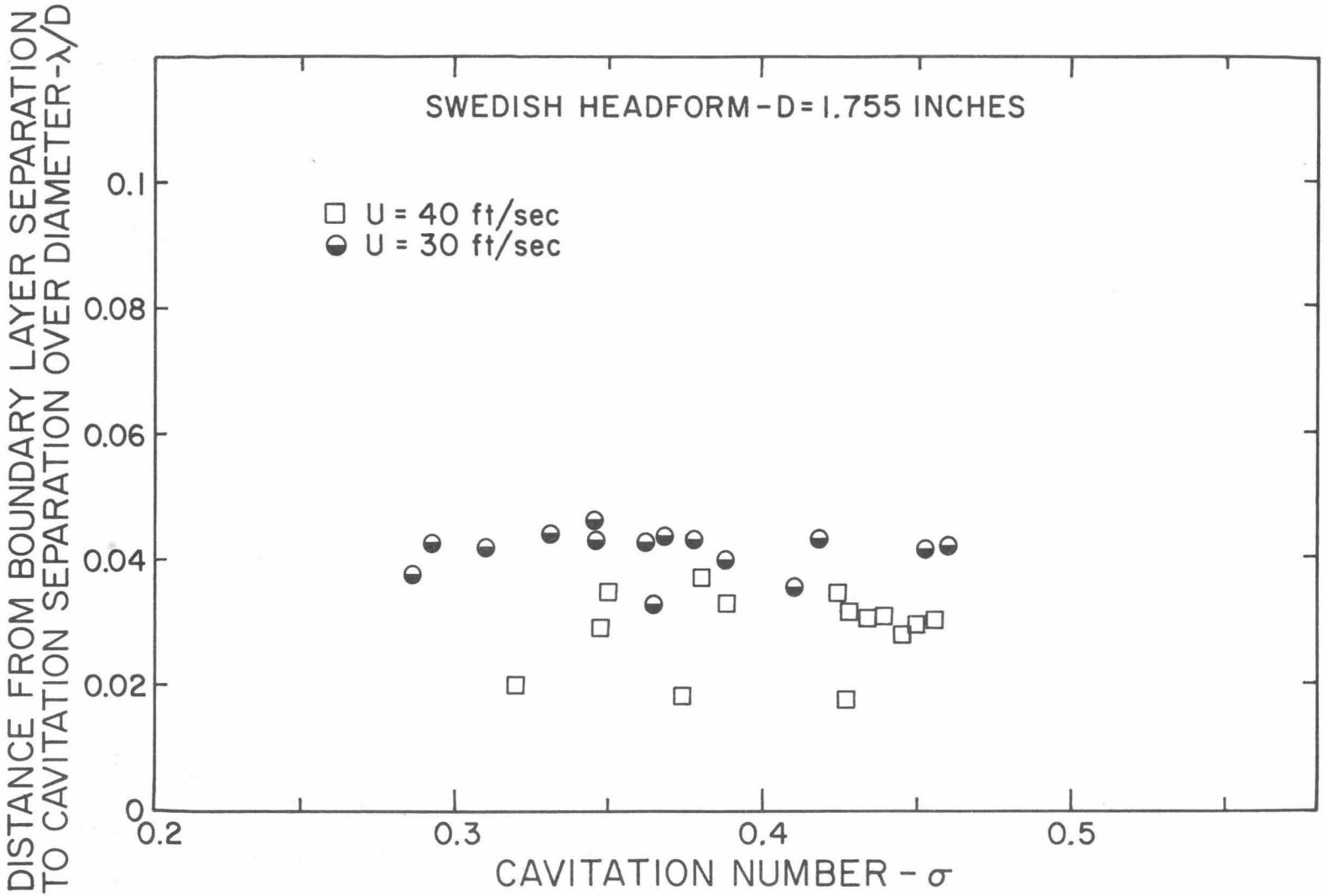

Fig.10. Data of Fig. 8 at only two velocities for which maximum amount of data was obtained.

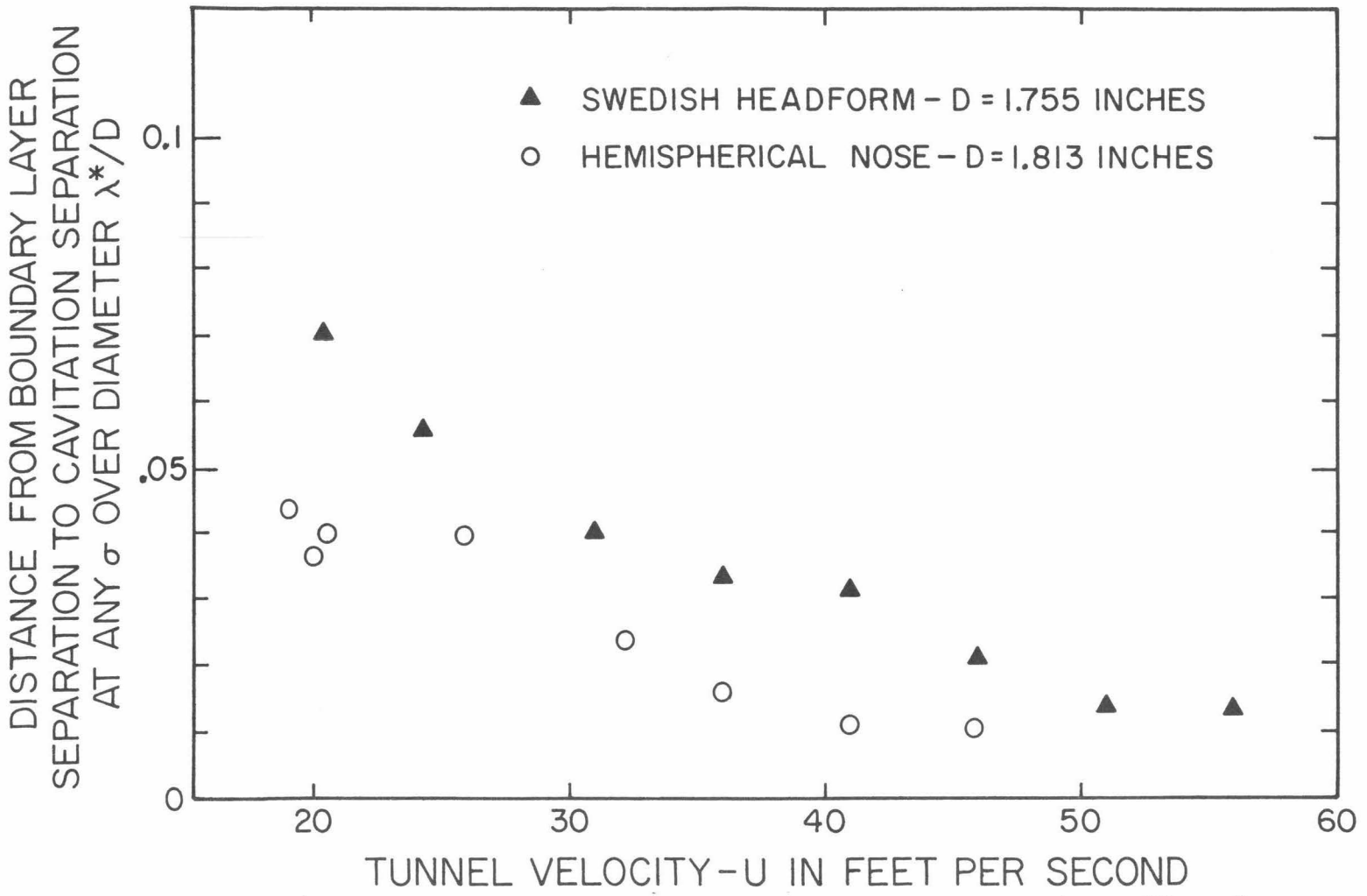

Fig.11. Variation of the streamwise distance between the position of boundary layer separation and the cavity separation at any cavitation number with tunnel velocity for both the test models.

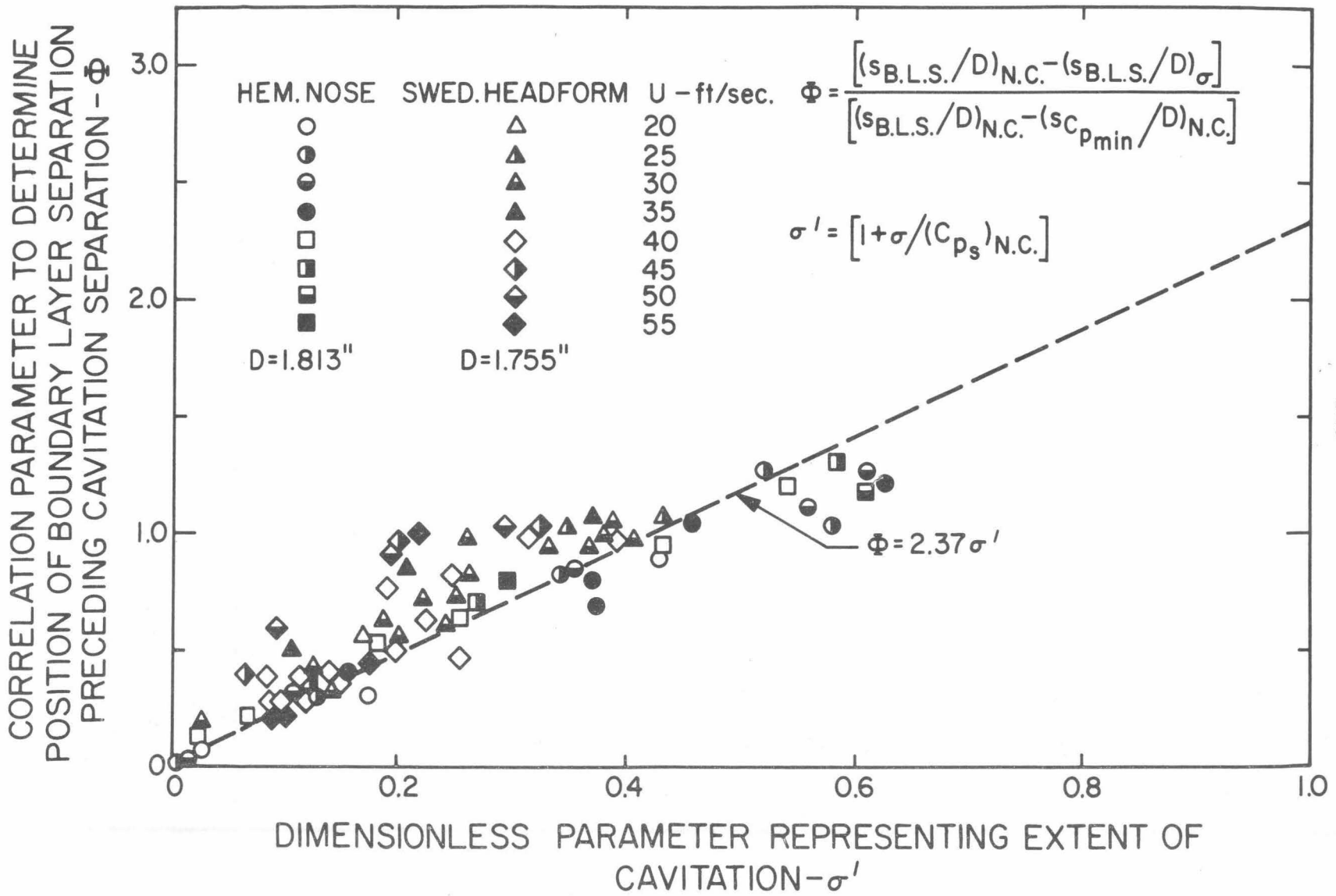

Fig.12. A correlation plot to determine the position of boundary layer separation under cavitating conditions.

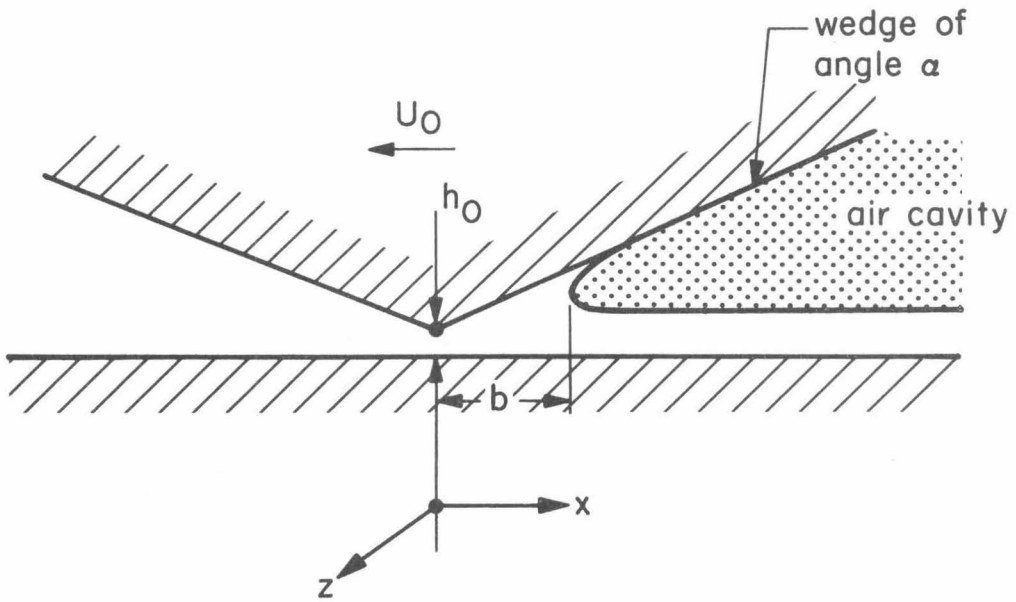

Fig. 13. A schematic drawing showing the apparatus used by Pearson[50] to study the entrainment of a air cavity in the diverging section of a wedge.

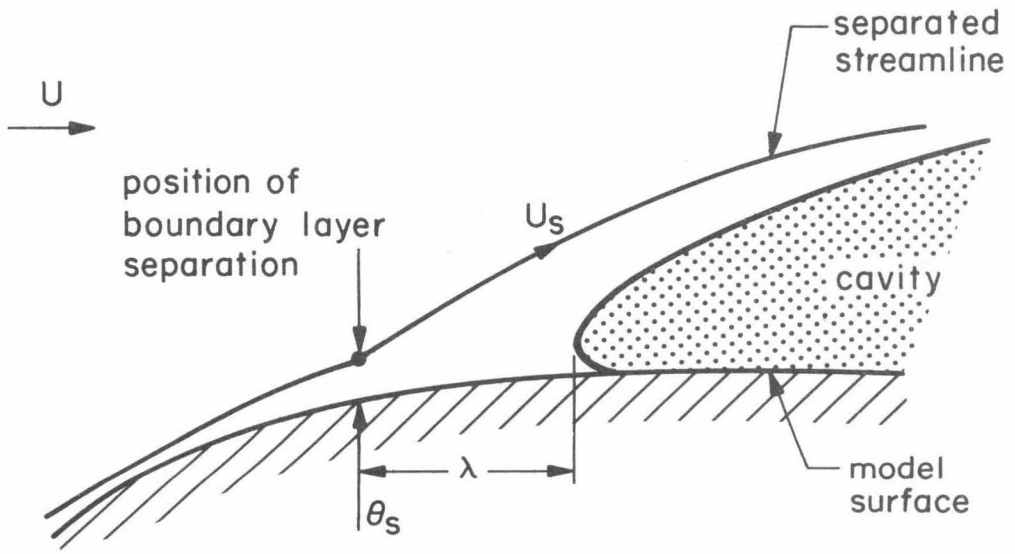

Fig. 14. A schematic drawing showing the physical conditions under which cavitation occurs on the present models.

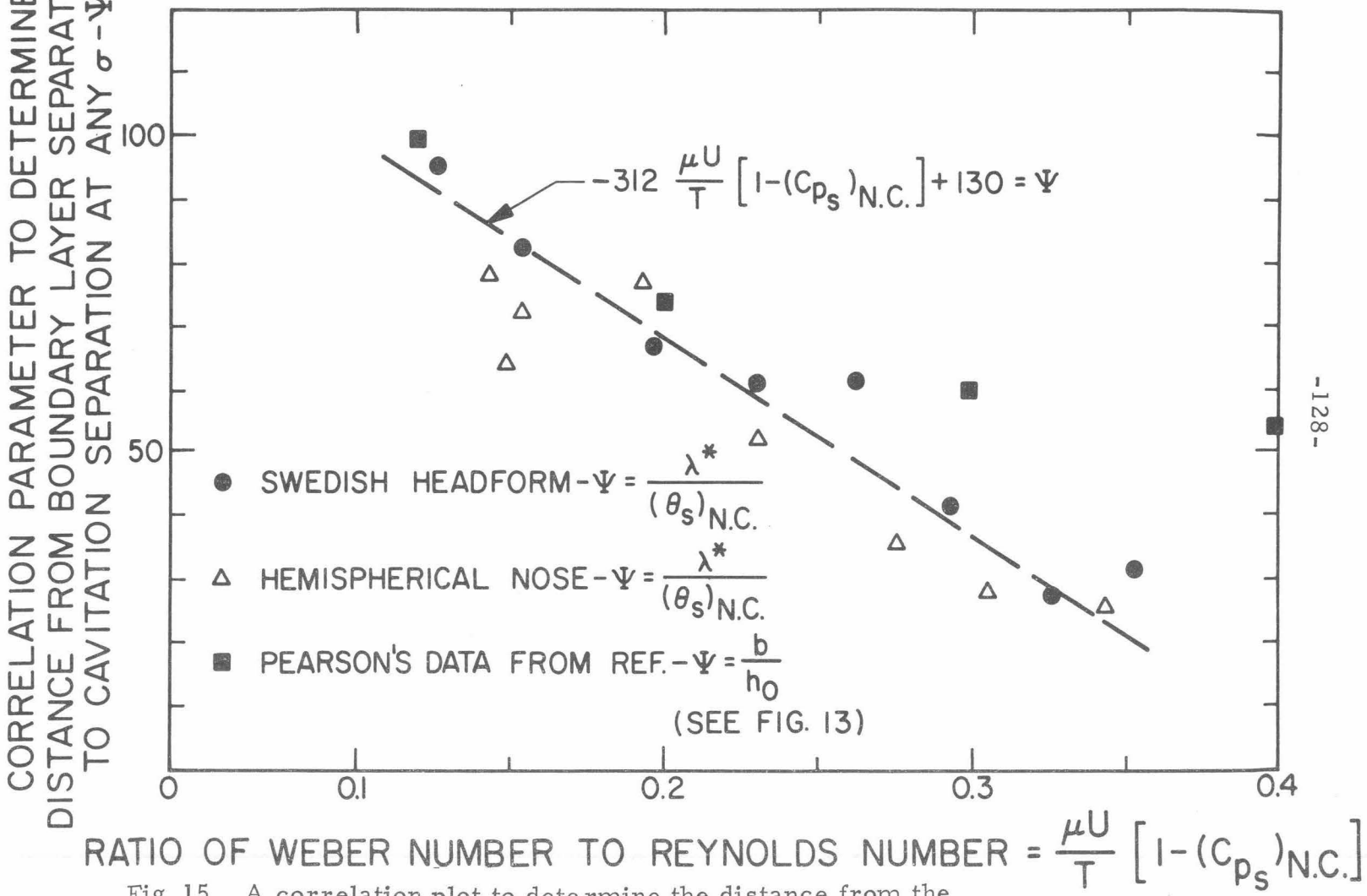

Fig. 15. A correlation plot to determine the distance from the position of boundary layer separation to the position of cavitation separation.

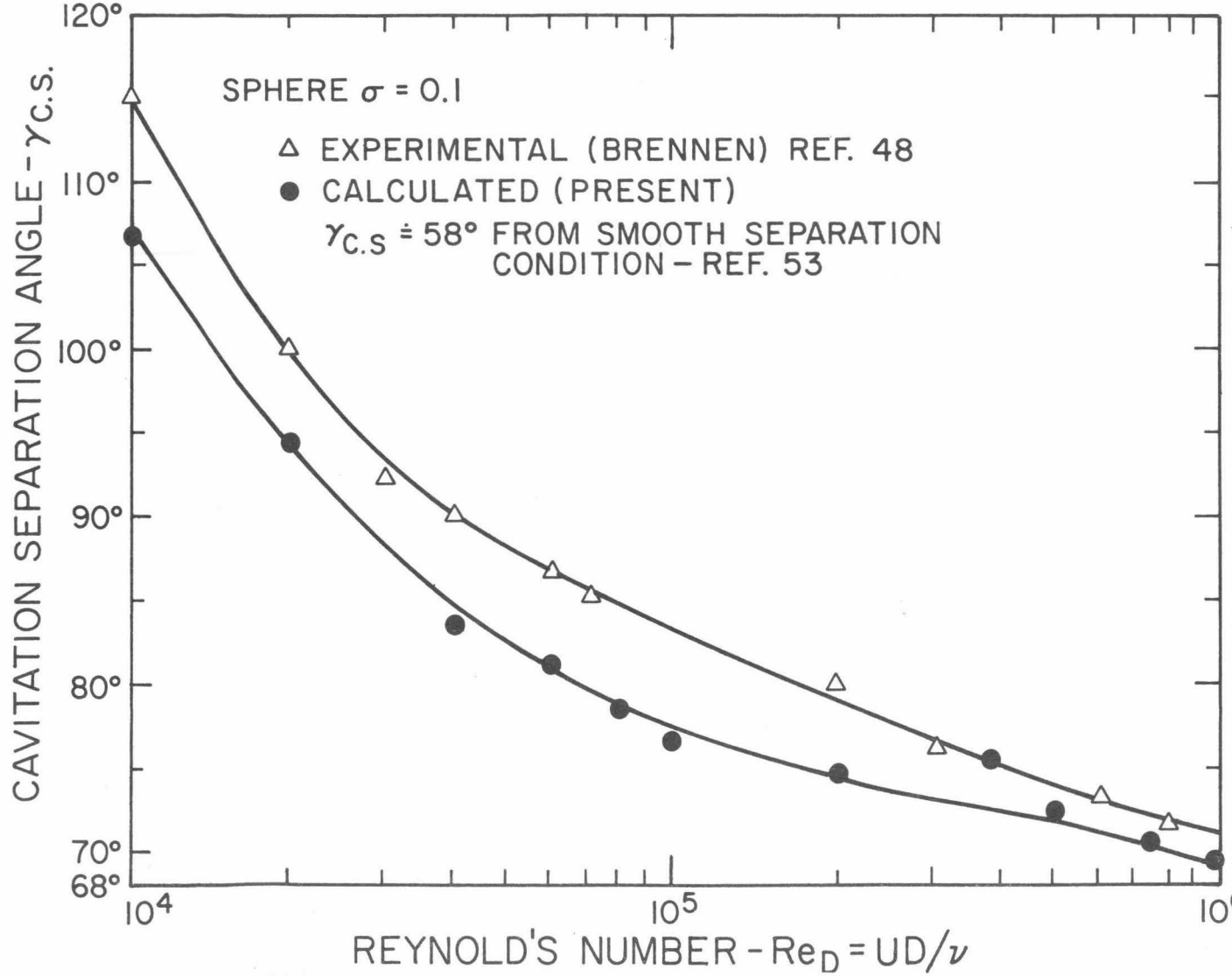

Fig.16. Comparison of presently calculated position of cavitation separation with experimentally observed position on sphere for $10^4 < Re_D < 10^6$ at $\sigma = .1$.

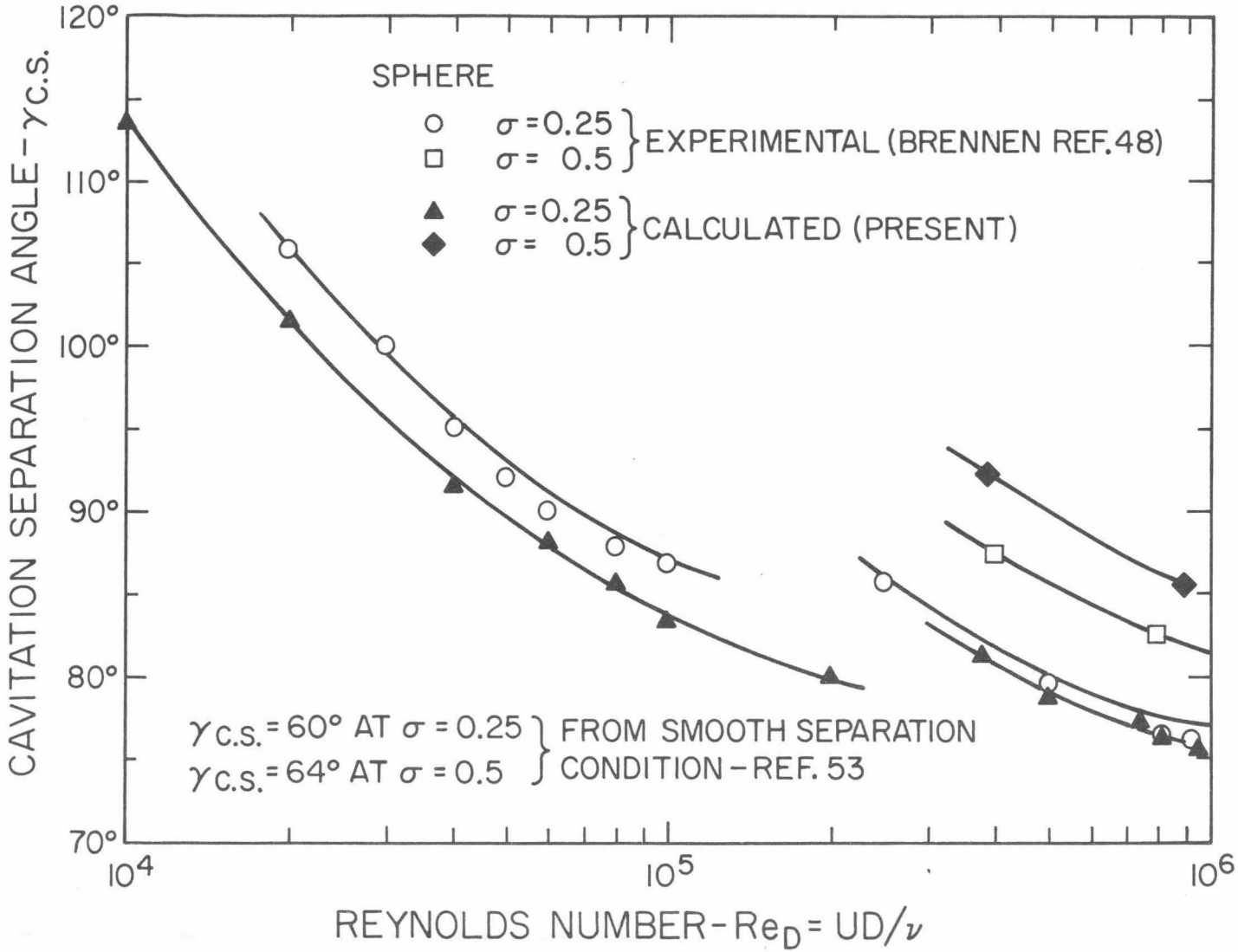

Fig.17. Comparison of presently calculated position of cavitation separation with experimentally observed position on sphere for $10^4 < Re_D < 10^6$ at $\sigma = .25$ and .5.

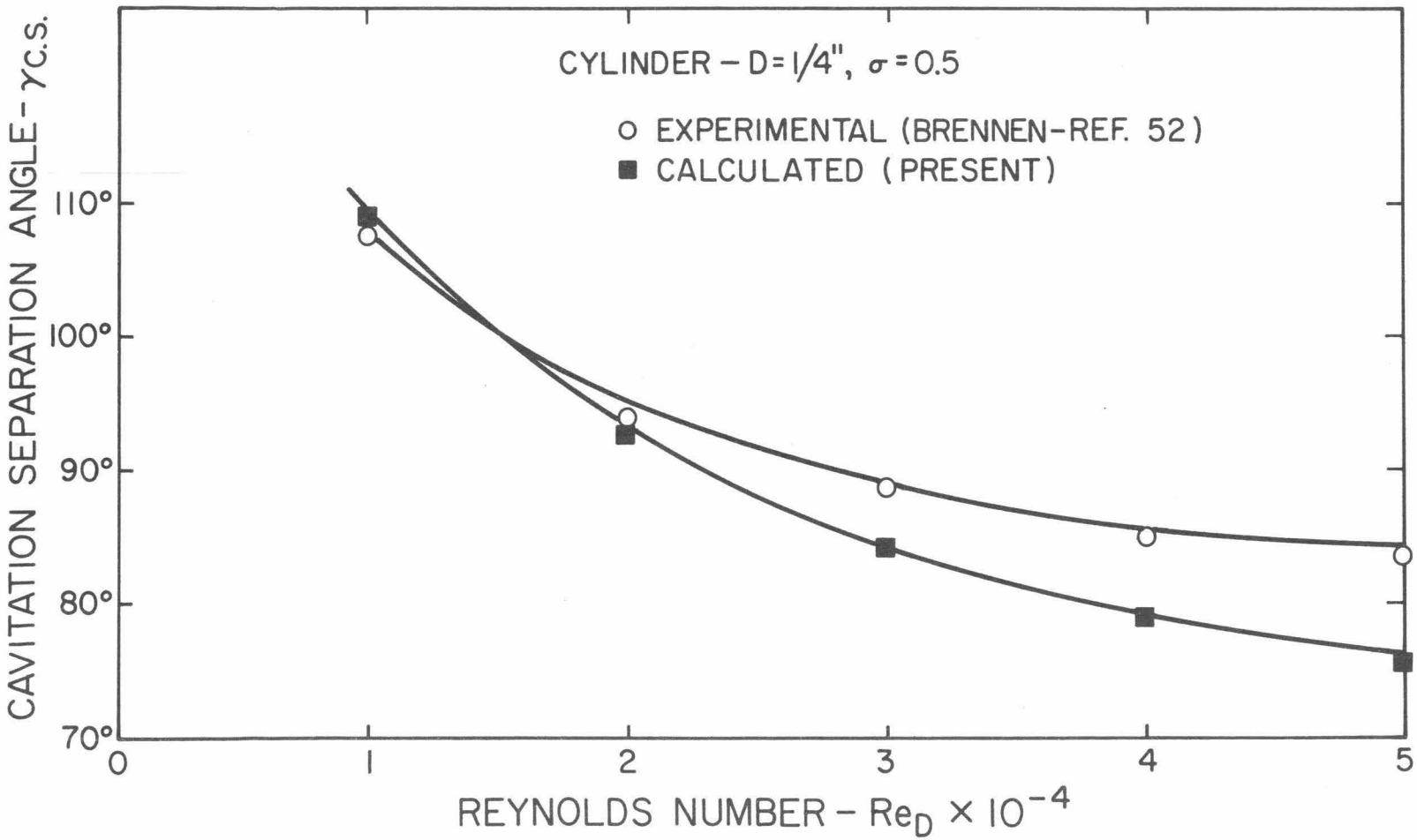

Fig.18. Comparison of presently calculated position of cavitation separation with experimentally observed position on cylinder for $10^4 < Re_D < 10^5$ at $\sigma = .5$.

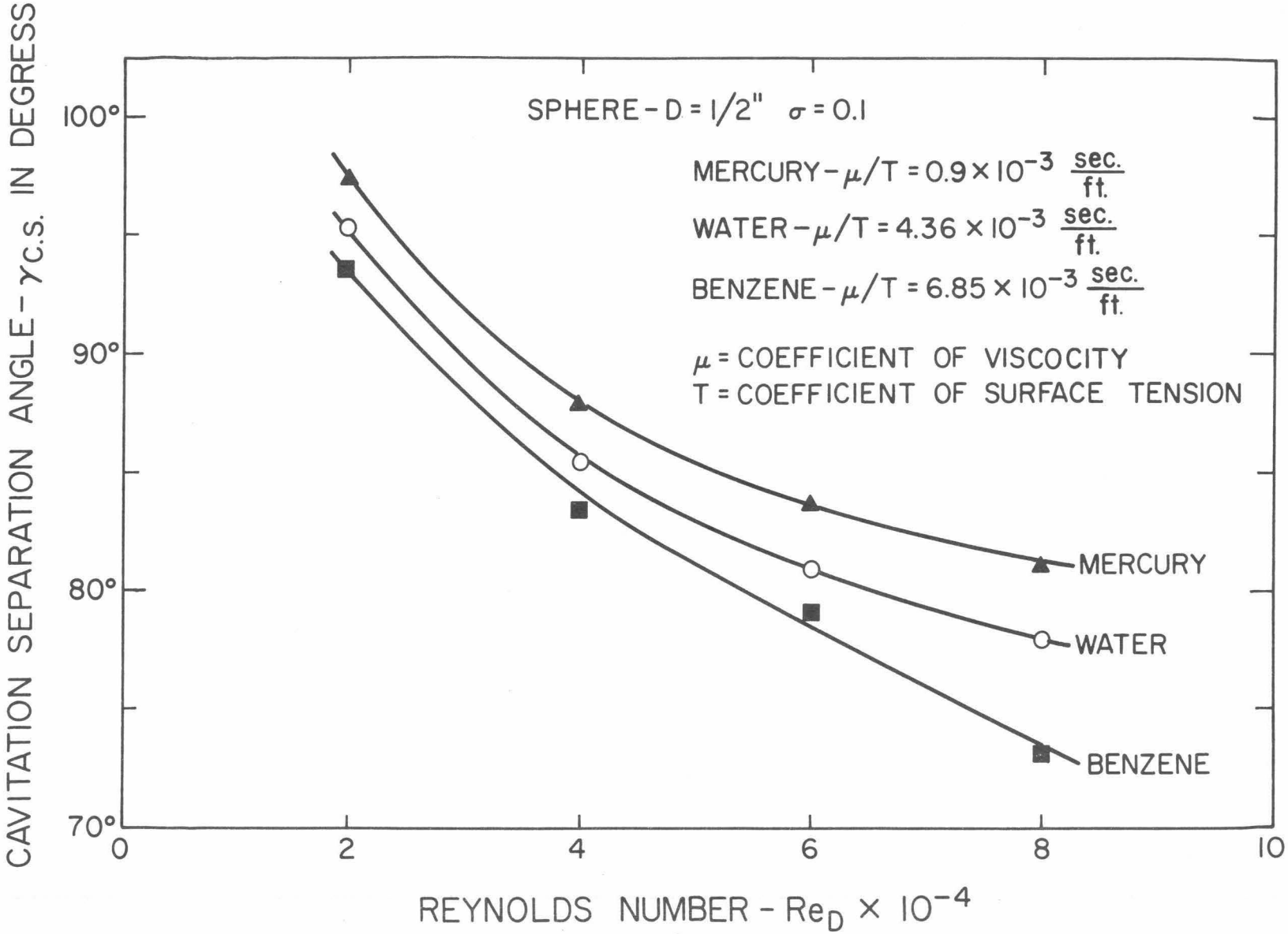

Fig.19. Comparison of calculated position of cavitation separation on sphere at $\sigma = .1$ for three different liquids with different physical properties.

APPENDIX A

LAMINAR BOUNDARY LAYER GROWTH CALCULATIONS

The laminar boundary layer growth calculations were made by using Thwaites approximate method which is detailed in Ref.(54) for two dimensional bodies and is detailed in Ref. (55) for axisymmetric bodies. Computations were made on a hemispherical nose, Swedish headform, 1.5 calibre ogive, a sphere and a cylinder.

Necessary information to use the Thwaites method is the knowledge of the pressure distribution around the headform. Presently used experimental pressure distributions obtained from different sources are shown in Figs. A.1 and A.2. It is assumed that the gross pressure distribution around the hemispherical nose, the Swedish headform and the 1.5 calibre ogive does not change with Re_D for $Re_D > 2 \times 10^5$. This assumption may be justified from the observations of Part I, that the hemispherical nose and the Swedish headform possess very small laminar separated regions for $Re_D > 2 \times 10^5$. Rouse[43] has observed that the gross pressure distribution around the hemispherical nose does not change appreciably with Re_D for $Re_D > 2 \times 10^5$.

In Thwaites method a parameter λ is defined as follows,

$$\lambda = \frac{\theta^2 U_e'}{\nu} \tag{A-1}$$

where θ is the momentum thickness, U_e' is the local velocity gradient at the edge of the boundary layer and ν is the kinematic viscosity. Then, from Thwaites approximate method,

$$\lambda = \frac{.45}{r_0^2} \frac{U_e'}{U_e^6} \int_0^s r_0^2 U_e^5 \, dx \qquad (A.2)$$

where s is the streamwise coordinate along the model surface, r_0 is the local radius as shown in Fig. A.3 and U_e is the local velocity at the edge of the boundary layer. Non-dimensionalizing velocities with U_∞ which is the velocity far away from the body and distances with diameter of the body, D, in equation (A.2) one obtains

$$\lambda = \frac{.45}{r_0^2} \left[- \left\{ d c_p / d(s/D) \right\} \cdot \frac{1}{2\sqrt{1-c_p}} \right] \cdot \frac{1}{[1-c_p]^3} \int_0^{(s/D)} r_0^2 [1-c_p]^{5/2} \, dx' \qquad (A.3)$$

Also used in equation (A.2) is the relationship $\frac{U_e}{U_\infty} = \sqrt{1-c_p}$ where c_p is the local pressure coefficient defined by $(P-P_\infty)/1/2\, \rho_L U_\infty^2$. P_∞ is the pressure far away from the body where velocity is U_∞ and ρ_L is the liquid density.

The integration of equation (A.3) was carried out by trapezoidal rule with the help of known experimental pressure distribution. Thus, once λ is determined from equation (A.3) the shape parameter, H, which is the ratio of displacement thickness to momentum thickness, δ^*/θ, may be found from page 306 of Ref. (55). The modified values of Curle and Skan were used.

Knowing λ, one may determine θ and H which provides the knowledge of δ^*. Laminar boundary layer separation is said to occur when $\lambda = -0.09$ with corresponding $H = 3.55$.

Results: Geometrical details of a hemispherical nose and Swedish headform are shown in Figs. 9 and 10 of Part I and that of 1.5 calibre ogive are shown in Fig. A.4. Comparison of the predicted position of the laminar boundary layer separation by Thwaites approximate method for several cases with that observed experimentally is shown in Table A.1. The predictions are seen to be within 7 percent of experimental observations. Variation of the momentum thickness at the predicted position of separation, θ_s, with Reynolds number for different bodies is shown in Fig. A.5.

Model	Reynolds Number-Re_D	Source of Pressure Distribution	Position of B. L. S. Thwaites' Method	Position of B. L. S. Experimental
1.5 Calibre Ogive	$Re_D > 10^5$	Ref. (43)	$(s_{B.L.S.}/D) = 1.32$	None Measured
Swedish Headform	$Re_D \cong 3 \times 10^5$	Ref. (43)	$(s_{B.L.S.}/D) = .82$	$(s_{B.L.S.}/D) = .82$ Present - Part I
Swedish Headform	$Re_D \cong 8 \times 10^5$	Ref. (43)	$(s_{B.L.S.}/D) = .82$	$(s_{B.L.S.}/D) = .84$ Present
Hemispherical Nose	$Re_D > 2 \times 10^5$	Ref. (43)	$\gamma_{B.L.S.} = 87°$	$\gamma_{B.L.S.} \cong 87°$ Present HSWT
Hemispherical Nose	$Re_D > 2 \times 10^5$	Ref. (43)	$\gamma_{B.L.S.} = 87°$	$\gamma_{B.L.S.} \cong 87°$ Present FSWT
Sphere	$10^4 < Re_D < 10^5$	Ref. (51)	$\gamma_{B.L.S.} \cong 78°$	$\gamma_{B.L.S.} \cong 82.5°$ Ref. (51)
Sphere	$Re_D \cong 2 \times 10^5$	Ref. (51)	$\gamma_{B.L.S.} \cong 78°$	$\gamma_{B.L.S.} \cong 82.5°$ Ref. (51)
Sphere	$Re_D > 3 \times 10^5$	Ref. (51)	$\gamma_{B.L.S.} = 108°$	$\gamma_{B.L.S.} = 109°$ Ref. (51)
Cylinder	$10^4 < Re_D < 5 \times 10^4$	Ref. (42)	$\gamma_{B.L.S.} = 80°$	$\gamma_{B.L.S.} = 80°$ Ref. (42)

TABLE A.1 Comparison of Calculated Positions of Boundary Layer Separation by Thwaites' Method with Experimentally Observed Positions for Various Bodies.

LIST OF FIGURE CAPTIONS - APPENDIX A

Fig. A.1. Pressure distribution on the hemispherical nose, the Swedish headform and the 1.5 calibre ogive. Taken from Refs. (4) and (43).

Fig. A.2. Pressure distribution on a sphere and a cylinder in various Reynolds number ranges. Taken from Refs. (42) and (51).

Fig. A.3. Coordinate system used for boundary layer growth calculations.

Fig. A.4. Diagram showing the geometrical details of the 1.5 calibre ogive.

Fig. A.5. Variation of calculated value of momentum thickness at separation by Thwaites' method with Reynolds number for various models.

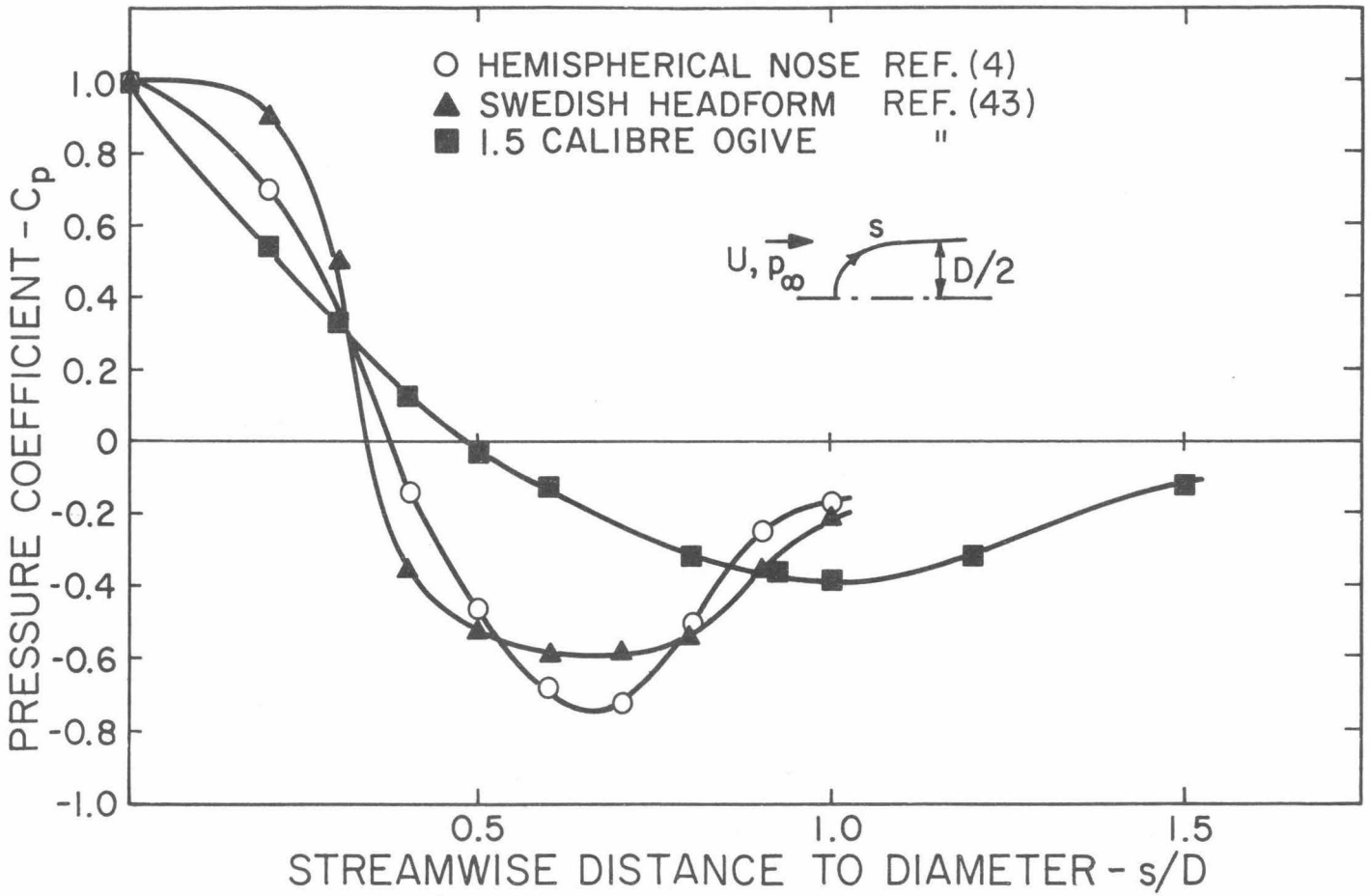

Fig. A.1. Pressure distribution on the hemispherical nose, the Swedish headform and the 1.5 calibre ogive. Taken from Ref. (4) and (43).

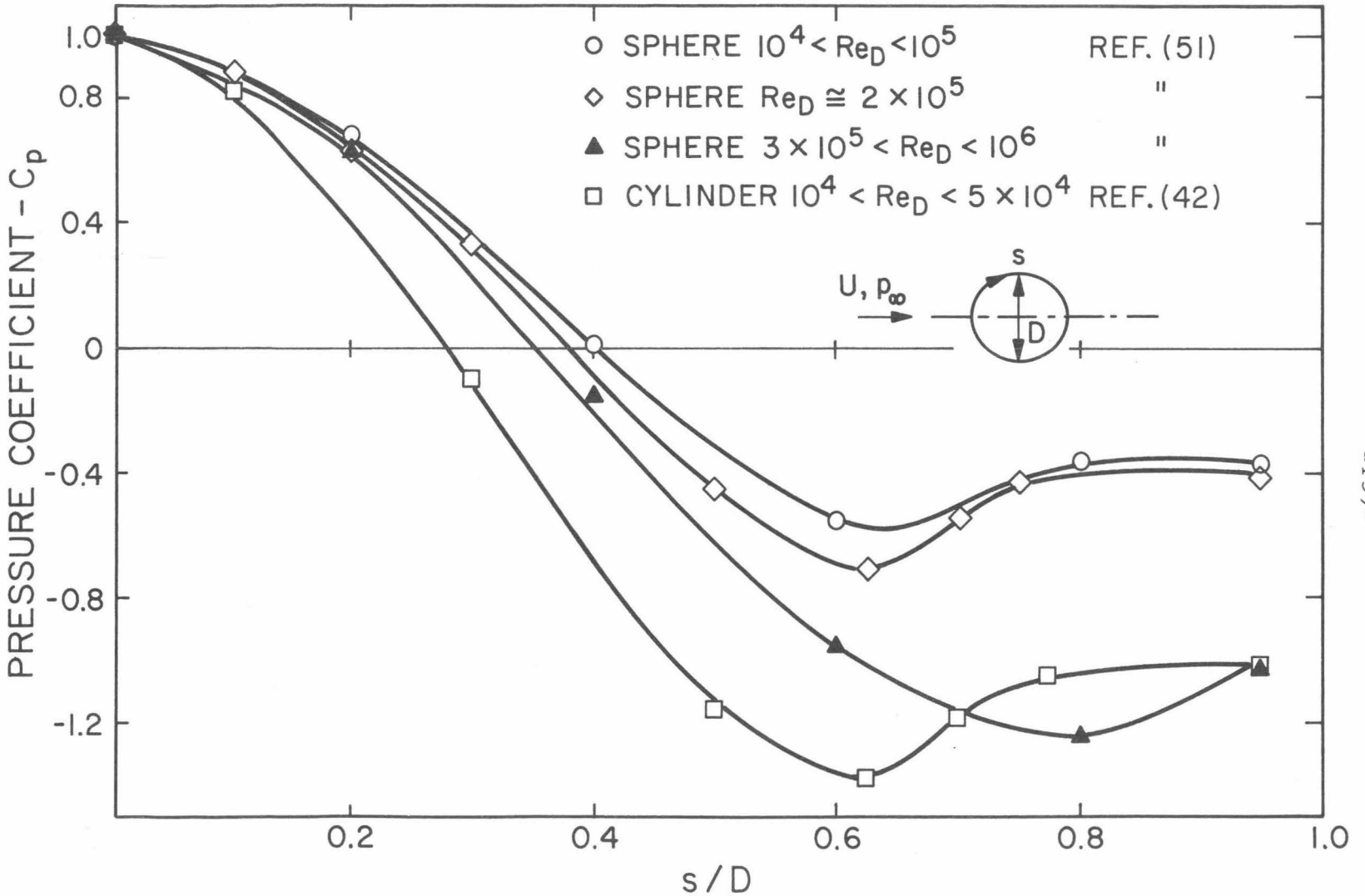

Fig.A.2. Pressure distribution on a sphere and a cylinder in various Reynolds number ranges. Taken from Refs. (42) and (51).

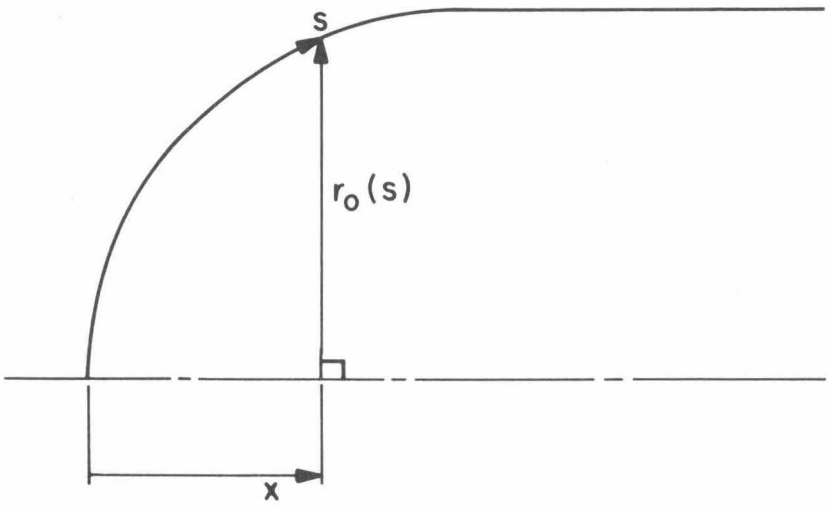

Fig. A. 3. Coordinate system used for boundary layer growth calculations.

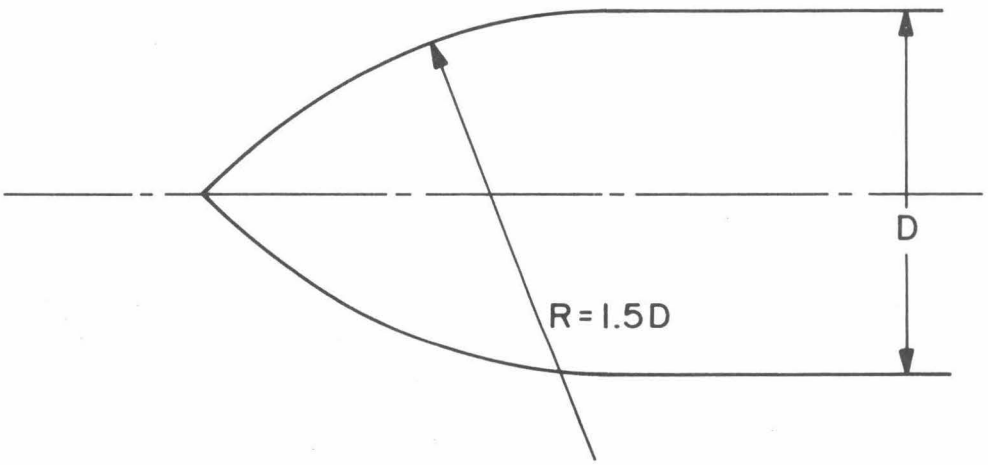

Fig. A.4. Diagram showing thegeometrical details of the 1.5 calibre ogive.

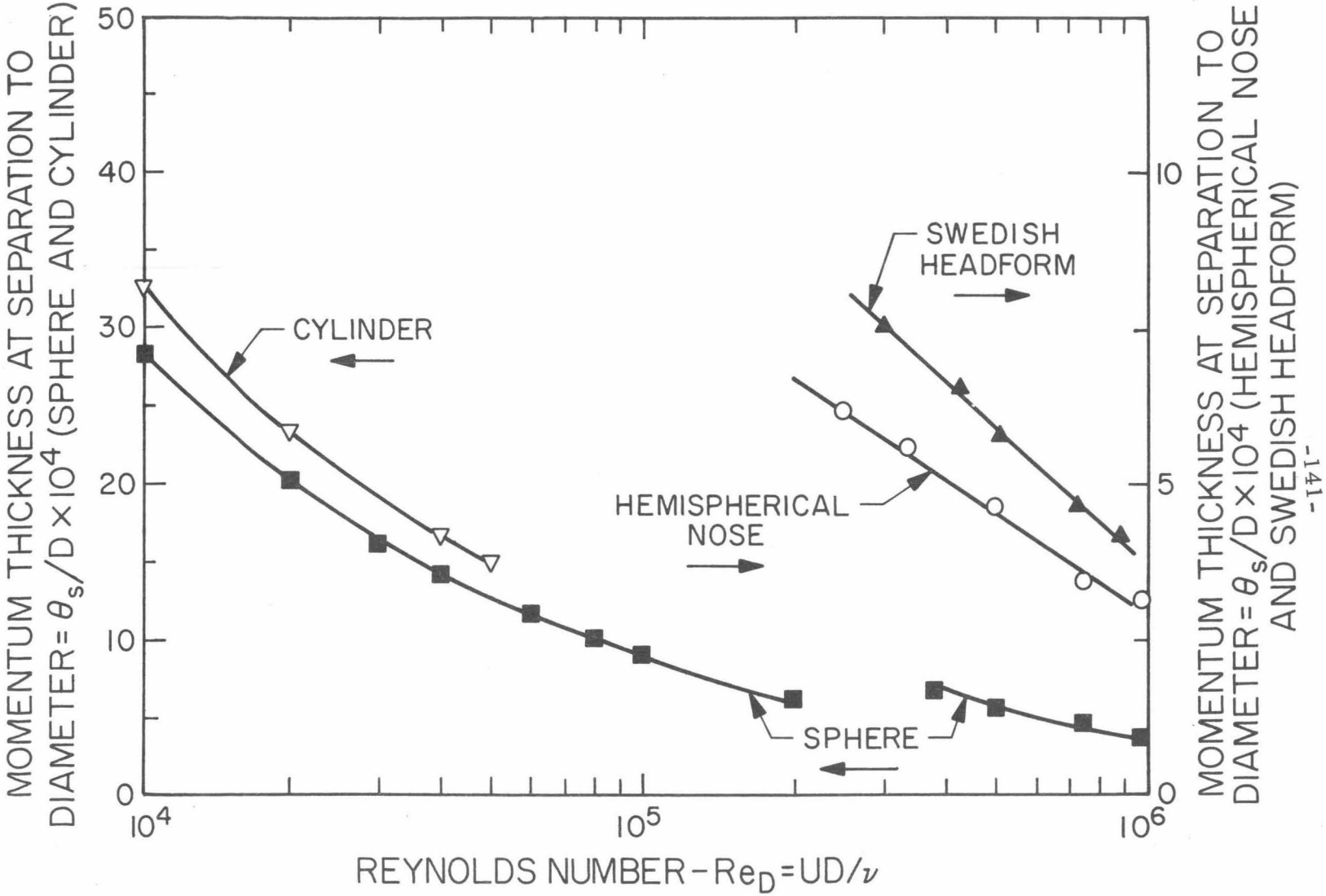

Fig. A.5. Variation of calculated value of momentum thickness at separation by Thwaites method with Reynolds number for various models.

APPENDIX B

APPROXIMATE COMPUTATIONS OF SPATIAL GROWTH OF BOUNDARY LAYER DISTURBANCES TO PREDICT TRANSITION

In Appendix B an approximate method of predicting transition of the laminar boundary layer to turbulent boundary layer using the spatial stability charts for the Falkner-Skan boundary layer profiles is presented. The stability charts have been computed by Wazzan, Okamura, and Smith and are presented in Refs. (46) and (41). An approximate method of obtaining necessary boundary layer growth information for the use of stability charts is outlined in Appendix A. Transition of boundary layer is said to occur when the amplitude of initial disturbance is magnified by a factor of e^7, which is based on the semi-empirical method of Smith (41). For axisymmetric bodies the calculated amplification factor by Smith was found to be about e^7 to e^9 at the experimental position of transition. This method has been applied for hemispherical nose, Swedish headform and 1.5 calibre ogive. The value of Reynolds number at which transition occurs at the position of laminar boundary layer separation is said to be a critical value and is designated by $Re_{D\,crit}$. Roshko (42) refers to this Reynolds number as second critical Reynolds number. It should be noted that for $Re_D < Re_{D\,crit}$ transition to turbulence occurs on the separated free shear layer and thus cannot be predicted by the present method.

In the method of Ref. (46) the stream function is assumed to be of the form

$$\Psi = \psi_0(y) + \psi(x, y, t) \tag{B. 1}$$

where ψ_0 represents the mean flow and ψ a small disturbance commonly known as Tollmein-Schlichting disturbance of the form

$$\psi = \varphi(y) e^{i\alpha(x-ct)} \tag{B. 2}$$

In the above two equations the distances are normalized by boundary layer thickness δ, velocity by U_e, velocity at the edge of the boundary layer and t by δ/U_e. Substitution of these equations in continuity and Navier-Stokes equations of motion and linearizing them in φ produces the Orr-Sommerfield equation. It should be noted that α in general is complex and imaginary part α_i is the disturbance amplification rate and the real part α_r the wave number, and c is complex of which the real part c_r is the phase speed. Since only spatial amplifications are considered the product αc is taken to be real quantity. The Orr-Sommerfield equation with proper boundary conditions is solved by numerical means. The details should be referred to in Ref. (46). The Falkner-Skan velocity profiles are obtained by numerical integration of the boundary layer equation

$$F'''(\eta) = -FF'' + \beta(F'^2 - 1) \tag{B. 3}$$

where $\eta = y/\delta$, $F'(y) = U(y)/U_e$ and prime denotes differentiation with η. It should be remembered that $\beta > 0$ represents accelerating flow, $\beta = 0$ represents flat plate solution and $\beta < 0$ represents deaccelerating flow. $\beta = -.1988$ represents separating velocity profile. Therefore solution of Eq. (B. 3) provides a value for the shape parameter $H = \delta^*/\theta$ as function of β. Tabulation of values of H for different β's is given on page 20 of Ref. (46) and are shown in Fig. B.1.

The stability charts of Ref. (46) are presented in the form of curves of constant $\alpha_i \delta^*/R_{\delta^*}$ on the diagrams of dimensionless frequency vs. Reynolds number (ω_r, R_{δ^*}). This is done for many values of β. These charts represent the eigenvalue solutions of Orr-Sommerfield equation.

If s_i is taken to be the neutral point or position from where the disturbances begin to grow, then amplification at any point s downstream of s_i in terms of tabulated quantities is given by

$$\ell n\, A(s/D) = -\int_{s_i/D}^{s/D} \left(\alpha_i \delta^*/Re_{\delta^*}\right) \cdot \frac{U_e}{U_\infty} \cdot Re_D \cdot d(s'/D) \qquad (B.4)$$

The above equation is for fixed $\omega_r = \omega^* \nu/U_e^2$.

Method of Present Computations: From Thwaites' method local value of R^*_δ H as function of s/D is calculated, corresponding to this H from Fig. B.1 a β is obtained. At this β corresponding chart in Ref. (46) gives the value of $(\alpha_i \delta^*/R_{\delta^*})$ for different value of ω_r . Local value of $\frac{U_e}{U_\infty}$ is obtained from experimental pressure distribution. Many times extrapolation of charts from Ref. (46) had to be carried out by replotting the results. Therefore the product of $(\alpha_i \delta^*/Re_{\delta^*}) \cdot \frac{U_e}{U_\infty} \cdot Re_D$ can be plotted as function of s/D. This has to be done for different values of ω_r, and among these ω_r one particular value will give the maximum amplification at the desired position. Thus ℓn (A max) may be calculated as function of position along the model surface by simple integration. Such computations for hemispherical nose are shown in Fig. B. 2; it may be seen that even at a Reynolds number of 2.2×10^6 transition has not occurred prior to

predicted boundary layer separation. The critical Reynolds for hemispherical nose was estimated to be about 5×10^6. It was seen earlier that during present experiments schlieren method showed a laminar separation bubble to exist at a Reynolds number of 9×10^5 confirming the predictions afforded in Fig. B.2. Computation of maximum amplification rates for the Swedish headform are shown in Fig. B.3. The critical Reynolds number for Swedish headform is found to be around 1.5×10^6 and from schlieren experiments a laminar separation bubble existed on the Swedish headform at a Reynolds number of 8.78×10^5. For $Re_D > 1.5 \times 10^6$ transition is predicted prior to the predicted and observed position of laminar boundary layer separation as shown in Fig. B.3. From Fig. B.4, the estimated critical Reynolds number for 1.5 calibre ogive is 6.28×10^5. Also shown in Fig. B.4 are predicted position of transition for various Re_D greater than 6.28×10^5. Once knowing the position of transition, one may estimate the magnitude of the pressure coefficient at transition, $c_{p_{tr}}$, from the experimentally measured pressure distribution. Using the results of Fig. B.4 in conjunction with pressure distribution for 1.5 calibre ogive shown in Fig. A.1 of Appendix A, variation of $-c_{p_{tr}}$ with Re_D is shown in Fig. B.5. As expected the position of transition moves forward with increas in Re_D and hence, $-c_{p_{tr}}$ may be expected to increase with increase in Re_D as observed in Fig. B.5.

A few concluding remarks should be made concerning the method outlined above. During the computations described earlier, an assumption has been made that the gross pressure distribution around the

headform does not change with Re_D for $Re_D > 2 \times 10^5$. This assumption has been justified in Appendix A. It should be noted that for axi-symmetric bodies the difference on amplification rates from that of a two dimensional body comes about only through the change of boundary layer growth properties.

LIST OF FIGURE CAPTIONS - APPENDIX B

Fig. B.1. Relationship between Hartee β-dimensionless pressure coefficient and H-shape parameter. Taken from Ref. (46).

Fig. B.2. Calculated maximum amplification factors along streamwise position of the hemispherical nose with increasing Reynolds number.

Fig. B.3. Calculated maximum amplification factors along streamwise position of the Swedish headform with increasing Reynolds number.

Fig. B.4. Calculated maximum amplification factors along streamwise position of the 1.5 calibre ogive with increasing Reynolds number.

Fig. B.5. Variation of the calculated pressure coefficient at the predicted position of transition with Reynolds number for $Re_D > Re_{D\,crit}$. The results are for the 1.5 calibre ogive.

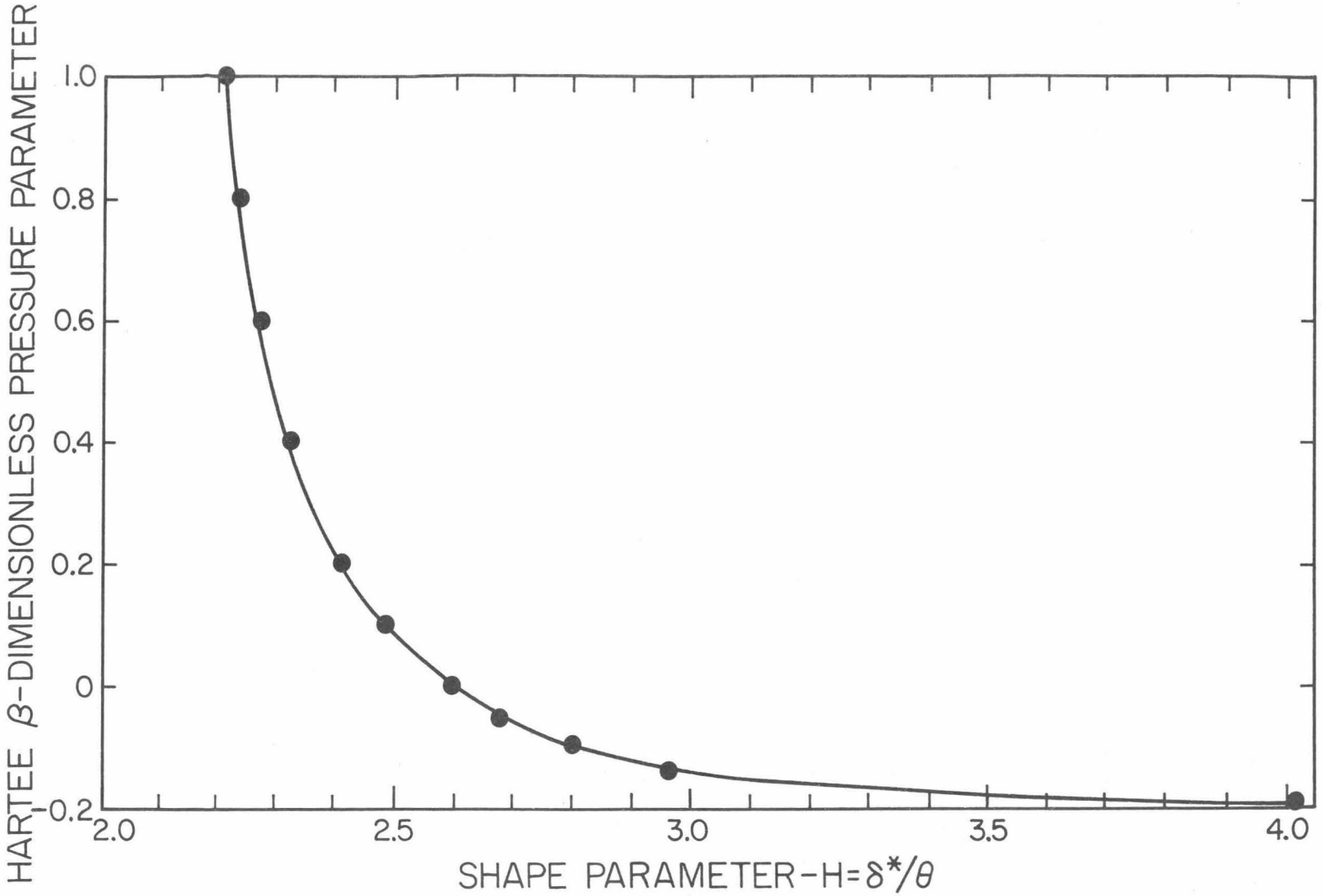

Fig. B.1. Relationship between Hartee β-dimensionless pressure coefficient and H-shape parameter. Taken from Ref. (46).

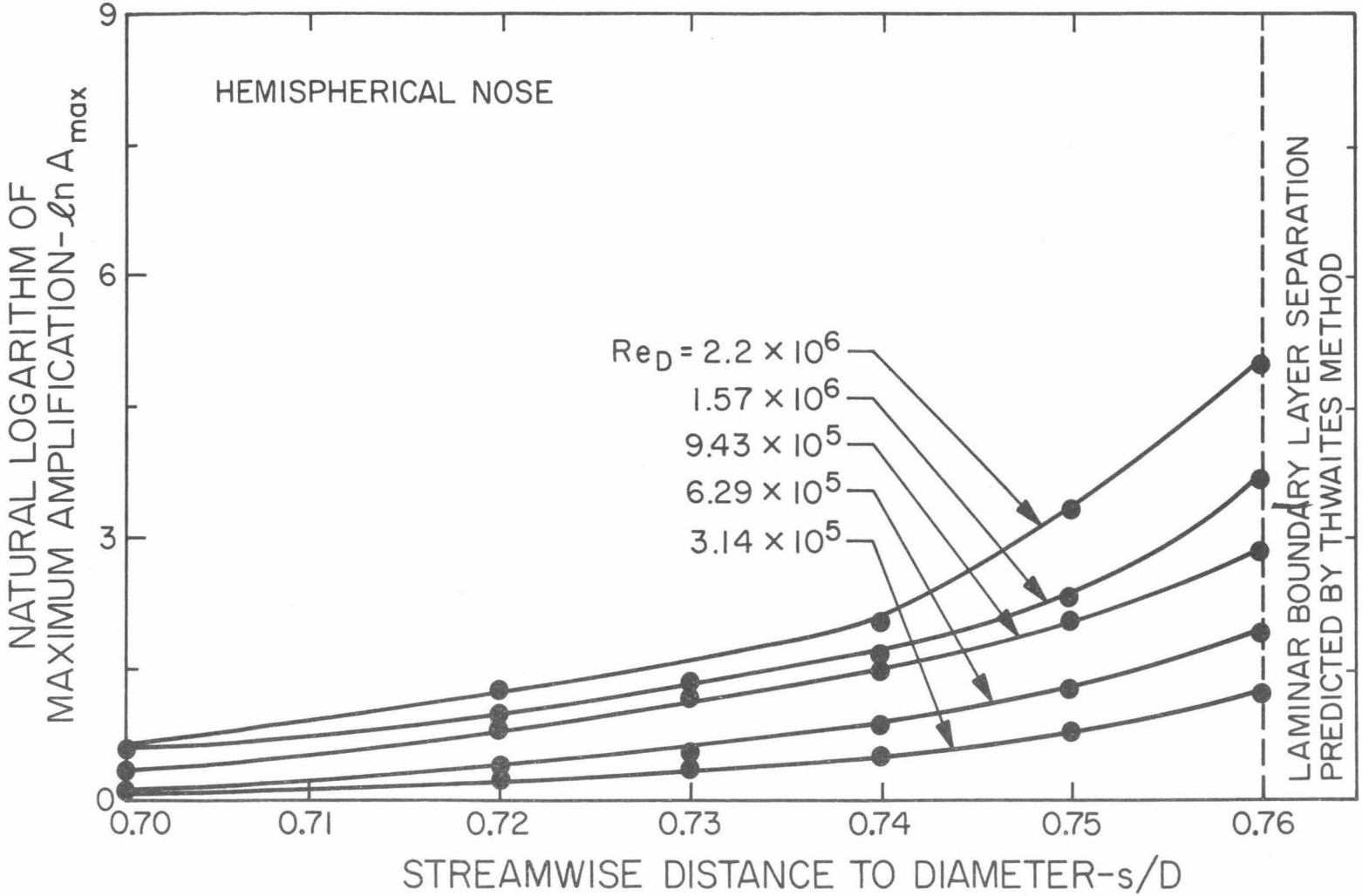

Fig. B.2. Calculated maximum amplification factors along streamwise position of the hemispherical nosewith increasing Reynolds number.

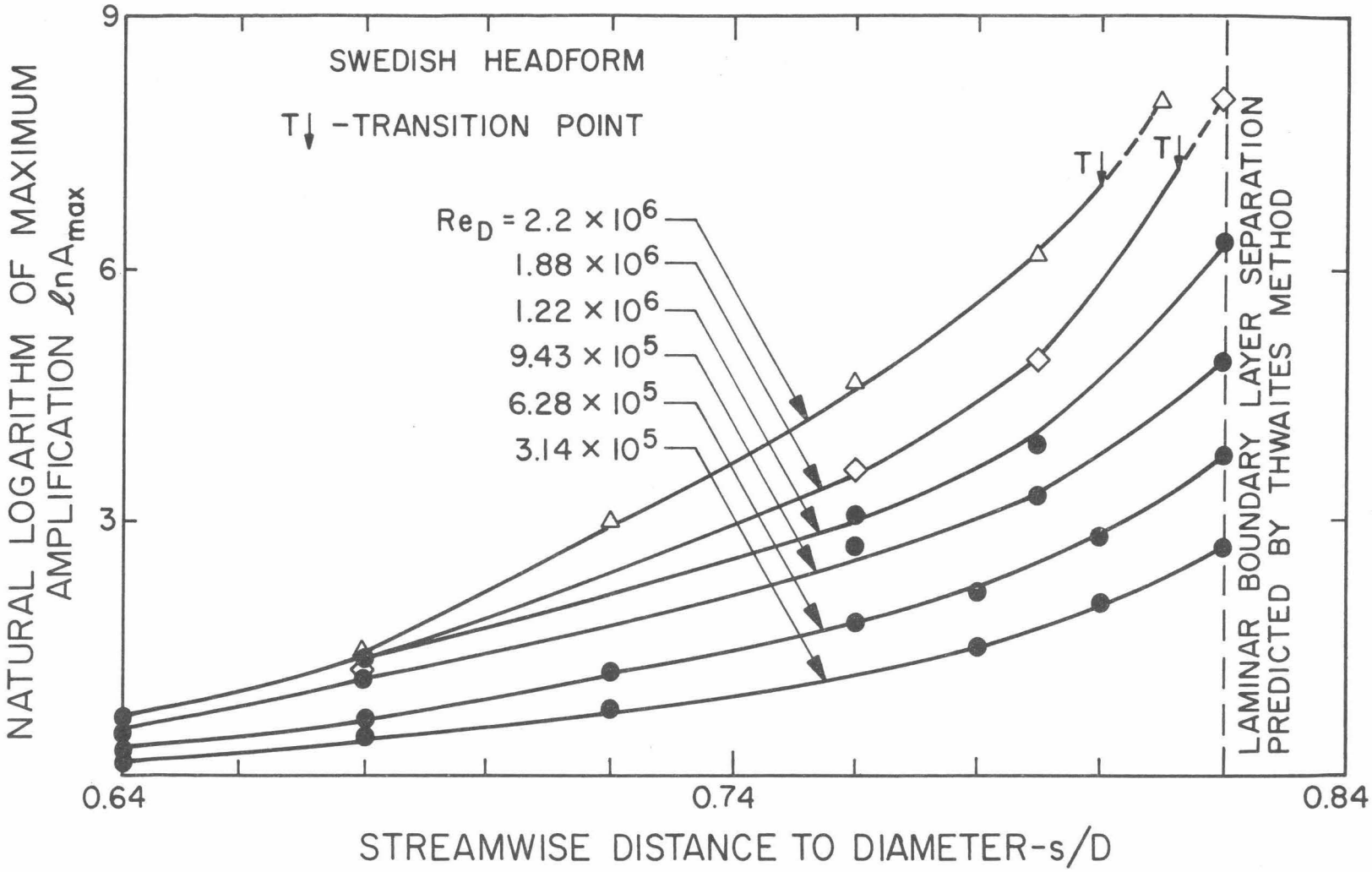

Fig. B.3. Calculated maximum amplification factors along streamwise position of the Swedish headform with increasing Reynolds number.

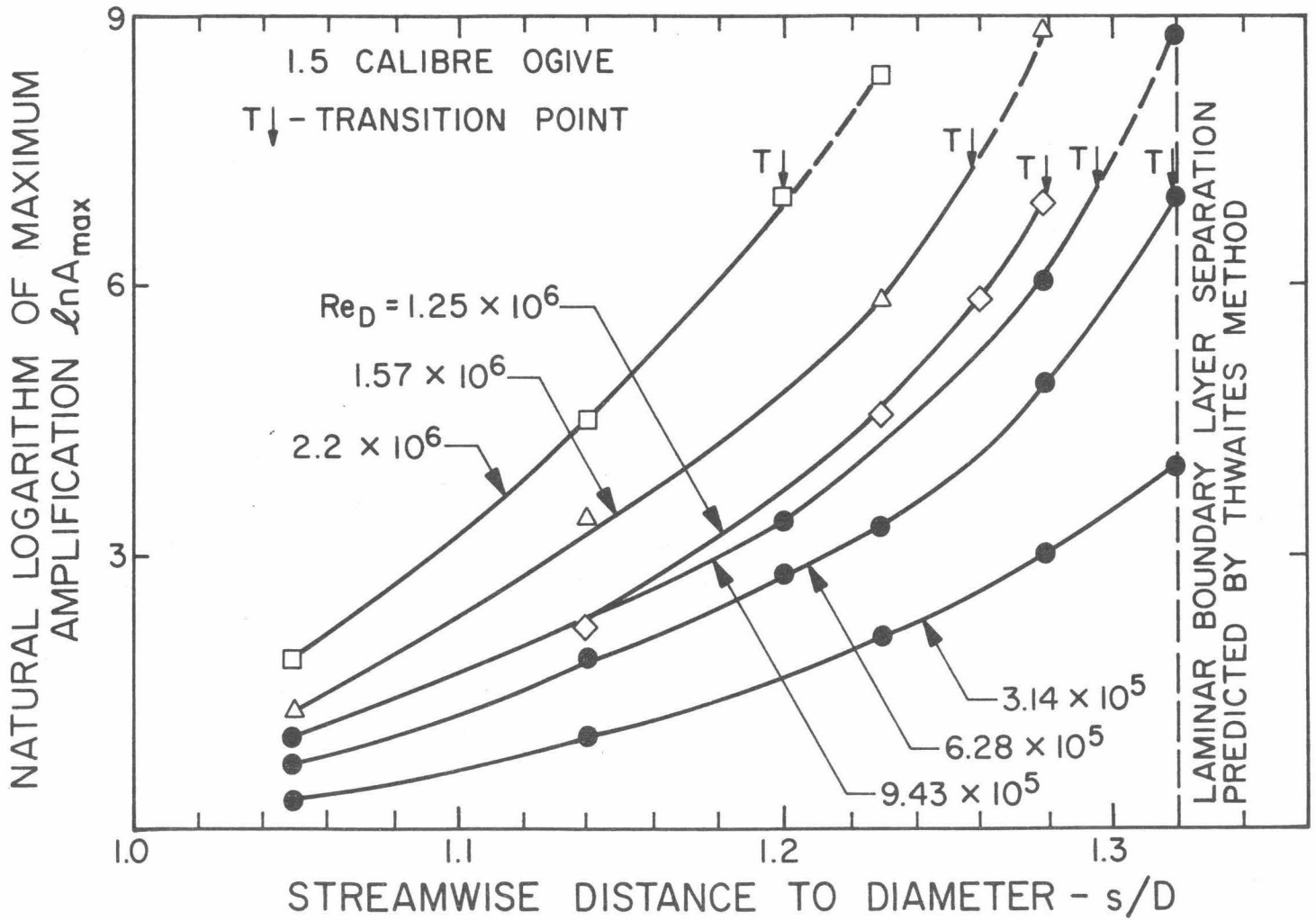

Fig. B.4. Calculated maximum amplification factors along streamwise position of the 1.5 calibre ogive with increasing Reynolds number.

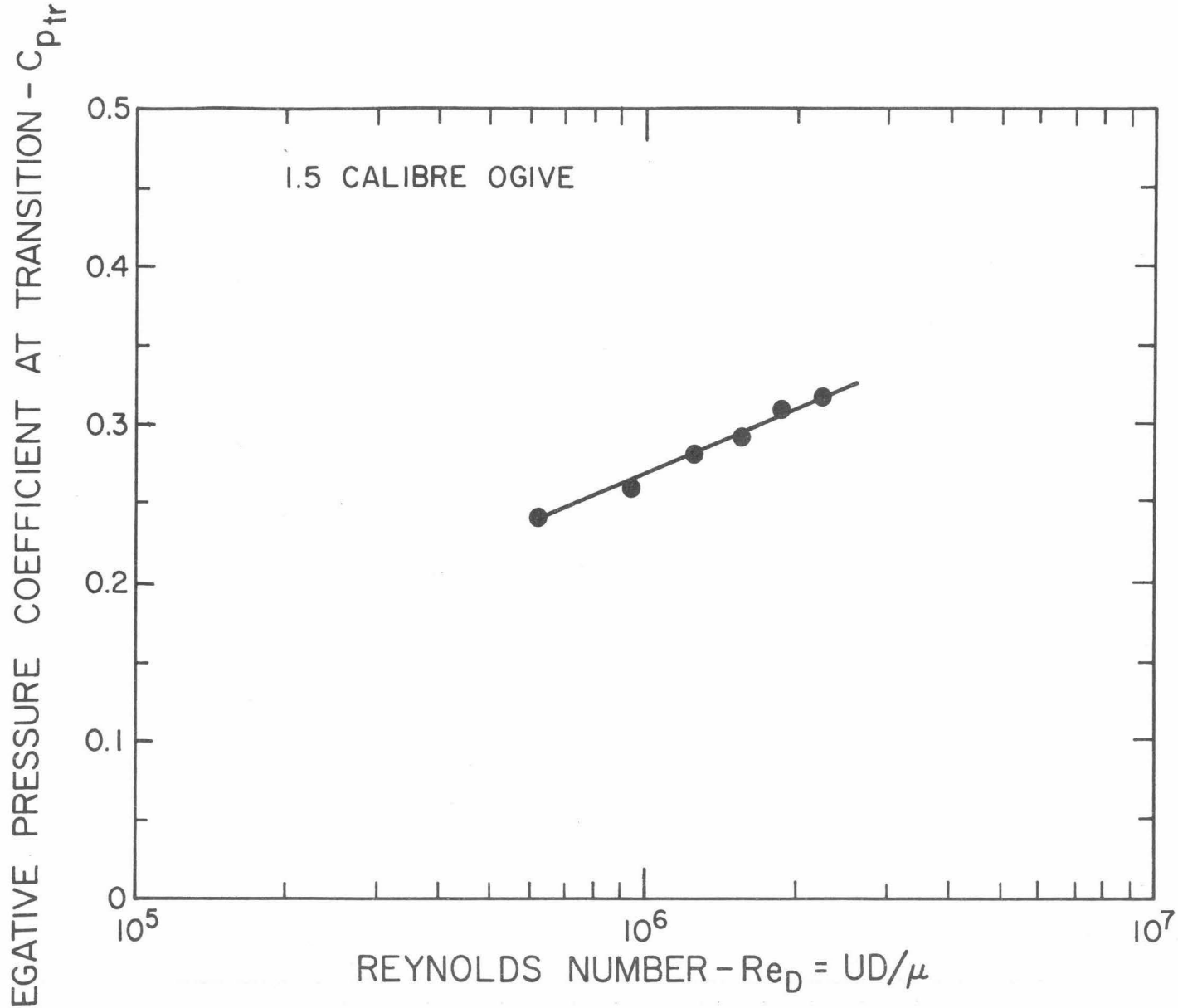

Fig.B.5. Variation of the calculated pressure coefficient at the predicted position of transition with Reynolds number for $Re_D > Re_{D\,crit}$. The results are for the 1.5 calibre ogive.

REFERENCES

1. Plesset, M. S., "Cavitation State of Knowledge", ASME, New York, p. 15, 1969.

2. Holl, J. W., "Cavitation State of Knowledge", ASME, New York, p. 26, 1969.

3. Knapp, R. T., Daily, J. W., and Hammitt, F. G., "Cavitation", McGraw-Hill, 1970.

4. Kermeen, R. W., "Some Observations of Cavitation on Hemispherical Head Models", California Institute of Technology, Hydrodynamics Laboratory Report,No. E-35.1, June 1952.

5. Parkin, B. R. and Holl, J. W., "Incipient-Cavitation Scaling Experiments for Hemispherical and 1.5 Calibre Ogive-Nosed Bodies", Report Nord 7958-264, Ordnance Research Laboratory, Pennsylvania State University, February 1956.

6. Arakeri, V. H., "Water Tunnel Investigations of Scale Effects in Cavitation Detachment from Smooth Slender Bodies and Characteristics of Flow Past a Bi-Convex Hydrofoil", California Institute of Technology, Hydrodynamics Laboratory Report No. E-79A.12, January 1971.

7. Lindgren, H. and Johnsson, C. A., "Cavitation Inception on Head Forms ITTC Comparitive Experiments", Publications of the Swedish State Shipbuilding Experimental Tank, no. 58, 1966. (Also presented at the Eleventh ITTC Meeting in Tokyo, 1966)

8. Knapp, R. T. and Hollander, A., "Laboratory Investigations of the Mechanism of Cavitation", Transactions ASME, vol. 70, pp. 419-435, 1948.

9. Acosta, A. J. and Hamaguchi, H., "Cavitation Inception on the I. T. T. C. Standard Head Form", California Institute of Technology, Hydrodynamics Laboratory Report No. E-149.1, March 1967.

10. Harvey, E. N., Barnes, D. K., McElroy, W. D., Whiteley, A. H., Pease, D. C., and Cooper, K. W., "Bubble Formation in Animals: I. Physical Factors", Journal of Cellular and Comparative Physiology, vol. 24, no. 1, August 1944.

11. Harvey, E. N., Whiteley, A. H., McElroy, W. D., Pease, D. C., and Barnes, D. K., "Bubble Formation in Animals: II. Gas Nuclei and Their Distribution in Blood and Tissues", Journal of Cellular and Comparitive Physiology, vol. 24, no. 1, August 1944.

12. Harvey, E. N., McElroy, W. D., and Whiteley, A. H., "On Cavity Formation in Water", Journal of Applied Physics, vol. 18, February 1947.

13. Pease, D. C. and Blinks, L. R., "Cavitation from Solid Surfaces in the Absence of Gas Nuclei", Journal of Physiology and Colloidal Chemistry, vol. 51, pp. 556-567, 1947.

14. Strasberg, M., "The Influence of Air-Filled Nuclei on Cavitation Inception", DTMB, Hydromechanics Laboratory Report No. 1078, May 1957.

15. Epstein, P. S. and Plesset, M. S., "On the Stability of Gas Bubbles in Liquid-Gas Solution", Journal of Chemical Physics, vol. 18, p. 1505, November 1950.

16. Holl, J. W. and Treaster, A. L., "Cavitation Hysteresis", Journal of Basic Engineering, Trans. ASME, Series D, vol. 81, no. 1, pp. 199-212, March 1966.

17. Reed, R. L., "The Influence of Surface Characteristics and Pressure History on the Inception of Cavitation", MS Dissertation, Department of Aerospace Engineering, Pennsylvania State University, March 1969.

18. Gupta, S. K., "The Influence of Porosity and Contact Angle on Incipient and Desinent Cavitation", MS Dissertation, Department of Aerospace Engineering, Pennsylvania State University, December 1969.

19. Peterson, F. B., "Cavitation Originating at Liquid-Solid Interfaces", Report 2799, Naval Ship Research and Development Center, September 1968.

20. Ripken, J. F. and Killen, J. M., "Gas Bubbles: Their Occurrence, Measurement, and Influence in Cavitation Testing", Proceedings of IAHR-Symposium, Sendai, Japan, pp. 37-57, 1962.

21. Schiebe, F. R., "The Influence of Gas Nuclei Size Distribution on Transient Cavitation Near Inception", University of Minnesota, St. Anthony Falls Hydraulic Laboratory, Project Report No. 107, May 1969.

22. Parkin, B. R. and Kermeen, R. W., "Incipient Cavitation and Boundary Layer Interaction on a Streamlined Body", California Institute of Technology, Hydrodynamics Laboratory Report No. E-35.2, December 1953.

23. Plesset, M. S., "The Dynamics of Cavitation Bubbles", Journal of Applied Mechanics, vol. 16, pp. 277-338, September 1949.

24. Parkin, B. R., "Scale Effects in Cavitating Flow", Ph. D. Dissertation, California Institute of Technology, 1952.

25. Holl, J. W. and Kornhauser, A. L., "Thermodynamic Effects on Desinent Cavitation on Hemispherical Nosed Bodies in Water of Temperatures from 80 Degrees F to 260 Degrees F", presented at Joint Conference of Applied Mechanics and Fluids Engineering Divisions, ASME, Northwestern University, June 1969. ASME Paper No. 69-FE-1.

26. Van der Walle, F., "On the Growth of Nuclei and the Related Scaling Factors in Cavitation Inception", Fourth Symposium on Naval Hydrodynamics, August 27 - 31, 1962 (sponsored by ONR).

27. Oshima, R., "Theory of Scale Effects on Cavitation Inception on Axially Symmetric Bodies", Journal of Basic Engineering, Trans. ASME, Series D, no. 3, vol. 83, pp. 379-398, September 1961.

28. Johnson, V. E. and Hsieh, T., "The Influence of the Trajectories of Gas Nuclei on Cavitation Inception", Sixth Symposium on Naval Hydrodynamics, September 1966, (sponsored by ONR).

29. Kermeen, R. W. and Parkin, B. R., "Incipient Cavitation and Wake Flow Behind Sharp-Edged Disks", California Institute of Technology, Hydrodynamics Laboratory Report No. E-85.4, 1957.

30. Johnson, V. E., "Report to the Fourteenth American Towing Tank Conference on Cavitation", Glen Cove, New York, September 9-11, 1965.

31. Daily, J. W. and Johnson, V. E., "Turbulence and Boundary Layer Effects on Cavitation Inception from Gas Nuclei", Trans. ASME, vol. 78, pp. 1695-1706, 1956.

32. Rouse, H., "Jet Diffusion and Cavitation", Journal of the Boston Society of Civil Engineers, vol. 53, no. 3, pp. 254-271, July 1966.

33. Arndt, R. E. A. and Ippen, A. T., "Cavitation State of Knowledge ASME, New York, p. 64, 1969.

34. Bailey, A.B., "The relationship between flow separation and cavitation", Oxford University, Department of Engineering Science Report No. 1111/70.

35. Arakeri, V. H., "Water Tunnel Observations of Laminar Boundary Layer Separation Using Schlieren Technique", Polyphase Flow Forum, ASME, New York, 1972.

36. Knapp, R. T., Levy, J., O'Neill, J. P. and Brown, F. B., "The Hydrodynamics Laboratory of the California Institute of Technology", Trans. ASME, vol. 20, pp. 437-457, 1948.

37. Liepmann, H. W. and Roshko, A., "Elements of Gas Dynamics", John Wiley and Sons, Inc., pp. 153-168, 1957.

38. Bland, R. E. and Pelick, T. J., "The Schlieren Method Applied to Flow Visualization in a Water Tunnel", Journal of Basic Engineering, Trans. ASME, vol. 84, pp. 587-592, 1962.

39. Hoyt, J. W., "Wall Effect on ITTC Standard Head Shape Pressure Coefficients", Eleventh ITTC Formal Contribution, April 1966.

40. Gaster, M., "The Structure and Behaviour of Laminar Separation Bubbles", NPL, Aero Report 1181 (Revised), March 1967. (Also available as British R. and M. Report No. 3595.)

41. Jaffe, N. A., Okamura, T. T., and Smith, A. M. O., "Determination of Spatial Amplification Factors and Their Application to Predicting Transition", AIAA Journal, vol. 8, no. 2, pp. 301-308, February 1970.

42. Roshko, A., "Experiments on a Cylinder at High Reynolds Numbers", Journal of Fluid Mechanics, vol. 10, p. 345, 1961.

43. Rouse, H. and McNown, J. S., "Cavitation and Pressure Distribution Head Forms at Zero Angle of Yaw", State University of Iowa, Studies in Engineering Bulletin 32, 1948.

44. Parkin, B. R. and Kermeen, R. W., "The Roles of Convective Air Diffusion and Liquid Tensile Stresses", Proceedings of IAHR-Symposium, Sendai, Japan, pp. 17-35, 1962.

45. Plesset, M. S., "Bubble Dynamics", Proceedings of the Symposium on Cavitation in Real Liquids, Edited by R. Davies, Elsevier Publishing Company, pp. 1-17, 1964.

46. Wazzan, A. R., Okamura, T. T., and Smith, A. M. O., "Spatial and Temporal Stability Charts for the Falkner-Skan Boundary Layer Profiles", DAC 67086, McDonnell Douglas Corp., Sept. 1, 1968.

47. Wu, T. Y., "Inviscid Cavity and Wake Flows", in Basic Developments in Fluid Dynamics, Edited by M. Holt, Academic Press, pp. 42-44, 1968.

48. Brennen, C., "Cavitation State of Knowledge", ASME, New York, p. 141, 1969.

49. Taylor, G. I., "Cavitation in Hydrodynamic Lubrication", Proceedings of the Symposium on Cavitation in Real Liquids, Edited by R. Davies, Elsevier Publishing Company, pp. 80-101, 1964.

50. Pearson, J. R. A., "The Instability of Uniform Viscous Flow Under Rollers and Spreaders", JFM, vol. 7, pp. 481-500, 1960.

51. Maxworthy, T., "Experiments on the Flow Around a Sphere at High Reynolds Numbers", ASME, Journal of Applied Mechanics Paper No. 69-APMW-26.

52. Brennen, C., "Some Cavitation Experiments with Dilute Polymer Solutions", JFM, vol. 44, pp. 51-63, 1970.

53. Brennen, C., "A Numerical Solution of Axisymmetric Cavity Flows", JFM, vol. 37, p. 671, 1969.

54. Thwaites, B., "Approximate Calculation of the Laminar Boundary Layer", Aeronautical Quarterly, 1, pp. 245-280, 1949.

55. Crabtree, L. F., Küchemann, D., and Sowerby, L., "Three-Dimensional Boundary Layers", in Laminar Boundary Layers, Edited by L. Rosenhead, pp. 430-432, 1963.

DISTRIBUTION LIST FOR REPORTS
PREPARED UNDER THE
GENERAL HYDROMECHANICS RESEARCH PROGRAM

Commander
Naval Ship Research and
Development Center
Bethesda, Maryland 20034
Attn: Code 1505
Code 5614 (39)

Officer-in-Charge
Annapolis Laboratory
Naval Ship Research and
Development Center
Annapolis, Maryland 21402
Attn: Code 5642 (Library)

Commander
Naval Ship Systems Command
Washington, D. C. 20360
Attn: Ships 2052 (3)
Ships 03412B
Ships 0372
Ships 0342

Director
Defense Documentation Center
5010 Duke Street
Alexandria, Virginia 22314 (12)*

Office of Naval Research
800 N. Quincy Street
Arlington, Virginia 22217
Attn: Mr. R. D. Cooper (Code 438)

Office of Naval Research
Branch Office
492 Summer Street
Boston, Massachusetts 02210

Office of Naval Research
Branch Office (493)
536 S. Clark Street
Chicago, Illinois 60605

Chief Scientist
Office of Naval Research
Branch Office
1030 E. Green Street
Pasadena, California 91106

Office of Naval Research
Resident Representative
207 West 24th Street
New York, New York 10011

Office of Naval Research
Resident Representative
50 Fell Street
San Francisco, California 94102

Director
Naval Research Laboratory
Washington, D. C. 20390
Attn: Code 2027
Code 2629 (ONRL)

Commander
Naval Facilities Engineering
Command (Code 032C)
Washington, D. C. 20390

Library of Congress
Science & Technology Division
Washington, D. C. 20540

* The DDC Form 50, "DDC Accession Notice: must be forwarded with 12 copies of the report to the Defense Documentation Center.

Commander
Naval Ordnance Systems
Command (ORD 035)
Washington, D. C. 20360

Commander
Naval Electronics Laboratory
Center (Library)
San Diego, California 92152

Commander
Naval Ship Engineering Center
Center Building
Prince Georges Center
Hyattsville, Maryland 20782
Attn: SEC 6034B
SEC 6110
SEC 6114H
SEC 6120
SEC 6136
SEC 6144G
SEC 6140B
SEC 6148

Naval Ship Engineering Center
Norfolk Division
Small Craft Engr Dept
Norfolk, Virginia 23511
Attn: D. Blount (6660.03)

Library (Code 1640)
Naval Oceanographic Office
Washington, D. C. 20390

Technical Library
Naval Proving Ground
Dehlgren, Virginia 22448

Commander (ADL)
Naval Air Development Center
Warminster, Pennsylvania 18974

Commanding Officer (L31)
Naval Civil Engineering Laboratory
Port Hueneme, California 93043

Commander
Naval Undersea Center
San Diego, California 92132
Attn: Dr. A. Fabula (6005)

Officer-in-Charge
Naval Undersea Center
Pasadena, California 91107
Attn: Dr. J. Hoyt (2501)
Library (13111)

Director
Naval Research Laboratory
Underwater Sound Reference Division
P. O. Box 8337
Orlando, Florida 32806

Library
Naval Underwater Systems Center
Newport, Rhode Island 02840

Research Center Library
Waterways Experiment Station
Corp of Engineers
P. O. Box 631
Vicksburg, Mississippi 39180

National Bureau of Standards
Washington, D. C. 20234
Attn: P. Klebanoff (FM 105)
Fluid Mechanics (2)
Hydraulic Section

AFOSR/NAM
1400 Wilson Blvd
Arlington, Virginia 22209

AFFOL/FYS (J. Olsen)
Wright Patterson AFB
Dayton, Ohio 45433

Dept of Transportation
Library TAD-491.1
400 - 7th Street S.W.
Washington, D. C. 20590

Boston Naval Shipyard
Planning Dept Bldg 39
Technical Library, Code 202.2
Boston, Massachusetts 02129

Charleston Naval Shipyard
Technical Library
Naval Base
Charleston, South Carolina 29408

Norfolk Naval Shipyard
Technical Library
Portsmouth, Virginia 23709

Philadelphia Naval Shipyard
Philadelphia, Pennsylvania 19112
Attn: Code 240

Portsmouth Naval Shipyard
Technical Library
Portsmouth, N. H. 03801

Puget Sound Naval Shipyard
Engineering Library
Bremerton, Washington 98314

Long Beach Naval Shipyard
Technical Library (246L)
Long Beach, California 90801

Hunters Point Naval Shipyard
Technical Library (Code 202.3)
San Francisco, California 94135

Pearl Harbor Naval Shipyard
Code 202.32
Box 400, FPO
San Francisco, California 96610

Mare Island Naval Shipyard
Shipyard Technical Library
Code 202.3
Vallejo, California 94592

Assistant Chief Design Engineer
for Naval Architecture (Code 250)
Mare Island Naval Shipyard
Vallejo, California 94592

U. S. Naval Academy
Annapolis, Maryland 21402
Attn: Technical Library
Dr. Bruce Johnson
Prof. P. Van Mater, Jr.

Naval Postgraduate School
Monterey, California 93940
Attn: Library, Code 2124
Dr. T. Sarpkaya
Prof. J. Miller

Capt L. S. McCready, USMS
Director, National Maritime
Research Center
U. S. Merchant Marine Academy
Kings Point, L.I., N.Y. 11204

U. S. Merchant Marine Academy
Kings Point, L.I., N.Y. 11204
Attn: Academy Library

Library
The Pennsylvania State University
Ordnance Research Laboratory
P. O. Box 30
State College, Pennsylvania 16801

Bolt, Beranek & Newman
1501 Wilson Blvd
Arlington, Virginia 22209
Attn: Dr. F. Jackson

Bolt, Beranek & Newman
50 Moulton Street
Cambridge, Massachusetts 02138
Attn: Library

Bethlehem Steel Corporation
Center Technical Division
Sparrows Point Yard
Sparrows Point, Maryland 21219

Bethlehem Steel Corporation
25 Broadway
New York, New York 10004
Attn: Library (Shipbuilding)

Cambridge Acoustical Associates, Inc.
1033 Mass Avenue
Cambridge, Massachusetts 02138
Attn: Dr. M. Junger

Cornell Aeronautical Laboratory
Aerodynamic Research Dept
P. O. Box 235
Buffalo, New York 14221
Attn: Dr. A. Ritter

Eastern Research Group
P. O. Box 222
Church Street Station
New York, New York 10008

Esso International
Design Division, Tanker Dept
15 West 51st Street
New York, New York 10019

Mr. V. Boatwright, Jr.
R & D Manager
Electric Boat Division
General Dynamics Corporation
Groton, Conn 06340

Gibbs & Cox, Inc.
21 West Street
New York, New York 10006
Attn: Technical Info. Control

Hydronautics, Inc.
Pindell School Road
Howard County
Laurel, Maryland 20810
Attn: Library

McDonnell Douglas Aircraft Co.
3855 Lakewood Blvd
Long Beach, California 90801
Attn: J. Hess
A.M.O. Smith

Lockheed Missiles & Space Co.
P. O. Box 504
Sunnyvale, California 94088
Attn: Mr. R. L. Waid, Dept 57-74
Bldg 150, Facility 1

Newport News Shipbuilding &
Dry Dock Company
4101 Washington Avenue
Newport News, Virginia 23607
Attn: Technical Library Dept

North American Aviation, Inc.
Space & Information Systems Div
12214 Lakewood Blvd
Downey, California 90241
Attn: Mr. Ben Ujihara (SL-20)

Nielsen Engineering & Research, Inc.
850 Maude Avenue
Mountain View, California 94040
Attn: Mr. S. B. Spangler

Oceanics, Inc.
Technical Industrial Park
Plainview, L.I., N.Y. 11803

Society of Naval Architects
and Marine Engineers
74 Trinity Place
New York, New York 10006
Attn: Technical Library

Sun Shipbuilding & Dry Dock Co.
Chester, Pennsylvania 19000
Attn: Chief Naval Architect

Sperry Systems Management Division
Sperry Rand Corporation
Great Neck, N. Y. 11020
Attn: Technical Library

Stanford Research Institute
Menlo Park, California 94025
Attn: Library G-021

Southwest Research Institute
P. O. Drawer 28510
San Antonio, Texas 78284
Attn: Applied Mechanics Review
Dr. H. Abramson

Tracor, Inc.
6500 Tracor Lane
Austin, Texas 78721

Mr. Robert Taggart
3930 Walnut Street
Fairfax, Virginia 22030

Ocean Engr Department
Woods Hole Oceanographic Inst.
Woods Hole, Massachusetts 02543

Worcester Polytechnic Inst.
Alden Research Laboratories
Worcester, Massachusetts 01609
Attn: Technical Library

Applied Physics Laboratory
University of Washington
1013 N. E. 40th Street
Seattle, Washington 98105
Attn: Technical Library

University of Bridgeport
Bridgeport, Conn 06602
Attn: Dr. E. Uram

Cornell University
Graduate School of Aerospace Engr
Ithaca, New York 14850
Attn: Prof. W. R. Sears

University of California
Naval Architecture Department
College of Engineering
Berkeley, California 94720
Attn: Library
Prof. W. Webster
Prof. J. Wehausen
Prof. J. Paulling

California Institute of Technology
Pasadena, California 91109
Attn: Aeronautics Library
Dr. T. Y. Wu
Dr. A. J. Acosta

Docs/Repts/Trans Section
Scripps Institution of
Oceanography Library
University of California, San Diego
P. O. Box 2367
La Jolla, California 92037

Catholic University of America
Washington, D. C. 20017
Attn: Dr. S. Heller, Dept of
Civil & Mech Engr

Colorado State University
Foothills Campus
Fort Collins, Colorado 80521
Attn: Reading Room, Engr Res Center

University of California at San Diego
La Jolla, California 92038
Attn: Dr. A. T. Ellis
Dept. of Applied Math

Florida Atlantic University
Ocean Engineering Department
Boca Raton, Florida 33432
Attn: Technical Library

Harvard University
Pierce Hall
Cambridge, Massachusetts 02138
Attn: Prof. G. Carrier
Gordon McKay Library

University of Hawaii
Department of Ocean Engineering
2565 The Mall
Honolulu, Hawaii 96822
Attn: Dr. C. Bretschneider

University of Illinois
Urbana, Illinois 61801
Attn: Dr. J. Robertson

Institute of Hydraulic Research
The University of Iowa
Iowa City, Iowa 52240
Attn: Library
Dr. L. Landweber
Dr. J. Kennedy

The John Hopkins University
Baltimore, Maryland 21218
Attn: Prof. O. Phillips
Mechanics Dept

Kansas State University
Engineering Experiment Station
Seaton Hall
Manhattan, Kansas 66502
Attn: Prof. D. Nesmith

University of Kansas
Chm Civil Engr Dept Library
Lawrence, Kansas 66044

Fritz Engr Laboratory Library
Dept of Civil Engr
Lehigh University
Bethlehem, Pennsylvania 18015

Dept of Ocean Engineering
Massachusetts Institute of Technology
Cambridge, Massachusetts 02139
Attn: Dept Library
Prof. P. Leehey
Prof. P. Mandel
Prof. M. Abkowitz
Dr. J. Newman

Parsons Laboratory
Massachusetts Institute of Technology
Cambridge, Massachusetts 02139
Attn: Prof. A. Ippen

St. Anthony Falls Hydraulic Laboratory
University of Minnesota
Mississippi River at 3rd Ave S.E.
Minneapolis, Minnesota 55414
Attn: Director
Mr. J. Wetzel
Mr. F. Schiebe
Mr. J. Killen
Dr. C. Song

Department of Naval Architecture
and Marine Engineering
University of Michigan
Ann Arbor, Michigan 48104
Attn: Library
Dr. T. F. Ogilvie
Prof. F. Hammitt

College of Engineering
University of Notre Dame
Notre Dame, Indiana 46556
Attn: Engineering Library
Dr. A. Strandhagen

New York University
Courant Inst of Math Sciences
251 Mercier Street
New York, New York 10012
Attn: Prof. A. Peters
Prof J. Stoker

New York University
University Heights
Bronx, New York 10453
Attn: Prof. W. Pierson, Jr.

Department of Aerospace &
Mechanical Sciences
Princeton University
Princeton, New Jersey 08540
Attn: Prof. G. Mellor

Davidson Laboratory
Stevens Institute of Technology
711 Hudson Street
Hoboken, New Jersey 07030
Attn: Library
Mr. J. Breslin
Mr. S. Tsakonas

Department of Mathematics
St. John's University
Jamaica, New York 11432
Attn: Prof. J. Lurye

Applied Research Laboratory Library
University of Texas
P. O. Box 8029
Austin, Texas 78712

College of Engineering
Utah State University
Logan, Utah 84321
Attn: Dr. R. Jeppson

Stanford University
Stanford, California 94305
Attn: Engineering Library
Dr. R. Street

Webb Institute of Naval Architecture
Crescent Beach Road
Glen Cover, Long Island, N.Y. 11542
Attn: Library
Prof. E. V. Lewis
Prof. L. W. Ward

National Science Foundation
Engineering Division Library
1800 G Street N.W.
Washington, D. C. 20550

University of Connecticut
Box U-37
Storrs, Connecticut 06268
Attn: Dr. V. Scottron
Hydraulic Research Lab

Long Island University
Graduate Department of
Marine Science
40 Merrick Avenue
East Meadow, Long Island, N.Y. 11554
Attn: Prof. David Price

Dr. Douglas E. Humphreys (Code 712)
Naval Coastal Systems Laboratory
Panama City, Florida 32401

Unclassified
Security Classification

DOCUMENT CONTROL DATA - R & D

(Security classification of title, body of abstract and indexing annotation must be entered when the overall report is classified)

1. ORIGINATING ACTIVITY *(Corporate author)*

California Institute of Technology
Pasadena, California 91109

2a. REPORT SECURITY CLASSIFICATION

Unclassified

2b. GROUP

3. REPORT TITLE

Viscous Effects in Inception and Development of Cavitation on Axi-Symmetric Bodies. Part I - Cavitation Inception. Part II - A Semi-Empirical Method to Predict Cavitation Separation on Smooth Bodies.

4. DESCRIPTIVE NOTES *(Type of report and inclusive dates)*

5. AUTHOR(S) *(First name, middle initial, last name)*

Vijay H. Arakeri

6. REPORT DATE	7a. TOTAL NO. OF PAGES	7b. NO. OF REFS
January 1973	166	55

8a. CONTRACT OR GRANT NO.	9a. ORIGINATOR'S REPORT NUMBER(S)
N00014-67-A-0094-0023	
b. PROJECT NO. SR 0230101	Eng. 183-1
c.	9b. OTHER REPORT NO(S) *(Any other numbers that may be assigned this report)*
d.	

10. DISTRIBUTION STATEMENT

Approved for public release; distribution unlimited.

11. SUPPLEMENTARY NOTES	12. SPONSORING MILITARY ACTIVITY
	Naval Ship Research and Development Center (1505) Bethesda, Maryland

13. ABSTRACT

The schlieren method was developed as a flow visualization technique for use in water tunnels. The process of cavitation development on two axi-symmetric bodies was studied using this approach and found to be greatly influenced by the presence of a previously unreported viscous laminar separation. On these bodies, cavitation inception was observed to take place within this separated region which occurs far downstream of the minimum pressure point. On one of these bodies, the incipient cavitation index was found to be closely correlated with the negative value of the pressure coefficient at the point of laminar separation. Approximate computations of the position of transition on a body without laminar separation indicate that the incipient cavitation index is closely correlated with the negative value of the pressure coefficient at the predicted point of transition.

Cavitation separation under fully developed conditions is found to be preceded by a viscous laminar boundary layer separation on bodies which possess the latter separation under fully wetted conditions. An empirical method is proposed to compute the position of cavitation separation on such bodies and the method applied to a sphere and a cylinder showed good agreement with experiments.

14. KEY WORDS	LINK A		LINK B		LINK C	
	ROLE	WT	ROLE	WT	ROLE	WT
Cavitation Viscous Effects Inception Separation Flow Visualization Schlieren Method Axi-Symmetric Bodies